**IDENTIFYING METABOLIC DETERMINANTS OF CELL IDENTITY**

by

Paige Krystin Arnold

A Dissertation

Presented to the Faculty of the

Louis V. Gerstner, Jr. Graduate School of Biomedical Sciences,

Memorial Sloan Kettering Cancer Center

In Partial Fulfillment of the Requirements for the Degree of

Doctor of Philosophy

New York, NY

May 2022

Lydia Finley, PhD

Dissertation Mentor

Date

**To my partner, Blake, and my parents for their unwavering support and encouragement throughout my PhD journey. And to my late dad for instilling curiosity and a love for nature in me.**

## ABSTRACT

Mammalian cells must wire metabolic pathways to support cell-type specific bioenergetic requirements. The tricarboxylic acid (TCA) cycle is a core metabolic pathway that generates reducing equivalents for energy production and several biosynthetic intermediates. TCA cycle-derived products are vital for cell viability and proliferation, yet mammalian cells display considerable diversity in TCA cycle activity. This dissertation focuses on identifying drivers of TCA cycle diversity and investigating whether TCA cycle wiring is crucial for the establishment of cell identity.

Mouse embryonic stem cells (ESCs) are a well-defined primary cell system in which to study distinct cell states and model cell fate transitions. Most proliferating cells in culture rely on glutamine oxidation to fuel the TCA cycle and support cell proliferation, but pluripotent ESCs represent one notable exception. We previously found that ESCs maintained in a state of naïve pluripotency by the addition of pharmacological inhibitors exhibit altered TCA cycle metabolism that enables proliferation in the absence of exogenous glutamine. To build on this work, we used genetic methods to enhance ESC self-renewal and observed that glutamine independence is an inherent feature of highly self-renewing ESCs and not a specific consequence of perturbed signal transduction. Accordingly, only highly self-renewing ESCs within a heterogeneous population could survive and be enriched by transient culture in glutamine-deficient media. These findings established a novel method for eliminating non-pluripotent cells from a mixed population and emphasized the link between TCA cycle wiring and cell identity.

The existence of variable TCA cycle wiring across different cell types led us to hypothesize that TCA cycle enzymes can assemble into multiple pathway configurations. By harnessing genetic co-essentiality mapping to identity putative TCA cycle pathway configurations, we found that TCA cycle genes cluster into two distinct metabolic modules, one of which is the canonical pathway characterized by Sir Hans Krebs. The second module comprises a biochemical alternative to the traditional TCA cycle, in which citrate is exported to

the cytoplasm and metabolized by ATP citrate lyase (ACL), producing oxaloacetate that can be recycled back into the mitochondria to support continuous citrate regeneration. Isotope tracing studies in both cancer cells and ESCs revealed that a significant portion of the TCA cycle transits through the cytoplasm in an ACL-dependent manner and that ACL loss forces cells to engage in primarily traditional TCA cycle metabolism. Thus, this 'non-canonical' TCA cycle represents a significant alternative to the traditional TCA cycle in both normal and transformed cells.

Krebs originally elucidated the traditional TCA cycle in pigeon breast muscle. We therefore asked whether TCA cycle configuration is cell-state dependent by culturing C2C12 mouse myoblasts, which can be differentiated *in vitro* into mature myotubes. In accordance with Krebs' work, we found that myogenic differentiation is accompanied by a switch from ACL-dependent to primarily traditional TCA cycle metabolism. Next, we used ESCs to study TCA cycle dynamics during changes in cell fate. These studies revealed that exit from naïve pluripotency drives a shift towards non-canonical TCA cycle metabolism. Consequently, loss of ACL prevents metabolic adaptation upon induction of differentiation and blocks ESCs from exiting the pluripotent state. These results demonstrate that TCA cycle behavior is linked to cell state and reveal that successful cell state transitions require appropriate TCA cycle engagement.

Non-canonical TCA cycle engagement offers several advantages to proliferating cells, including retention of reduced carbon that would otherwise be lost as $CO_2$ and regeneration of cytosolic NAD+, a limiting cofactor for biosynthetic reactions. Thus, non-canonical TCA cycle engagement adds to the diversity of metabolic strategies that allow cells to meet their unique bioenergetic demands. Collectively, the work in this dissertation uncovers a context-dependent alternative to the traditional TCA cycle active across a wide array of mammalian cells.

## BIOGRAPHICAL SKETCH

Paige Krystin Arnold was born on September 9th, 1992, to Amy Marie and Ray T. Arnold in Hollywood, FL. Paige spent most of her childhood in Coral Springs, FL. In 2010, she moved to North Carolina to attend Duke University, where she worked in the laboratory of Dr. Kristin Scott investigating mechanisms of heterochromatin maintenance and inheritance in fission yeast. During the summer of 2013, Paige participated in the Summer Undergraduate Research Program of the Louis V. Gerstner, Jr. Graduate School of Biomedical Sciences at Memorial Sloan Kettering Cancer Center (MSKCC). During the program, she worked in the laboratory of Dr. Maria Jasin studying the role of BRCA2 function in human mammary epithelial cell viability. This formative experience solidified Paige's interest in research and motivated her to pursue a PhD. In 2014, she graduated *magna cum laude* with a Bachelor of Science in Biology, a minor in Philosophy, and a certificate in Genome Sciences & Policy. Paige went on to enroll in the Cancer Biology PhD program at the Louis V. Gerstner, Jr. Graduate School of Biomedical Sciences at MSKCC in 2015. Following a year in Dr. Mary Goll's laboratory studying the role of DNA methylation at pericentromeric heterochromatin, she joined Dr. Lydia Finley's laboratory in 2017. With Dr. Finley's guidance, Paige has used a variety of research approaches to identify links between metabolic wiring and cell identity.

## ACKNOWLEDGMENTS

Pursuing a PhD is hard. A few people told me this when I started back in 2015, but no one could have prepared me for the experience. And certainly no one could have anticipated the other major events of my PhD: a lab and topic switch at the end of my second year, near-constant political upheaval, and a global pandemic. I relied heavily on my mentors, colleagues, and loved ones to see me through, and I'm immensely thankful for their encouragement and guidance.

First and foremost, I would like to express my gratitude to my mentor, Dr. Lydia Finley. I'm beyond grateful that she took a chance on me and let me join her newly founded research group when I was without a lab at the end of my second year. It wasn't easy for me to develop a new thesis project while taking on a totally new field, but Lydia's belief in me enabled me to try more and achieve more during my PhD than I ever thought possible. I have grown so much as a scientist over the last five years under her continuous support and guidance and I greatly appreciate the time and effort that she invested in my training. Her enthusiasm for science is an inspiration and joy for those of us in her lab and her insistence on celebrating even small victories always made it easier to overcome challenges and setbacks. It has been an honor to engage in the scientific process with her and learn from her curiosity and rigorous approach to science. I've learned most of what I know from our weekly one-on-one meetings—I will miss these conversations but intend to carry what I've learned from her with me for the rest of my career.

I would also like to thank my committee members, Drs. Maria Jasin and Danwei Huangfu, for their advice and support throughout my PhD. Even when I pivoted to an

entirely different field, it was important to me that these two phenomenal scientists remain on my committee. Their scientific insights during my committee meetings greatly strengthened my thesis work and their sage advice helped me at multiple points during my PhD. Dr. Jasin has been a mentor to me since I spent a summer in her laboratory as an undergraduate and I have benefited greatly from her guidance. I've also been fortunate enough to collaborate with Dr. Huangfu and her lab and it was an honor to witness her thoughtful approach to science in this context. I'm also grateful to Dr. Andrew Intlekofer for agreeing to chair my dissertation committee and for providing valuable feedback throughout my PhD via our joint lab meetings. I would like to thank Dr. Kathryn Wellen for agreeing to be my external examiner and for the opportunity to present my work to her research group a few years ago. Beyond my dissertation committee, I'd like to thank Dr. Santosh Vardhana, with whom I collaborated and learned so much from.

I am deeply indebted to current and formers members of the Finley lab—thank you for your kindness and for making it a joy to come to lab every day. It's been a pleasure to know and work with each of you and I feel so lucky to be a part of this amazing group. To Jossie Yashinskie, Dr. Pavlina Todorova, and Yanyang Chen—it was an extremely fun and formative experience to be founding members of the lab with you all. These members, along with Dr. Julia Brunner, Ben Jackson, Katrina Paras, and Abby Xie—have been so helpful with experimental assistance and I'm inspired every day by their intelligence, thoughtfulness, and scientific prowess. To Ben—from rotation student to incredibly talented collaborator, you have been a wonderful science partner and I'm constantly impressed by your creative approach to science. To Jossie—thank you for being a support system for me throughout my time in lab, it's been fun to constantly

laugh with you and grow as a scientist alongside you. I'm also immensely grateful to our administrative assistant, Sonia Das, who has continually supported us lab members and kept our lab afloat, particularly during the most challenging parts of the pandemic.

Next, I would like to thank the administration of the Gerstner Sloan Kettering (GSK) Graduate School. Your commitment to graduate students was palpable even during my time in the Summer Undergraduate Research Program back in 2013 and is a major reason why I selected the program for my PhD. Deans Dr. Ken Marians and Dr. Michael Overholtzer, Associate Dean Linda Burnley, and Assistant Dean Dr. Thomas Magaldi—thank you for your support and vision for a unique, supportive training environment. Thank you to David McDonagh, Stacy De La Cruz, Julie Masen, and Raphaelle Chassagne for your continuous support and assistance in helping students navigate the program. I would also like to thank past members of the administration, including Maria Torres, Ivan Gerena, Alexandria Woodside, and Iwona Abramek for their help and encouragement in the early years of my PhD. Last but certainly not least, I would like to thank my GSK classmates, past and present, for being such a wonderful group. Some of my favorite memories from my PhD are from GSK social events—it's been a pleasure to train with such a fun and talented cohort.

This journey would not have been possible without my support system outside of the lab. To all my friends, thank you for enriching my life and being there for me over the last several years. I've disrupted and canceled a lot of plans because of lab, thanks for being understanding about this ☺. To Matt, Shikha, and Kyle—you are quite literally family and have celebrated the highs of this journey with me and lifted me up during the lows, I don't know what I would do without you. To Alexa—thank you for the last

almost two decades of friendship, your advice means the world to me. To Maria—thank you for being such a wonderful friend and one of my biggest cheerleaders since we first met freshman year. To Emily, Rui, and Gemma—from classmates to lifelong friends, thank you for being such a huge part of my graduate school experience.

I am forever grateful for the love and support of my family. To my Mom—there really aren't words for the endless encouragement and guidance that you've given me and the sacrifices that you've made for me. Everything I know about strength and resilience I learned from you, I'm so lucky to be your daughter. To my stepdad, Edward—thank you for your constant kindness and love, you are such a source of stability in my life. To my dad— I wish you could have been here to share in this journey with me as you are perhaps the reason why I became a scientist in the first place. Thank you for teaching me to constantly be curious and for making nature such a huge part of my upbringing. To the rest of my family, thank you for providing support from near and far.

Finally, I'm eternally grateful to my partner, Blake, for the huge role that he has played during my PhD—thank you for your unconditional love and support. You've been there for me since the very beginning of this journey, celebrating my successes, encouraging me during stressful moments, and holding me up when things were hard. You went above and beyond to make things easier for me whenever you could, and that meant the world to me. You and Lenny have brought me so much joy and I can't wait for the next phase of our incredible life together!

## TABLE OF CONTENTS

## LIST OF FIGURES

## LIST OF TABLES

## LIST OF ABBREVIATIONS

| | |
|---|---|
| **2HG** | 2-hydroxyglutarate |
| **ACL** | ATP-citrate lyase |
| **ACO** | aconitase |
| **ACO2** | aconitase 2 |
| **ACSS2** | acyl-coenzyme A synthetase short-chain family member 2 |
| **αKG** | alpha-ketoglutarate |
| **AML** | acute myelogenous leukemia |
| **AP** | alkaline phosphatase |
| **ATP** | adenosine triphosphate |
| **BCAAs** | branched-chain amino acids |
| **BCAT1** | branched-chain amino acid transaminase 1 |
| **$Ca^{2+}$** | calcium |
| **$CO_2$** | carbon dioxide |
| **CoA-SH** | coenzyme A |
| **CPT1** | carnitine acetyltransferase I |
| **CPT2** | carnitine acetyltransferase II |
| **CS** | citrate synthase |
| **d5-2HG** | d-2-hydroxyglutaric-2,3,3,4,4-$d_5$ acid |
| **DAPI** | 4,6-diamidino-2-phenylindole |
| **ESCs** | embryonic stem cells |
| **ETC** | electron transport chain |
| **FACS** | fluorescence-activated cell sorting |
| **FH** | fumarate hydratase |
| **GCMS** | gas chromatography-mass spectrometry |
| **GCSF** | granulocyte colony-stimulating factor |
| **GDH** | glutamate dehydrogenase |
| **Gln** | glutamine |
| **GLS** | glutaminase |
| **GLUT1** | glucose transpoter 1 |
| **GO** | gene ontology |
| **GOT1** | glutamic-oxaloacetic transaminase 1 |
| **GOT2** | glutamic-oxaloacetic transaminase 2 |
| **GSH** | glutathione |
| **GTP** | guanosine triphosphate |
| **$H_2O_2$** | hydrogen peroxide |
| **H3K27me3** | H3 trimethylated lysine 27 |
| **hESC** | human embryonic stem cells |

| | |
|---|---|
| **HFSCs** | hair follicle stem cells |
| **HIFs** | hypoxia-inducible transcription factors |
| **IDH1** | isocitrate dehydrogenase 1 |
| **IDH2** | isocitrate dehydrogenase 2 |
| **IDH3** | isocitrate dehydrogenase 3 |
| **IF** | immunofluorescence |
| **ISCs** | intestinal stem cells |
| **JHDM** | Jumonji C-domain-containing histone demethylases |
| **LCMS** | liquid chromatography-mass spectrometry |
| **LDH** | lactate dehydrogenase |
| **LDHA** | lactate dehydrogenase-A |
| **LIF** | leukemia inhibitory factor |
| **M2-rtTA** | reverse tetracycline-dependent transactivator |
| **MCT1** | monocarboxylate transporters |
| **MCU** | mitochondrial calcium uniporter |
| **MDH1** | malate dehydrogenase 1 |
| **MDH2** | malate dehydrogenase 2 |
| **MEFs** | mouse embryonic fibroblasts |
| **MPC** | mitochondrial pyruvate carrier |
| **MS** | mass spectrometry |
| **mtDNA** | mitochondrial DNA |
| **NMR** | nuclear magnetic resonance |
| **NSCLC** | non-small cell lung cancer |
| **$O_2^-$** | superoxide |
| **OAA** | oxaloacetate |
| **OCR** | oxygen consumption rate |
| **OGDH** | oxoglutarate dehydrogenase |
| **OP-puro** | O-propargyl-puromycin |
| **OXPHOS** | oxidative phosphorylation |
| **PC** | pyruvate carboxylase |
| **PDHC** | pyruvate dehydrogenase complex |
| **PDKs** | pyruvate dehydrogenase kinases |
| **PDPs** | pyruvate dehydeogenase phosphatases |
| **PHDs** | prolyl hydroxylases |
| **PI** | propidium iodide |
| **PI3K** | phosphatidylinositol 3-kinase |
| **PPARs** | peroxisome proliferator-activated receptors |
| **Q** | glutamine |
| **ROS** | reactive oxygen species |
| **rTCA cycle** | reductive TCA cycle |

| | |
|---|---|
| **RTKs** | receptor tyrosine kinases |
| **S/L** | serum/LIF |
| **SDH** | succinate dehydrogenase |
| **SLC25A1** | mitochondrial citrate/malate antiporter |
| **SODs** | super dismutases |
| **TCA** | tricarboxylic acid |
| **TET** | ten-eleven translocation |
| **tetOP** | tetracycline-dependent minimal promoter |

# CHAPTER 1: INTRODUCTION

## 1.1 TCA cycle overview

Cellular metabolism comprises a complex network of biochemical reactions that support cell survival and proliferation in living organisms. All cells need to generate the energy and reducing equivalents necessary to support basic biological processes and maintain homeostasis[1]. Accordingly, cells have evolved the capacity to acquire nutrients and direct them towards catabolic pathways that break down molecules to harness chemical energy. Proliferating cells have additional bioenergetic demands beyond homeostasis as they must also accumulate the intracellular biomass necessary for cell duplication[1]. To meet this requirement, cells have also evolved anabolic pathways that convert nutrients into biosynthetic building blocks, like proteins, lipids, and nucleic acids. Proliferative metabolism requires the appropriate engagement of both anabolic and catabolic pathways to support the bioenergetic requirements of rapid cell growth.

At the nexus of both catabolic and anabolic metabolism lies the tricarboxylic acid (TCA) cycle, a core metabolic pathway in eukaryotic cells consisting of a cyclic series of chemical reactions that harness high-energy electrons from fuel sources[2-4]. The reactions of the TCA cycle involve the consecutive oxidation of carbon substrates to carbon dioxide ($CO_2$), thereby generating reducing equivalents that can donate electrons to the electron transport chain (ETC) to produce cellular energy in the form of adenosine triphosphate (ATP) via a process known as oxidative phosphorylation (OXPHOS) (**Figure 1.1**)[4]. While the TCA cycle is generally considered a catabolic process, it also

produces several intermediates that serve as critical precursors for biosynthetic reactions[5,6]. Because the TCA cycle functions in both catabolic and anabolic capacities, it is considered an amphibolic pathway[7,8].

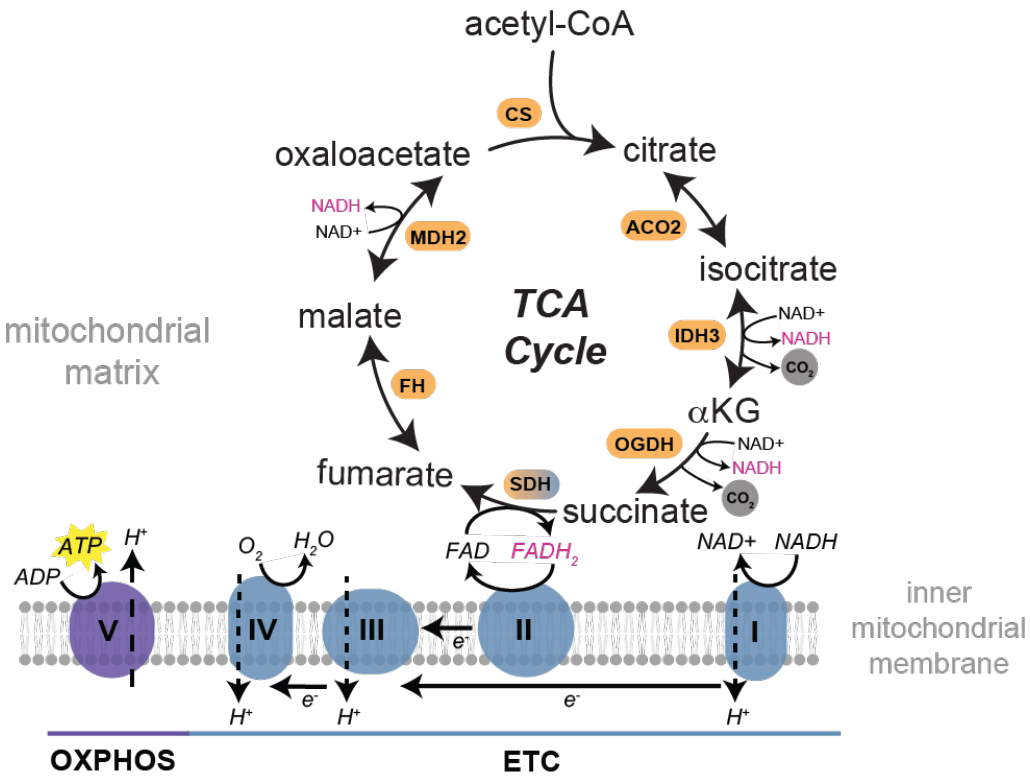


**Figure 1.1 Overview of the tricarboxylic acid (TCA) cycle.**
The TCA cycle starts when the two-carbon molecule acetyl-CoA combines with four-carbon oxaloacetate to form citrate, a reaction catalyzed by citrate synthase (CS). Citrate is then converted to isocitrate by aconitase 2 (ACO2). Isocitrate is decarboxylated to αKG in an NAD+-dependent manner by isocitrate dehydrogenase 3 (IDH3) or in an NADP+-dependent manner by isocitrate dehydrogenase 2 (IDH2), releasing carbon dioxide ($CO_2$). αKG undergoes decarboxylation to succinyl-CoA via oxoglutarate dehydrogenase (OGDH), producing NADH and releasing $CO_2$. Succinyl-CoA is then converted to succinate by succinyl-CoA synthetase. This is the only substrate-level phosphorylation step in the TCA cycle as it is coupled to the generation of guanosine triphosphate (GTP), which can be converted to adenosine triphosphate (ATP). Succinate is converted to fumarate by succinate dehydrogenase (SDH), a multi-subunit enzyme that participates in both the TCA cycle and the electron transport chain (ETC). SDH reduces FAD to $FADH_2$, which donates its electrons to complex II. Fumarate is converted to malate by fumarate hydratase (FH). Malate dehydrogenase 2 (MDH2) converts malate to oxaloacetate in an NAD+-dependent manner, regenerating the starting molecule and supporting the next turn of the cycle. Note: most TCA cycle reactions are reversible. Legend continued on the next page.

**Figure 1.1 Overview of the tricarboxylic acid (TCA) cycle. (*continued*)**
Electrons that are released during TCA cycle oxidation are transferred to NAD+ and FAD to form 3 NADH and 1 $FADH_2$ molecules. These reducing equivalents are reoxidized upon donating their electrons to the ETC, supporting continued TCA cycle activity. As the electrons donated by these reducing equivalents are transferred through the ETC and eventually to oxygen, complexes I, III, and IV pump protons across the inner mitochondrial membrane. This proton pumping establishes a proton gradient that is used by Complex V, or ATP synthase, to generate ATP from ADP, a process known as oxidative phosphorylation (OXPHOS). TCA cycle enzymes are colored in orange, ETC components are colored in blue or purple. SDH is colored blue and orange because it participates in both the TCA cycle and the ETC. Reducing equivalents are shown in pink.

## 1.2 Evolutionary perspectives on the TCA cycle

Cellular life emerged approximately 4 billion years ago, at a time in the Earth's history when its atmosphere is predicted to have been largely reducing and devoid of oxygen[9]. The existence of life in any capacity on Earth requires the generation of basic cellular constituents. Ancient pathways thus must have acted to produce starting organic molecules for the synthesis of biomolecules, like proteins, lipids, and nucleic acids. A major theory in the study of primordial metabolism is that these ancient anabolic pathways originated spontaneously based on geochemical conditions before the emergence of enzymes, genetic material, or cells[10]. It has been shown that the reactions of the oxidative TCA cycle can occur non-enzymatically in the presence of iron as a catalyst and oxidizing agents other than oxygen[11,12]. However, given what we know about geochemical conditions at the time that life emerged, primordial metabolism likely centered on reductive, $CO_2$-fixing pathways[10]. Clues about primordial metabolism have been sought by studying the metabolism of $CO_2$-fixing chemoautotrophs, which lie at the root of the tree of life and thus may offer insights into the earliest biosynthetic pathways[10].

A $CO_2$-fixing pathway of particular interest found in eubacteria and archaea and both aerobes and anaerobes is the reductive TCA cycle (rTCA cycle), or reverse Krebs cycle[13]. The rTCA cycle consists of a cyclic series of chemical reactions that are essentially those of the TCA cycle but in reverse[14]. Accordingly, while the oxidative TCA cycle oxidizes acetyl-CoA to $CO_2$ to generate electron donors (reducing equivalents) and ATP, the rTCA cycle captures $CO_2$ to generate acetyl-CoA in a process requiring electron donors and ATP (**Figure 1.2**). The rTCA cycle is an appealing candidate for early, prebiotic metabolism because it produces acetyl-CoA, pyruvate, oxaloacetate (OAA), succinate, and alpha-ketoglutarate (αKG), the five universal metabolic precursors for biosynthetic molecules (e.g. lipids, glucose, nucleic acids, amino acids, and co-factors)[10,11,15]. Intriguingly, a large portion of the cycle has been shown to occur non-enzymatically by minerals using photochemistry or metal ions under harsh, acidic conditions, not unlike those proposed on early Earth[10,11,16].

The ability of the rTCA cycle and other carbon-assimilating pathways to produce organic molecules eventually allowed for the synthesis of metabolic enzymes and the genetic material that mediated their propagation. Many of the enzymes of the oxidative, forward TCA cycle are reversible and, thus, function similarly to the enzymes that comprise the rTCA cycle. One of the biggest differences between the two cycles is that the rTCA cycle requires the conversion of succinate to αKG. This reaction, mediated by an αKG synthase, is highly unfavorable and requires a strong reducing agent in the form of reduced ferredoxin[14,15]. In the forward TCA cycle, citrate synthase (CS) is the key enzyme that condenses acetyl-CoA with OAA to form citrate. The rTCA cycle, on the other hand, requires that citrate be cleaved to liberate acetyl-CoA and regenerate OAA,

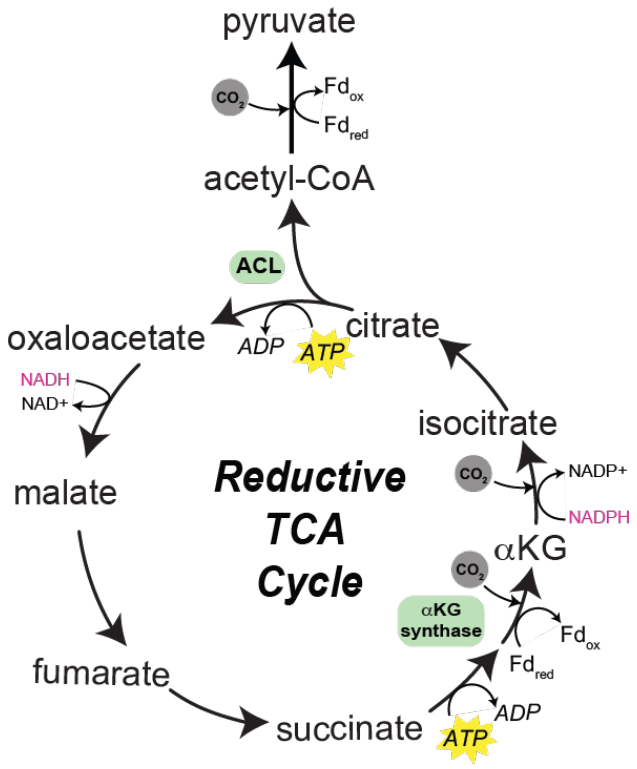


**Figure 1.2 The reductive TCA cycle.**
A simplified schematic depicting the reductive TCA cycle, or reverse Krebs cycle. Most reactions of this cycle are the same as those of the oxidative TCA cycle but in reverse and are catalyzed by the same enzymes. The major exceptions include cleavage of citrate to form oxaloacetate and acetyl-CoA and the production of alpha-ketoglutarate (αKG) from succinate. Citrate cleavage requires ATP and is carried out by ATP-citrate lyase (ACL) or the related citryl-CoA lyase and citryl-CoA synthase enzymes. Conversion of succinate to αKG, mediated by αKG synthase, is highly energetically unfavorable and thus requires a strong reducing agent in the form of reduced ferredoxin ($Fd_{red}$). The conversion of acetyl-CoA to pyruvate is catalyzed by pyruvate synthase and also utilizes $Fd_{red}$. While the oxidative TCA cycle combusts carbon and produces energy (ATP) and reducing equivalents, the reductive TCA cycle utilizes ATP and reducing equivalents to assimilate carbon and produce acetyl-CoA. Reducing equivalents are shown in pink.

a reaction that is catalyzed by the ATP-citrate lyase (ACL) enzyme. Recent work has demonstrated that CS bears structural similarity to and likely originated from an ancestral citryl-CoA lyase module related to ACL that operates in the reverse Krebs cycle of the deep branching bacterial phylum Aquificae[17]. Moreover, the CS reaction, which was previously considered irreversible, can proceed in the reverse direction in certain

anaerobes and this reversibility is favored under high $CO_2$ conditions[18-20]. These findings strengthen the notion that the rTCA cycle may represent both a vestige of prebiotic metabolism and an evolutionary precursor for the oxidative TCA cycle[15,21].

Over time, the oxygenation of the Earth's atmosphere likely facilitated the emergence of the oxidative TCA cycle as well as the coupling of the TCA cycle with OXPHOS. The evolution of increasingly complex TCA cycle enzymes was also a critical development as it allowed for both the improved efficiency of this metabolic pathway and the enhanced capacity for regulation of its activity[11]. Being able to fine-tune the function of metabolic pathways like the TCA cycle set the stage for early unicellular life forms to evolve into multicellular organisms, as this process required coordination of metabolic activity beyond that dictated by local nutrient availability[22].

### 1.3 Wiring of the mammalian TCA cycle

With each 'turn' of the TCA cycle, the TCA cycle intermediate OAA condenses with acetyl-CoA to generate citrate, which is oxidized in subsequent reactions to produce two molecules of $CO_2$, one GTP or ATP molecule, and four reducing equivalents (3 NADH and 1 $FADH_2$) (**Figure 1.1**)[4]. These reducing equivalents deposit their electrons onto the ETC, thereby driving the generation of ATP via OXPHOS. Importantly, each turn of the cycle ends with the regeneration of the starting molecule, OAA. OAA acts as a catalyst in the TCA cycle—only a small amount is required for the oxidation of large amounts of acetyl-CoA.

### *1.3.1 Discovery of the TCA cycle*

The catalytic role of OAA within the TCA cycle was essential to the cycle's discovery and elucidation. In 1935, Albert Szent-Györgyi worked out the sequence of reactions from succinate to fumarate to malate to OAA and demonstrated the rapid oxidation of these substances by pigeon breast muscle[23,24]. From this work, Szent-Györgyi hypothesized that dicarboxylic acids function in a catalytic capacity to promote oxygen uptake[23]. Support for this idea came the following year when Stare and Baumann found that very small quantities of dicarboxylic acids were sufficient to cause an increase in oxygen consumption and that this increase was beyond what was necessary for the oxidation of the quantities of substrate added[25]. Significantly, they also found that added dicarboxylic acids were not used up and could still be detected in the medium[25]. In 1937, Hans Krebs showed that succinate could be synthesized by animal tissues in the presence of pyruvate, leading him to speculate that succinate may arise from citrate oxidation[3,23]. A key finding in that same year came from Martius and Knoop, who found that αKG is a product of citrate oxidation and worked out the sequence of reactions from citrate to succinate[26].

These crucial experiments teed up the findings of Hans Krebs and his colleague William Johnson in *Enzymologia* in 1937, in which they discovered that citrate was readily oxidized by minced pigeon breast muscle and that citrate addition increased oxygen uptake beyond the amount necessary for the complete oxidation of the added citrate[2]. Moreover, they found that citrate did not disappear during this process, indicating that it was being continuously reformed[2,23]. Their work also showed that large

quantities of citrate could be synthesized anaerobically by muscle in the presence of OAA and that OAA, when added to muscle, condensed with two carbon atoms from an unknown precursor to form citrate[2]. By adding malonate, an inhibitor of succinate oxidation, they found that succinate accumulated when OAA was added to muscle, implying that this series of reactions was cyclical in nature[2,23]. In subsequent work, Krebs determined that the two carbon atoms that condensed with OAA to form citrate were derived from pyruvate[27]. Later work by Lipmann and others elucidated that the two-carbon molecule required for citrate synthesis was, in fact, acetyl coenzyme A, or acetyl-CoA[28,29].

In theory, OAA regeneration allows for infinite turning of the TCA cycle, assuming a continuous supply of acetyl-CoA. Following multiple turns of the TCA cycle, TCA cycle intermediate carbons can be entirely derived from and replaced by acetyl-CoA carbons[5]. However, TCA cycle intermediates can be siphoned from the cycle to feed into other metabolic pathways or supply precursors for macromolecule biosynthesis, a process termed 'cataplerosis'[30]. For example, mitochondrial citrate can be exported to the cytoplasm and metabolized by ACL to liberate acetyl-CoA, which is required for de novo lipid synthesis and protein acetylation[31,32]. The metabolite αKG functions as a critical intermediate in the synthesis of several amino acids, including alanine and aspartate, and can be diverted from the cycle for this purpose[1]. OAA itself is the source of the amino acid aspartate, a critical output of the TCA cycle that is utilized in the urea cycle and for protein and nucleotide biosynthesis[33,34]. Cataplerosis of OAA-derived aspartate requires the replacement of OAA to sustain TCA cycle activity. The process of replacing these and other intermediates that are removed from the TCA cycle is termed 'anaplerosis'[30].

Robust, sustained TCA cycle function requires both a continuous source of acetyl-CoA and replenishment of TCA cycle intermediates (particularly OAA) via anaplerotic reactions (**Figure 1.3**).

### *1.3.2 Sources of acetyl-CoA*

*Glucose oxidation*

Pyruvate derived from glucose oxidation functions as the primary source of acetyl-CoA for the TCA cycle in most mammalian cells[35]. Glucose is metabolized via glycolysis to form two molecules of pyruvate, which undergo oxidative decarboxylation to form acetyl-CoA in the mitochondrial matrix following import by the mitochondrial pyruvate carrier (MPC). This irreversible reaction is catalyzed by the pyruvate dehydrogenase complex, or PDHC, a supramolecular assembly of multiple catalytic subunits[36]. The PDHC is allosterically inhibited by NADH, acetyl-CoA, and ATP, making it a sensor of TCA cycle activity and thus a critical node of TCA cycle regulation (discussed further below)[37]. By converting the glycolytic product pyruvate into a substrate for TCA cycle oxidation, the PDHC functions as a gatekeeping enzyme that links glycolysis to the TCA cycle and mitochondrial respiration.

Glycolysis-derived pyruvate has an alternative fate outside of the mitochondria. Lactate dehydrogenase (LDH) can reduce pyruvate to lactate in the cytosol and this reaction is coupled with NADH oxidation to NAD+. In the absence of oxygen, this process of fermenting pyruvate to form lactate, also known as anaerobic glycolysis, occurs in mammals as a means of sustaining biosynthetic processes under hypoxia[36].

However, in 1924, Otto Warburg found that cancer cells produce significant amounts of lactate even in the presence of oxygen[38,39]. Subsequent investigation has revealed that

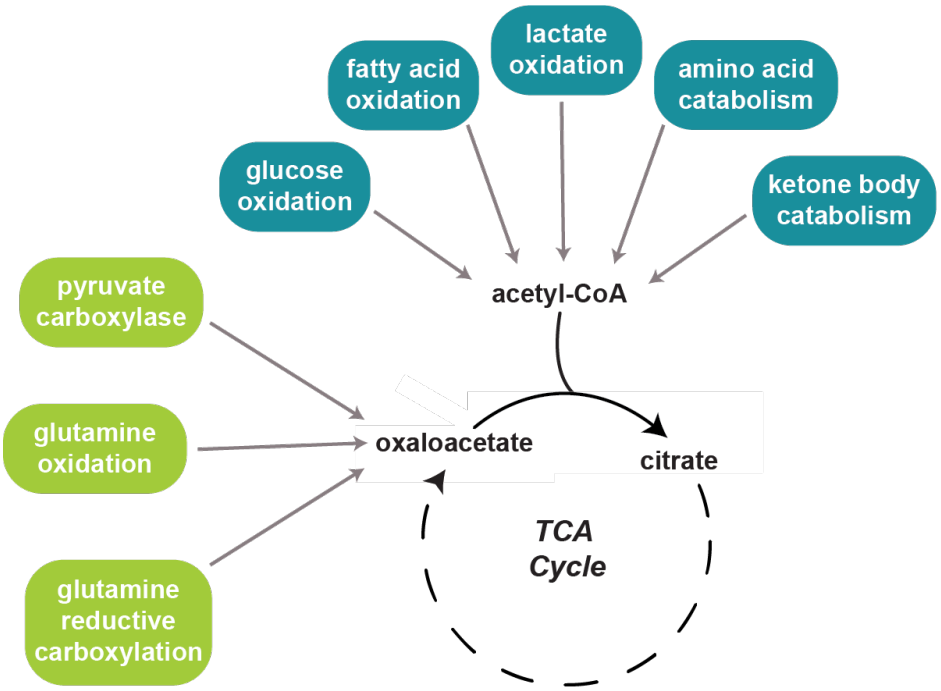


**Figure 1.3 Inputs into the TCA cycle.**
A functioning TCA cycle requires a continuous pool of acetyl-CoA and production of oxaloacetate. Several pathways either produce acetyl-CoA directly or produce pyruvate, an indirect source of acetyl-CoA through the activity of the pyruvate dehydrogenase complex. Sources of acetyl-CoA are shown in teal. Removal of TCA cycle intermediates ('cataplerosis') occurs at multiple steps of the cycle to supply precursors for biosynthetic processes or feed into other metabolic pathways. Replacement of these intermediates ('anaplerosis') is required to support continuous production of oxaloacetate. Sources of anaplerosis are shown in green.

proliferating cells significantly engage in this process, termed aerobic glycolysis or the Warburg effect. While the field continues to debate the underlying benefits of engaging in aerobic glycolysis, one clear advantage to the process is that it allows cells to robustly regenerate NAD+ in the cytosol. Cytosolic NAD+ is used during the conversion of glyceraldehyde-3-phosphate to 1,3-bisphosphoglycerate and, thus, is required to sustain

continuous flux through glycolysis[1]. Glycolysis provides carbon that supports nucleotide and lipid biosynthesis and some glycolytic intermediates are precursors for amino acid biosynthesis[1]. Therefore, glycolysis provides several biosynthetic advantages to proliferating cells beyond producing pyruvate. Proliferating cells must balance their use of pyruvate towards oxidation in the TCA cycle with their glycolytic flux and concomitant cytosolic NAD+ requirements.

*Fatty acid oxidation*

If glucose levels are low or pyruvate oxidation is otherwise unable to supply sufficient levels of acetyl-CoA to support TCA cycle function, cells can use fatty acids to generate acetyl-CoA using fatty acid oxidation, or β-oxidation. β-oxidation requires that fatty acids be transported from the cytosol into the mitochondrial matrix via the carnitine shuttle[36]. Before shuttling into the mitochondrion, long-chain fatty acids are first converted to their fatty acyl-CoA ester by fatty acyl-CoA synthetase[40]. Because the mitochondrial membrane is impermeable to fatty acyl-CoAs, transport first requires the activity of carnitine acetyltransferase I (CPT1), which is located on the outer mitochondrial membrane and converts fatty acyl-CoA to fatty acyl-carnitine[40]. The carnitine-translocase protein, located on the inner mitochondrial membrane, then exchanges this fatty acyl-carnitine for a free carnitine molecule. Once inside the mitochondrial matrix, carnitine acetyltransferase II (CPT2) reconverts acyl-carnitine back to its acyl-CoA ester, releasing carnitine that can continue to support translocase activity[36]. Mitochondrial fatty acyl-CoA then undergoes β-oxidation, which produces both an acetyl-CoA molecule and reducing equivalents following sequential degradation

in a four-enzyme reaction process[40]. Depending on the length of the original long-chain fatty acid, the β-oxidation process can be repeated several times, shortening acyl-CoAs to liberate two carboxy-terminal carbons as acetyl-CoA with each iteration[40].

Cells must sense intracellular levels of fatty acids and integrate this information with their requirement for de novo lipid synthesis versus β-oxidation. Sensing of free fatty acid availability primarily occurs through peroxisome proliferator-activated receptors (PPARs), which function as fatty acid-activated transcription factors that drive the expression of the rate-limiting enzyme of fatty acid oxidation, CPT1[41,42]. CPT1 itself is allosterically inhibited by the fatty acid synthesis intermediate malonyl-CoA, a regulatory step that prevents simultaneous fatty acid synthesis and oxidation[36,40].

*Lactate oxidation*

While glucose-derived pyruvate is the primary source of acetyl-CoA carbons for TCA cycle oxidation in cultured cells in vitro, recent work has revealed that glucose may not be the preferred fuel source of cells in vivo[43-45]. Within rapidly growing cells, the LDH-mediated conversion of pyruvate to lactate is a major source of cytosolic NAD+ that supports sustained glycolytic flux. Proliferating cells in culture typically excrete this lactate as a waste product to support redox and pH homeostasis[44]. However, recent studies in vivo have demonstrated that cells import lactate from the circulation via monocarboxylate transporters (e.g. MCT1) and directly oxidize it, resulting in a large fraction of pyruvate and TCA cycle intermediates being derived from circulating lactate[44,45]. In most tissues and in tumors, the contribution of circulating lactate to TCA cycle intermediates exceeds that of glucose, supporting the idea that lactate is a

fundamental TCA cycle substrate in living organisms[44,45]. Future work should be aimed at understanding the compartmentalization of lactate oxidation. One study found that LDH can localize to the mitochondria, which suggests that lactate can undergo direct mitochondrial uptake and catabolism[46]. Of note, mitochondrial import and catabolism of lactate would prevent the buildup of cytosolic NADH that can antagonize glycolytic flux and allow for the mitochondrial capture of both carbon and reducing equivalents[46].

*Amino acid and ketone body catabolism*

Acetyl-CoA can also be derived from the breakdown of amino acids and ketone bodies. Removal of the amino group from ketogenic amino acids, including lysine and the branched-chain amino acids (BCAAs) leucine and isoleucine, results in a carbon skeleton that can be catabolized to acetyl-CoA directly or the ketone body acetoacetate[47,48]. Acetoacetate can be converted to acetyl-CoA by first undergoing conversion to acetoacetyl-CoA by β-ketoacyl-CoA transferase followed by cleavage by thiolase[36]. In differentiated adipocytes, catabolism of BCAAs accounts for almost a third of cellular acetyl-CoA pools[49]. Catabolism of glucogenic amino acids, including serine and cysteine, and the transamination of alanine by alanine aminotransferase produce pyruvate, which can be converted to acetyl-CoA by PDHC. Beyond amino acids, the ketone body β-hydroxybutyrate can also be converted to acetoacetate, providing another potential source of acetyl-CoA.

### *1.3.3 TCA cycle anaplerosis*

*Pyruvate carboxylase*

Because OAA-derived aspartate is diverted from the TCA cycle for other metabolic pathways, including protein and nucleotide biosynthesis, anaplerosis is required to replenish OAA pools and maintain TCA cycle function. Pyruvate, derived from glucose, lactate, and amino acid sources, functions as a major anaplerotic source of OAA through the activity of the mitochondrial enzyme pyruvate carboxylase (PC)[30]. PC catalyzes the ATP-dependent carboxylation of pyruvate to generate OAA[50]. PC activity is allosterically activated by abundant acetyl-CoA, making it a potent sensor of OAA demand in the mitochondria[51]. This enzyme is also allosterically inhibited by both αKG and glutamate, thereby suppressing simultaneous engagement of both PC- and glutamine-mediated anaplerosis (see below)[52]. PC-derived OAA can either contribute to the TCA cycle or serve as a substrate for phosphoenolpyruvate carboxykinase (PEPCK), which catalyzes the decarboxylation of OAA to phosphoenolpyruvic acid in the gluconeogenic pathway[30]. PC is expressed in most tissues and is particularly active in gluconeogenic tissues like the kidney and liver. PC-mediated anaplerosis is also important in succinate dehydrogenase (SDH)-mutant cells, which exhibit a truncated TCA cycle and thus require an alternative source of OAA to support TCA cycle function and sustain aspartate production for anabolic pathways[53,54].

*Glutamine anaplerosis*

The preferred anaplerotic substrate in most proliferating cells growing in culture is glutamine, the most abundant amino acid in mammals[22,55-57]. Across cultured cell lines, the majority of the carbons in aspartate and other TCA cycle intermediates are supplied

by glutamine[56,58]. While glutamine can be synthesized directly by cells, it has been recognized for several decades that glutamine supplementation is necessary for the growth and viability of many cultured cell lines, particularly cancer cell lines[57,59,60]. Glutamine taken up by cells through transporters such as ASCT2 and LAT1 is converted to glutamate by glutaminase (GLS), producing ammonia, or through nitrogen-donating reactions involved in purine and pyrimidine nucleotide synthesis[61]. Glutamate can then be converted to αKG, which can enter the TCA cycle and undergo oxidation. Production of αKG from glutamate occurs through two mechanisms: 1) by deamination via glutamate dehydrogenase (GDH), releasing ammonia and the reducing equivalent NAD(P)H, or 2) by transaminases that transfer the amino group from glutamate to a keto-acid, generating αKG and an amino acid[62]. Notably, transamination is freely reversible, meaning aspartate aminotransferases (glutamic-oxaloacetic transaminase 1, GOT1; glutamic-oxaloacetic transaminase 2, GOT2) can alternatively directly generate OAA using αKG and aspartate. Cells can become particularly reliant on glutamine oxidation via GDH when their ability to oxidize glucose is impaired, e.g. upon MPC inhibition[63]. However, under normal, glucose-replete conditions, transamination is the dominant reaction that drives glutamine anaplerosis[63-65]. This is perhaps because transamination bypasses the production of ammonia, a toxic byproduct that must be dealt with by cells, or because transamination by GOT1/GOT2 provides the dual benefit of glutaminolysis and generation of aspartate from OAA.

In normal cells, glutamine serves as a major anaplerotic source of OAA through the oxidative decarboxylation of glutamine-derived αKG in the TCA cycle. However, under conditions of hypoxia or impaired mitochondrial respiration, reductive

carboxylation becomes the favored route of glutamine anaplerosis[53,66,67]. During reductive carboxylation, glutamine-derived αKG is converted to isocitrate and then to citrate through reverse isocitrate dehydrogenase (IDH) and aconitase (ACO) flux, respectively[66,67]. ACL-mediated metabolism of the citrate generated by reductive carboxylation is critical to supply acetyl-CoA carbons for de novo lipid synthesis during TCA cycle disruption. ACL cleavage of citrate derived from reductive carboxylation also provides an alternative anaplerotic source of OAA, allowing cells to bypass a truncated or otherwise defective TCA cycle.

The extent to which cells engage in either PC flux or glutaminolysis for anaplerosis has been shown to depend on multiple factors, including glucose versus glutamine availability, cellular capacity to deal with ammonia toxicity, and competition for glutamine, which also serves as a nitrogen source in biosynthetic pathways[62,68]. Anaplerotic substrate preference is likely also governed by cellular redox demands given that GDH-mediated production of αKG also produces NAD(P)H, which can be used for oxidative stress management and other biological processes (see below)[56,62].

### 1.4 Nodes of TCA cycle control

Because the TCA cycle functions as a critical biosynthetic hub and is coupled with cellular energy production via OXPHOS, cells have evolved multiple nodes of TCA cycle regulation. In this section, we will outline three different mechanisms by which tight control is exerted over the pathway.

### *1.4.1 Allosteric regulation of TCA cycle enzyme activity*

Metabolic flux through the TCA cycle is tightly coordinated by both negative and positive allosteric regulation of TCA cycle-associated enzymes. Three enzymes in particular—CS, IDH, and oxoglutarate dehydrogenase (OGDH)—are considered regulatory enzymes within the pathway. All three enzymes undergo allosteric inhibition by high levels of NADH[36,69]. In the electron transport chain, complex I and complex II function to replenish NAD+ and FAD, respectively, to support continuous TCA cycle activity[70]. Thus, inhibition of TCA cycle enzymes by high NADH levels functions to shutdown TCA cycle activity upon ETC dysfunction. OXPHOS activity also signals to the TCA cycle at the level of ATP; high ATP:ADP ratios allosterically inhibit IDH, resulting in a deceleration of the cycle upon excess energy supply[71]. OGDH undergoes substrate inhibition by succinyl-CoA, an intermediate product in the conversion of αKG to succinate. Succinyl-CoA also serves as an allosteric inhibitor of CS[70,72]. Apart from the three regulatory enzymes, SDH undergoes allosteric inhibition by OAA, slowing the cycle down upon insufficient acetyl-CoA availability[73].

### *1.4.2 Pyruvate dehydrogenase complex regulation*

While not technically part of the TCA cycle, the PDHC generates the starting molecule of the cycle, acetyl-CoA, thereby functioning as a gatekeeper of TCA cycle activity. During PDHC catalysis, a carboxyl group is removed from pyruvate and released as $CO_2$, and the remaining two-carbon molecule is oxidized, with NAD+

accepting the electrons to form NADH. The PDHC is a multienzyme complex composed of multiple copies of three catalytic subunits: pyruvate dehydrogenase (E1), dihydrolipoamide acetyltransferase (E2), and dihydrolipoamide dehydrogenase (E3). These subunits carry out the sequential conversion of pyruvate into acetyl-CoA along with five different coenzymes, including coenzyme A (CoA-SH), the universal carrier for acyl groups. The complex is activated by its substrate, pyruvate, and inhibited by its product, acetyl-CoA. Like IDH, the PDHC is also allosterically inhibited by a high ATP:ADP ratio, allowing it to respond to cellular energy status. Importantly, like the three regulatory enzymes of the TCA cycle described above, the PDHC is negatively regulated by high NADH levels. Inhibition of the complex by NADH links PDHC flux and, thus, acetyl-CoA production to ETC function and mitochondrial redox status (**Figure 1.4**). Recent work has shown that enhancing pyruvate oxidation via the PDHC can impair cell proliferation by limiting mitochondrial NAD+ availability, which increases mitochondrial membrane potential to the extent that NAD+ regeneration by complex I of the ETC becomes impaired[74]. Increasing cellular ATP consumption upon PDHC activation rescues proliferation, indicating that cell proliferation can be impaired when the demand for mitochondrial NAD+ exceeds that of ATP[74]. This may explain why highly proliferative cells often engage in aerobic glycolysis over pyruvate oxidation and OXPHOS, even in the presence of sufficient oxygen[74].

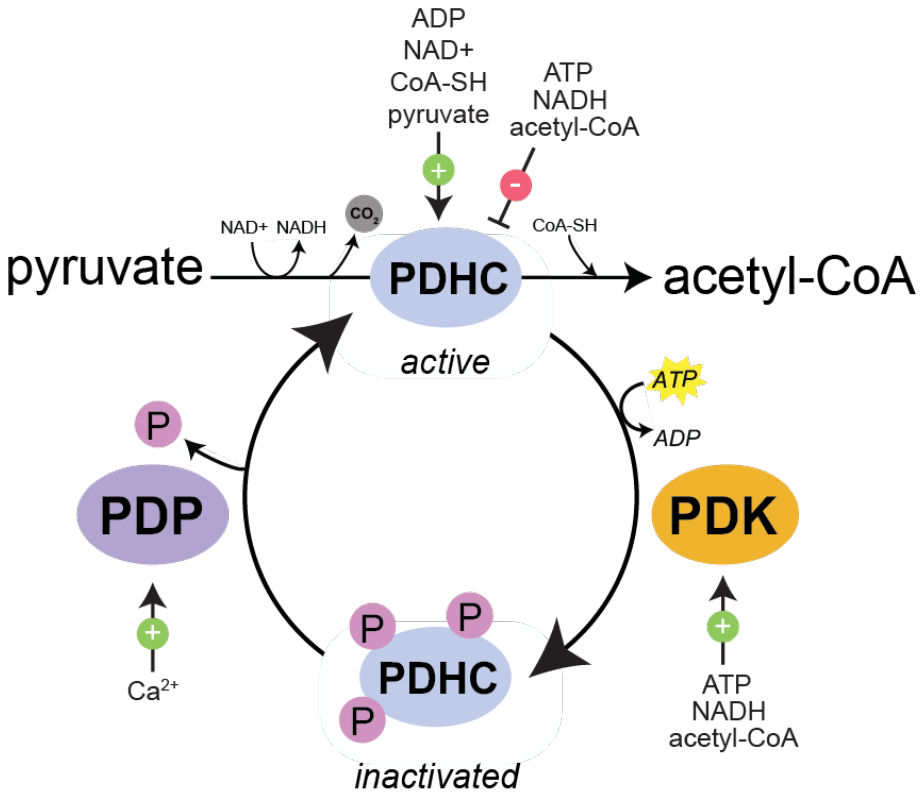


**Figure 1.4 Allosteric and covalent regulation of the pyruvate dehydrogenase complex.** The pyruvate dehydrogenase complex (PDHC) catalyzes the irreversible decarboxylation of pyruvate to acetyl-CoA, releasing $CO_2$ and transferring electrons to NAD+ to form NADH. The PDHC utilizes multiple coenzymes, including coenzyme A (CoA-SH), during its multistep reaction. The complex is activated by increased levels of ADP, NAD+, CoA-SH, and its substrate pyruvate. Conversely, the PDHC is allosterically inhibited by high levels of ATP, NADH, and its product acetyl-CoA. Phosphorylation of three serine residues on the PDHC by pyruvate dehydrogenase kinases (PDKs) inactivates the complex. The PDKs are activated by high levels of ATP, NADH, and acetyl-CoA, reinforcing the shutdown of PDHC flux under these conditions. The inhibitory phosphorylation of the PDHC is reversible and can be removed by the pyruvate dehydrogenase phosphatases (PDPs), which are activated by mitochondrial calcium ($Ca^{2+}$).

Beyond allosteric regulation, the PDHC is also regulated by covalent modification. The activity of the mammalian complex is regulated by the phosphorylation status of three serine residues (Ser-264, Ser-271, and Ser-203) on the pyruvate dehydrogenase E1 alpha subunit[75]. Four pyruvate dehydrogenase kinases (PDKs; PDK1-4) catalyze phosphorylation of the serine residues, each with different site specificities[75].

Phosphorylation of the complex is inhibitory but reversible via removal by pyruvate dehydrogenase phosphatases (PDPs; PDP1-2). While the PDHC is activated by NAD+, ADP, and pyruvate, the PDKs are conversely activated by NADH, ATP, and high acetyl-CoA levels[76]. The PDKs and PDPs provide cells with the ability to fine-tune PDHC activity through multiple signaling inputs. For example, low oxygen levels activate the hypoxia-inducible transcription factors (HIFs), which bind to hypoxia-response elements within a large number of target genes. The HIF-1 transcription factor activates lactate dehydrogenase-A (LDHA) and PDK1, leading to suppression of PDHC activity with a concomitant increase in aerobic glycolysis[36]. To preferentially engage aerobic glycolysis, cancer cells frequently co-opt several pathways, including the HIF/hypoxia transcriptional program, to enhance PDK1 expression and achieve PDHC repression[77].

### *1.4.3 Calcium-mediated TCA cycle regulation*

Calcium ($Ca^{2+}$) functions as an intracellular messenger in an array of biological processes, including mitochondrial metabolism. Mitochondrial $Ca^{2+}$ uptake primarily occurs via the mitochondrial calcium uniporter (MCU), a highly selective ion channel in the inner mitochondrial membrane. MCU-mediated $Ca^{2+}$ influx is driven by the membrane potential established by ETC activity[78]. Once inside the mitochondria, $Ca^{2+}$ ions directly activate isocitrate and OGDH enzymes. $Ca^{2+}$ binding to IDH leads to a decrease of the Km for isocitrate and this effect is enhanced by a decrease in the ATP:ADP ratio[79]. The binding of $Ca^{2+}$ to OGDH decreases the Km for αKG. Intramitochondrial $Ca^{2+}$ indirectly activates the PDHC by activating PDP1, leading to

dephosphorylation and activation of the complex[79,80]. Thus, intramitochondrial $Ca^{2+}$ regulates both carbon entry into and flux through the TCA cycle. Maintenance of $Ca^{2+}$ homeostasis is critical for cell viability as mitochondrial $Ca^{2+}$ overload favors opening of the permeability transition pore, leading to collapse of mitochondrial membrane potential and activation of cell death[78].

### *1.4.4 Regulation of TCA cycle substrate choice*

Multiple substrates feed into the TCA cycle, including glucose, fatty acids, and amino acids. TCA substrate preference is regulated by an array of factors, including culture conditions for cells *in vitro*[81] and circulating metabolite levels and environmental milieu for cells *in vivo*[82-84]. Transcriptional rewiring, such as the activation of the hypoxia/HIF transcriptional program, in both physiological and cancer contexts has also been shown to alter a cell's preferred TCA cycle fuel[83]. It remains understudied whether the various nodes of TCA cycle control outlined here also contribute to cellular nutrient preference and mode of utilization.

## 1.5 TCA cycle subversion in cancer

Cells must duplicate their biomass prior to division. Accordingly, proliferation requires that cells rewire their metabolism to support biomass accumulation. Cancer is defined by aberrant and uncontrollable cell proliferation, and it has been appreciated for well over a century that this rapid cell growth is driven by significant reprogramming of

metabolic activity. As a central metabolic hub, the TCA cycle is frequently a major target of metabolic rewiring in tumors. This section will cover some examples of how both inputs and outputs of the TCA cycle are exploited in cancer.

### *1.5.1 Deregulated nutrient uptake*

*Glucose uptake*

Cancer cells increase their acquisition of nutrients from the environment to support the anabolic demands of rapid cell growth. Perhaps the earliest metabolic feature to be associated with tumors is their avid uptake and consumption of glucose, which was first appreciated nearly 100 years ago by Otto Warburg[38,85]. This phenomenon has been confirmed in a variety of tumor contexts since that time and is the basis for clinical use of positron emission tomography-based imaging of the uptake of a radioactive, fluorine-labeled glucose analog, $^{18}$F-fluorodeoxyglucose, to detect cancer relative to normal tissue[86]. Following uptake, glucose is catabolized via glycolysis, which produces several biosynthetic precursors including the ribose-5-phosphate required for nucleic acid synthesis. Pyruvate produced from glycolysis can be oxidized in the TCA cycle or converted to lactate under the process of aerobic glycolysis. The tendency of cancer cells to significantly engage in aerobic glycolysis (see above) is an interesting paradox given that it results in the disposal of glucose-derived carbons and, by bypassing the TCA cycle, prevents cells from extracting much of the energy stored in glucose. Warburg himself theorized that upregulation of aerobic glycolysis in cancer cells could be due to defective respiration and/or mitochondrial function and that this could represent a

defining feature and driver of cancer[87]. However, this view has been refuted by multiple lines of evidence. Non-transformed cell types like T-cells also increase glucose uptake and shift towards enhanced aerobic glycolysis when stimulated with pro-proliferative stimuli[88]. Moreover, most cancer cells continue to oxidize carbon in the TCA cycle[89,90] and require intact respiration for growth[91-93], indicating that the TCA cycle is indeed intact and active in cancer.

Glucose and amino acids are polar molecules and thus require membrane transport proteins to cross the plasma membrane. In normal cells, the expression of sugar and amino acid transporters is regulated in a non-cell-autonomous manner via growth-factor-mediated activation of receptor tyrosine kinases (RTKs)[36]. Binding of extracellular growth factors activates RTKs to engage signaling pathways, namely those involving Ras and phosphatidylinositol 3-kinase (PI3K). Engagement of these pathways leads to activation of key downstream effectors, such as AKT, mTOR, and MEK/ERK, that promote nutrient uptake and stimulate anabolic activity. The PI3K/AKT signaling axis promotes the expression of glucose transporter 1 (GLUT1) and mediates its translocation to the cell surface where it facilitates glucose import[94]. Activation of this axis also enhances the activity of the glycolytic enzyme hexokinase, which catalyzes the first step of glycolysis by phosphorylating imported glucose molecules to prevent their efflux back into extracellular space[95]. Tumor cells frequently acquire gain-of-function mutations in PI3K or loss-of-function mutations in PTEN, the negative regulator of PI3K, mitigating the requirement for growth factor-mediated activation of the PI3K/AKT signaling axis and promoting constitutive glucose uptake and metabolism[6,96].

*Glutamine uptake*

Glutamine is another fundamental nutrient and source of TCA cycle carbon in proliferating cells. Beyond contributing to TCA cycle anaplerosis and participating directly in protein synthesis, glutamine contributes to other anabolic pathways by providing an amide group to support nucleotide synthesis and an α-amino group to support the synthesis of non-essential amino acids[6]. Most cultured cancer cell lines and some tumors are addicted to glutamine and display increased glutaminolysis, or the use of and reliance on glutamine as a bioenergetic substrate, and these phenotypes are largely driven by enhanced activity of the transcription factor Myc[97-100]. Myc positively regulates glutaminolysis by driving the expression of glutamine transporters like ASCT2 and the enzyme GLS, which converts glutamine to glutamate and is thus necessary for the TCA cycle's usage of glutamine. The Myc transcriptional program also bolsters glucose metabolism by enhancing the expression of glucose transporters and most glycolytic enzymes[101,102] and reinforces aerobic glycolysis by stimulating the expression of PDK1 to repress the PDHC and LDHA to promote the conversion of pyruvate to lactate[77,103]. Because of its role in coordinating glutaminolysis and other anabolic pathways, Myc functions as a proto-oncogene in cancer and is frequently aberrantly activated by gene amplification, chromosomal translocations, and other genomic events[104].

*Macromolecule uptake*

In addition to reinforcing direct uptake of low-molecular-weight nutrients like glucose and amino acids, cancer cells also take advantage of more opportunistic modes of nutrient acquisition[6]. This capability is critical for cancer cells in vivo as the progressive

growth of tumors is often accompanied by increasingly insufficient nutritional support from the blood vasculature. Under conditions of nutrient depletion or when their ability to take up nutrients directly from the environment is compromised, cancer cells can ingest and degrade bulk extracellular protein in an indiscriminate manner through the process of macropinocytosis, providing an intracellular source of free amino acids[6,105]. Oncogenic Ras mutations endow cancer cells with increased ability to engage in macropinocytosis, enhancing the ability of these cells to survive under amino acid-deplete conditions[106,107]. Cancer cells can also scavenge other extracellular macromolecules, including lipids, via macropinocytosis or a more selective, receptor-mediated process known as endocytosis[108]. Under conditions of extreme metabolic stress, cells can capture and degrade intracellular proteins or entire intracellular structures/organelles to support their nutritional needs and maintain cell survival[109]. However, by definition, autophagy cannot provide cancer cells with the ability to net accumulate new biomass for cell proliferation[6].

### *1.5.2 Reactive oxygen species*

The TCA cycle generates reducing equivalents that deposit their electrons onto the ETC to drive aerobic respiration via OXPHOS. OXPHOS is a highly efficient means of generating energy in the form of ATP. However, a significant consequence of electron transfer through the ETC is the generation of reactive oxygen species (ROS), which are volatile molecules that can be toxic to DNA, proteins, and lipids. A very small percentage of the electrons stored in TCA cycle-derived reducing equivalents (NADH and $FADH_2$) leak from the system and react with molecular oxygen to produce superoxide ($O_2^-$)[36].

ETC complexes I, II, and III generate $O_2^-$ and release it into the mitochondrial matrix, where superoxide dismutases (SODs) rapidly convert it to hydrogen peroxide ($H_2O_2$). $H_2O_2$ accumulation in the mitochondria can damage mitochondrial proteins and DNA (mtDNA) while $H_2O_2$ leakage into the cytosol can damage cellular proteins and nuclear DNA[110]. Multiple enzymes, including glutathione (GSH) peroxidases and peroxiredoxins, detoxify $H_2O_2$ to $H_2O$ in the mitochondrial matrix and cytosol. Controlling levels of $H_2O_2$ is important to maintain cellular integrity; in the presence of ferrous or cuprous ions, $H_2O_2$ can become a highly reactive hydroxyl radical, which causes potentially lethal oxidative damage to cellular constituents[111].

While ROS have historically been viewed as harmful metabolic by-products of aerobic respiration and other cellular processes, work over the past few decades has uncovered a physiological role for ROS in regulating cellular signaling and behavior. Low levels of $H_2O_2$ can reversibly oxidize cysteine residues in redox-sensitive target proteins, thereby functioning as a post-translational modification that can modulate protein function and the activity of downstream signaling pathways[111]. The dephosphorylation activity of certain redox-sensitive phosphatases, including PTEN, can be inhibited by being reversibly oxidized by $H_2O_2$, thereby affecting signal transduction[112-114]. Proteomics-based approaches have identified the reversible oxidation of thousands of proteins that participate in diverse biological functions, including proliferation, immune regulation, and adaptation to metabolic stress[36,115,116].

Cancer cells have been shown to carry higher levels of ROS than their normal counterparts[115,117]. Many cancer-associated changes can promote mitochondrial ROS production, including loss of tumor suppressor activity and alterations in mitochondrial

metabolism[91]. For example, increased hypoxia or engagement of the HIF/hypoxia transcriptional program slows the flow of electrons through the ETC and increases the likelihood of ROS generation. Enhanced levels of ROS can be beneficial to cancer cells as ROS can inhibit some redox-sensitive phosphatases, thereby maintaining signaling pathways in an activated state. 'Sweet spot' levels of ROS can generate just enough DNA damage and genomic instability to promote the acquisition of oncogenic alterations that reinforce tumorigenesis[115,118]. However, excessive levels of ROS can cause lethal oxidative damage to DNA and other cellular components and either directly activate cell death or sensitize cells to other forms of oxidative stress. Therefore, cancer cells must balance the production of ROS with a high rate of antioxidant activity[36]. Multiple antioxidant defense systems require the cofactor NADPH as an electron donor. The TCA cycle enzymes isocitrate dehydrogenase 2 (IDH2) in the mitochondria and isocitrate dehydrogenase 1 (IDH1) in the cytosol produce NADPH from the conversion of isocitrate to αKG [115]. By modulating flux through the TCA cycle, cancer cells can coordinate both ROS production and the maintenance of antioxidant defenses to strike the most advantageous redox balance.

### *1.5.3 Metabolic control of gene expression and cell fate*

Changes in cell fate ultimately occur through the acquisition of cell-type-specific gene expression programs that are enabled by cooperation between transcription factor availability and accessibility of the chromatin landscape. TCA cycle metabolites are increasingly appreciated for their role in modulating the chromatin landscape via their

regulation of the activity of αKG-dependent dioxygenases. The family of αKG-dependent dioxygenases includes Jumonji C-domain-containing histone demethylases (JHDM) and ten-eleven translocation (TET) DNA methylcytosine oxidases, which remove repressive histone marks and 5-methylcytosine, respectively, and alter the accessibility of chromatin. These enzymes utilize αKG, ferrous iron, and oxygen as co-substrates[22], thereby integrating multiple metabolic pathways in the control of gene expression programs and, ultimately, cell fate decisions.

*Exploitation of alpha-ketoglutarate production*

Alterations in intracellular αKG levels have been shown to modulate cell fate in cancer and stem cells. Depriving *APC*-mutant intestinal organoids of glutamine depletes intracellular αKG levels and promotes stemness and adenocarcinoma formation in vivo[119]. αKG supplementation rescues these effects by driving DNA and histone demethylation, which facilitates upregulation of differentiation-associated genes and blunts tumor growth in vivo[119]. The branched-chain amino acid transaminase 1 (BCAT1) enzyme, which mediates catabolism of valine, leucine, and isoleucine, normally restricts αKG pools in acute myelogenous leukemia (AML), leading to a hypermethylated chromatin landscape that blunts normal myeloid differentiation[120]. BCAT1 loss leads to accumulation of αKG and induces myeloid differentiation[120]. The effect of αKG on cell fate is likely context-specific, however, as interventions that increase αKG levels in mouse embryonic stem cells (ESCs) favor self-renewal over differentiation[121,122]. Moreover, naïve, highly self-renewing ESCs possess larger pools of αKG than their more committed counterparts (see below)[121].

*Oncometabolite Accumulation*

Beyond being regulated by fluctuations in intracellular αKG levels, αKG-dependent dioxygenases can be competitively inhibited by metabolites with structural similarity to αKG, including 2-hydroxyglutarate (2HG), fumarate, and succinate. By blocking the enzymatic activity of histone and DNA demethylases, these 'oncometabolites' can function to lock cells in a hypermethylated state that blocks differentiation and reinforces a malignant, stem cell-like phenotype[22,123-125]. 2HG can exist as either a D- or L-enantiomer (D-2HG or L-2HG) and is present at low concentrations in normal cells. However, D-2HG levels accumulate in cancer cells that harbor mutations in IDH1 and IDH2 that confer neomorphic enzymatic activity that favors the reduction of αKG to D-2HG[126,127]. These mutations have been identified in a range of tumor types, including solid tumors (e.g. gliomas and chondrosarcomas) and blood cancers like AML[111,128,129]. L-2HG can be produced in the absence of mutant IDH1/2 via the promiscuous enzymatic activity of malate dehydrogenase 1 or 2 (MDH1/MDH2) or LDHA[111]. This promiscuous enzymatic activity is amplified during hypoxia[130,131] and under acidic pH[132,133], raising the possibility that 2HG accumulation may play a regulatory role under normal physiological conditions.

Like 2HG accumulation, increased levels of the TCA cycle metabolites succinate and fumarate can inhibit JHDM and TET enzymes, driving a widespread hypermethylation phenotype that disrupts normal cell differentiation[134,135]. Mutations in the TCA cycle enzymes involved in the breakdown of these metabolites—SDH and fumarate hydratase (FH)—have been shown to facilitate the pathogenesis of certain rare

cancers (e.g. paragangliomas) and inherited cancer-predisposition syndromes[136-138]. In addition to affecting the activity of chromatin-associated αKG-dependent dioxygenases, succinate and fumarate accumulation can also inhibit αKG-dependent prolyl hydroxylases (PHDs), leading to stabilization of HIF-1 and concomitant activation of the HIF/hypoxia transcriptional program[139,140]. As a result of this 'pseudohypoxic' state, SDH- and FH-mutant tumors exhibit enhanced glycolytic metabolism and production of high ROS levels[141].

*Acetyl-CoA and Histone Acetylation*

The TCA cycle provides another critical input to chromatin regulation in the form of acetyl-CoA. As discussed above, several substrates feed into the TCA cycle at the level of acetyl-CoA, which condenses with oxaloacetate to form citrate. Acetyl-CoA itself cannot diffuse across the mitochondrial membrane; however, citrate can be transported out of the mitochondria to the cytoplasm, where it can undergo cleavage by ACL. ACL-mediated citrate cleavage provides a major source of acetyl-CoA that can be used for both de novo lipid synthesis and protein acetylation reactions. Acetylation of histone tails alters chromatin dynamics and generally increases accessibility to transcription factors, leading to activation of gene transcription[22]. Thus, regulation of cytosolic acetyl-CoA generation can modulate transcriptional outputs by altering global histone acetylation[142]. The PI3K/AKT signaling pathway mediates both the generation and cytosolic export of glucose-derived citrate while AKT-mediated phosphorylation of ACL enhances its catalytic activity[22,143]. Accordingly, oncogenic activation of the

PI3K/AKT signaling axis increases acetyl-CoA levels and promotes elevated histone acetylation both in vitro and in tumors[144].

Tumorigenesis requires that cells implement oncogenic gene expression programs, and metabolic reprogramming that promotes epigenetic remodeling can facilitate this process. By co-opting the production and localization of TCA cycle metabolites, cancer cells can regulate the activity of chromatin-modifying enzymes and exert control over gene expression and cell fate.

### 1.6 TCA cycle heterogeneity

The TCA cycle generates multiple outputs that are critical for cell viability and proliferation, including the reducing equivalents required for energy production and several biosynthetic precursors. Yet, despite the central role of TCA cycle-derived products in viability and growth, mammalian cells exhibit considerable diversity in TCA cycle activity. This includes heterogeneity in metabolic enzyme activity, differences in preferred TCA cycle substrate, and variability between cells in whether they synthesize certain TCA cycle-derived precursors de novo or take them up from the extracellular environment[83,145]. These observations have largely been derived from studies that use isotope tracing to track metabolic pathway activity. In isotope tracing studies, metabolites are extracted from experimental systems that have been exposed to isotopically labeled versions of nutrients that contain a heavy labeled atom (such as $^{13}C$ or $^{15}N$) in one or more positions. Techniques like nuclear magnetic resonance (NMR) or mass spectrometry (MS) are then used to track the passage of these heavy labeled atoms

through metabolic systems[36]. Uniformly labeled glucose and glutamine, e.g. $^{13}$C-glucose and $^{13}$C-glutamine, are particularly relevant for the study of flux through the TCA cycle (**Figure 1.5**). By tracing the fate of isotopically labeled carbons throughout TCA cycle intermediates, we can determine the relative contribution of these nutrients to different metabolites and measure the fractional abundance of different isotopologues, or the same metabolites that vary in their isotopic composition[146]. This wealth of information enables the characterization of TCA cycle behavior in different cell types and unique cellular contexts.

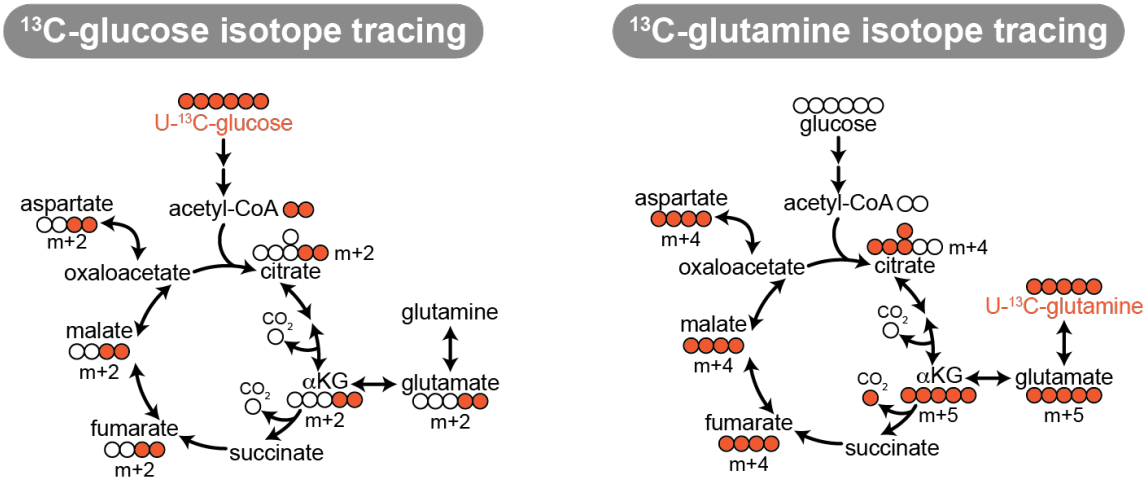


**Figure 1.5 Quantifying TCA cycle flux using isotope tracing.**
Schematics depicting how oxidative metabolism of uniformly labelled glucose ([U-$^{13}$C]glucose) (left) and glutamine ([U-$^{13}$C]glutamine) (right) generates metabolites associated with the TCA cycle. The colored circles represent $^{13}$C-labeled carbons. Figure is adapted from Vardhana, Arnold et al., *Nature Metabolism* 2019.

### *1.6.1 TCA cycle heterogeneity in cancer*

Most mammalian cells growing in culture rely on both glucose- and glutamine-derived carbon to fuel the TCA cycle. However, isotope tracing studies in both lung and

glioblastoma tumors suggest that glutamine is a relatively minor source of TCA cycle carbon in cancer cells growing in vivo[90,147]. The extent to which cancer cells growing in vivo rely on glucose versus glutamine as TCA cycle substrates is likely informed, in part, by cancer type and driver genetic mutations. Liver tumors with aberrant Myc activity display enhanced glutamine oxidation and sensitivity to therapies that target glutamine catabolism[100]. Clear cell renal carcinomas do not oxidize glucose-derived carbon in the TCA cycle and instead preferentially engage in aerobic glycolysis[148]. Recent in vivo tracing studies have also revealed that TCA cycle metabolism in vivo is fueled by substrates beyond glucose and glutamine. As described above, the contribution of circulating lactate to TCA cycle intermediates exceeds that of glucose in most tissues and in tumors.[44,45] Some cancer types, including liver and glioblastomas, readily take up acetate, which can be converted to acetyl-CoA by the mitochondrial enzyme acyl-coenzyme A synthetase short-chain family member 2 (ACSS2) and undergo oxidation in the TCA cycle[149,150].

### *1.6.2 TCA cycle heterogeneity in adult tissue stem cells*

Isotope tracing and metabolomics-based approaches have also revealed heterogeneity in TCA cycle activity across cell states. Adult tissue stem cells regulate organ homeostasis by balancing the choice between self-renewal and differentiation into mature cell types. In multiple tissue contexts, adult tissue stem cells have been found to primarily engage in aerobic glycolysis. Upon lineage commitment and differentiation, however, cells increase their oxidation of pyruvate in the TCA cycle and display

enhanced OXPHOS[151-153]. For example, intestinal stem cells (ISCs) express lower levels of MPC than their differentiated progeny and blocking mitochondrial pyruvate entry via MPC inhibition drives increased ISC numbers and proliferative potential[154]. Unlike ISCs, hair follicle stem cells (HFSCs) are not continuously proliferative and instead remain dormant unless induced to divide during a new hair cycle[155]. LDHA expression and activity are high in HFSCs relative to other cell types in the epidermis and promoting lactate production via MPC deletion boosts their activation[156]. Conversely, deleting LDHA prevents HFSC activation and the initiation of a new hair cycle[156]. Myogenic differentiation is also coupled with increased pyruvate oxidation and OXPHOS and this metabolic shift is likely driven, in part, by the significant energy demands of skeletal muscle[152,157]. Collectively, these studies illustrate that TCA cycle substrate preference and behavior can vary within the same lineage.

### *1.6.3 TCA cycle heterogeneity in pluripotent stem cells*

Pluripotent stem cells are emerging as a powerful system in which to study metabolism during cell state transitions. While pluripotency, or the ability to give rise to all embryonic germ layers, is a state that exists only transiently during early mammalian development, it can be modeled indefinitely in vitro[158]. Mouse embryonic stem cells (ESCs) derived from the inner cell mass of preimplantation stage embryos can generate all somatic and germline lineages in vitro and in chimeric embryos[158]. Mouse ESCs are typically maintained in serum supplemented with leukemia inhibitory factor (LIF), which activates JAK/STAT3 signaling to reinforce the pluripotent state[158]. However, cells

maintained under these conventional serum/LIF ("S/L") culture conditions display heterogeneous expression of pluripotency-associated transcription factors such as Nanog[159]. This heterogeneity is linked to the propensity of individual cells to either self-renew or spontaneously differentiate. In contrast, culturing mouse ESCs in the presence of two small molecule inhibitors, PD0325901 (a MEK inhibitor) and CHIR99021 (a GSK3β inhibitor), referred to as "2i", generates ESCs that homogenously express high levels of pluripotency-associated transcription factors[160,161]. These ESCs are considered naïve as they reflect the ground state of pluripotency observed in pre-implantation epiblasts *in vivo* and have been shown to be more resistant to spontaneous differentiation than their S/L-cultured counterparts.

Despite being derived from the same source, naïve and more committed S/L ESCs possess distinct metabolic phenotypes. Naïve ESCs accumulate pools of αKG, which may reinforce the pluripotent state by stimulating αKG-dependent dioxygenases to drive more open chromatin[121,162]. Moreover, while most cultured cell lines require glutamine supplementation to support cell survival and proliferation, naïve ESCs can grow in the absence of exogenous glutamine. The glutamine-independent phenotype exhibited by naïve ESCs is coupled with a reduction in the contribution of glutamine-derived carbons to TCA cycle intermediates[121]. Metabolic activity also varies with PSC identity in human ESCs, which display increased mitochondrial respiration upon conversion to a more naïve state[163].

These findings indicate that cell state transitions are accompanied by rewiring of TCA cycle activity in pluripotent stem cells. Moreover, pluripotent cell state transitions are dictated by controlled media formulations, making ESCs a highly tractable system in

which to study metabolism and uncover links between TCA cycle wiring and cell identity.

### 1.7 Dissertation research aims

While there are certain hallmarks of proliferative metabolism, it has become increasingly evident that mammalian cells can solve the problem of survival and growth using markedly diverse metabolic strategies. The TCA cycle is a core metabolic pathway that generates reducing equivalents that fuel energy production and metabolites that support proliferation, yet mammalian cells display considerable heterogeneity in TCA cycle activity. Diversity in TCA cycle function suggests that the pathway can be wired to meet cell-type specific demands, yet the link between TCA cycle wiring and cell identity remains largely unexplored. In this dissertation, we aim to determine whether TCA cycle behavior is an intrinsic component of cell identity (**Chapter 2**) and identify drivers of TCA cycle heterogeneity (**Chapter 3**). These aims will shed light on the different metabolic strategies that cells can exploit to support growth and proliferation during normal development and in aberrant disease states like cancer.

# CHAPTER 2: GLUTAMINE INDEPENDENCE IS AN INTRINSIC FEATURE OF PLURIPOTENT STEM CELLS

## 2.1 Introduction

When induced to proliferate in culture, mammalian cells rewire metabolic pathways to support the anabolic demands of cell growth. Cells take up high levels of glucose and glutamine, which are used to generate the metabolic building blocks, reducing equivalents and energy required to duplicate biomass prior to cell division[57]. Consequently, exogenous supplies of both glucose and glutamine are essential to sustain rapid proliferation of most cultured cell lines[57]. While proliferating cells of all lineages share many common metabolic features, most notably elevated glycolysis and glutaminolysis, recent evidence demonstrates that there is not one single mode of proliferative metabolism. Rather, cells can engage multiple routes of nutrient acquisition and catabolism to support survival and proliferation[164]. Several factors contribute to this metabolic diversity, including cell lineage, genetic makeup and environmental conditions[165]. This raises the intriguing possibility that metabolic manipulation can provide selective pressures that promote or antagonize the proliferation of distinct cell types in a predictable manner.

---

Chapter 2 is adapted from Vardhana, S.A., Arnold, P.K., Rosen, B.P. *et al.* Glutamine independence is a selectable feature of pluripotent stem cells. *Nat Metab* **1,** 676-687 (2019). Reproduced with permission from Springer Nature

Metabolites serve many roles beyond anabolic building blocks. Metabolites also serve as signals or effectors that affect myriad cellular processes, including signal transduction, stress response pathways and chemical modification of proteins and nucleic acids[166,167]. Consequently, regulation of cellular metabolism has emerged as a mechanism to influence cell fate decisions beyond proliferation. In particular, many of the enzymes that modify DNA and histones require metabolites as necessary co-substrates, raising the possibility that metabolic fluctuations shape the chromatin landscape and, in turn, affect gene expression programs[166,168]. Indeed, pathological accumulation of certain metabolites in many malignancies is sufficient to block differentiation and promote transformation by disrupting the normal dynamic chromatin regulation of progenitor cells[169].

Collectively, these findings suggest that how a cell solves the problem of proliferative metabolism may have consequences for the regulation of cell identity. The link between proliferation and cell identity is especially critical in pluripotent stem cells, which proliferate rapidly in culture while retaining the capacity to differentiate into all three lineages of the developing embryo. Pluripotent stem cells utilize glucose and glutamine to fuel proliferation, and perturbations in the metabolism of these nutrients can alter both survival and differentiation[121,170-172]. Notably, glucose-derived acetyl-CoA, the substrate for histone acetyltransferases, and glutamine-derived αKG, a co-substrate of αKG-dependent dioxygenases including the Tet family of methylcytosine oxidases and the Jumonji-domain containing family of histone demethylases, contribute to the regulation of the chromatin landscape, thereby influencing the balance of self-renewal vs differentiation[121,122,173,174].

Given the emerging links between proliferative metabolism and cell identity, we speculated that we could exploit the specific metabolic requirements of particular cell types to favor the enrichment of cells with the highest capacity for self-renewal. Mouse ESCs cultured under conventional conditions including serum and LIF ('S/L') exhibit heterogeneous expression of key pluripotency transcription factors that denote cells with variable propensity for differentiation[175,176]. Addition of inhibitors against MEK and GSK3β ('2i') drive cells into a naïve "ground state" of pluripotency in which cells express relatively homogenous levels of pluripotency transcription factors and are resistant to spontaneous differentiation[161]. We previously showed that addition of 2i to mouse ESCs rewired intracellular metabolic pathways without altering proliferation rate[121]. In particular, 2i-cultured ESCs decreased glutamine oxidation and increased glucose oxidation, enabling an increase in the ratio of αKG/succinate that has been mechanistically linked to the regulation of chromatin and cell identity in a variety of contexts[121,177-179]. However, whether altered metabolic profiles are a specific consequence of altered signal transduction or a general feature of self-renewing ESCs remains an open question. Here we address this issue and reveal that reduced reliance on exogenous glutamine is a fundamental feature of highly self-renewing ESCs. Accordingly, both mouse and human pluripotent stem cells are able to survive and be enriched by transient culture in glutamine-deficient medium. These results demonstrate that defined metabolic profiles are an inherent feature of pluripotent stem cell identity and provide a rationale for the use of metabolic interventions as a method to manipulate heterogeneity in stem cell populations.

## 2.2 Results

### *2.2.1 Glutamine anaplerosis is reduced in highly self-renewing ESCs*

In proliferating mammalian cells *in vitro*, glutamine is the major source of carbon for TCA cycle intermediates[57]. Consequently, most cell lines including ESCs depend on exogenous glutamine for growth and proliferation[57,121,171]. One notable exception is 2i-cultured mouse ESCs in the ground state of pluripotency, which can sustain proliferation in the absence of exogenous glutamine[121]. Previously, we found that addition of 2i reduces the contribution of glutamine-derived carbons to TCA cycle intermediates while increasing the contribution of glucose-derived carbons, thereby reducing reliance on exogenous glutamine to support TCA cycle anaplerosis[121]. To determine whether the effects of 2i on mouse ESC metabolism are a specific consequence of MEK/GSK3β inhibition or a general feature of the metabolic requirements of self-renewing pluripotent cells, we utilized alternative methods to drive ESCs into the ground state of pluripotency. First, we took advantage of a chimeric LIF receptor engineered to respond to granulocyte colony-stimulating factor (GCSF) and harboring a mutation at tyrosine 118 to impair negative feedback by Socs3[180]. Upon treatment with GCSF, cells expressing this chimeric receptor exhibit elevated and sustained JAK/STAT3 signaling (**Figure 2.1a**) and are stabilized in the naïve state of pluripotency regardless of the presence of differentiation-inducing stimuli[181].

To assess glucose and glutamine utilization in these cells, we used gas chromatography-mass spectrometry to trace the fate of uniformly $^{13}C$-labeled glucose or

glutamine. In addition to enhancing expression of the Stat3 target gene *Tfcp2l1* and key transcription factors associated with naïve pluripotency[182] (**Figure 2.1b**), GCSF treatment induced metabolic alterations similar to those triggered by 2i. Specifically, GCSF increased the fraction of TCA cycle metabolites derived from oxidative decarboxylation of glucose-derived pyruvate (m+2 labeled isotopologues) and decreased the fraction of metabolites derived from glutamine catabolism (**Figure 2.1c,d**). Whereas more than 80% of glutamate is derived from glutamine in control ESCs, in line with other cultured mammalian cells, GCSF reduced the fraction of glutamate derived from glutamine to 60% suggesting that GCSF-cultured ESCs can generate glutamate from sources other than glutamine (**Figure 2.1d**). Indeed, when deprived of exogenous glutamine, GCSF-cultured ESCs were able to use glucose and other anaplerotic substrates to maintain intracellular pools of glutamate (**Figure 2.1e**).

Both MEK/GSK3β inhibition and JAK/STAT3 activation promote naïve pluripotency by altering signal transduction. To determine whether direct activation of pluripotency gene networks is sufficient to rewire intracellular metabolic pathways, we ectopically expressed pluripotency-associated transcription factors Klf4 and Nanog (**Figure 2.1f**). Expression of either transcription factor is sufficient to enhance self-renewal[183-185] and induce expression of target genes associated with naïve pluripotency[186,187] (**Figure 2.1g**). Similar to MEK/GSK3β inhibition and JAK/STAT3 activation, overexpression of Klf4 or Nanog increased the fraction of TCA cycle intermediates generated from glucose-derived carbons (**Figure 2.1h**) while decreasing the fraction of TCA cycle intermediates derived from glutamine (**Figure 2.1i**). Under conditions of reduced glutamine anaplerosis, pyruvate carboxylase can partially

compensate to maintain TCA cycle anaplerosis[68]. Accordingly, both JAK/STAT3-stimulated and Nanog/Klf4-expressing cells exhibited an increase in glucose-derived anaplerosis through pyruvate carboxylase (m+3 isotopologues), further underscoring the reduced reliance on glutamine anaplerosis in cells with enhanced pluripotency networks (**Figure 2.1j,k**).

Together, these results suggest that interventions that enhance ESC self-renewal alter the balance of glucose and glutamine utilization in cells independently of changes in culture conditions or proliferation rates (**Figure 2.1l,m**). We have previously represented this metabolic shift—marked by reduced glutamine anaplerosis coupled with enhanced contribution of glucose-derived carbons to TCA cycle metabolites—as a change in the ratio of α-ketoglutarate to succinate[121]. Both JAK/STAT3 induction and Nanog overexpression increase cellular αKG/succinate ratios, while Klf4, which has a more modest effect on glucose and glutamine utilization under routine culture conditions, had no notable effect on this ratio (**Figure 2.1n,o**).

We next asked whether the αKG/succinate ratio varies in correlation with the inherent self-renewal potential of ESCs. The significant population heterogeneity of ESCs cultured under conventional S/L conditions provided an opportunity to determine whether the functional heterogeneity of ESCs is accompanied by metabolic heterogeneity. To this end, we utilized ESCs harboring a GFP reporter at the endogenous *Nanog* locus[188] to sort out cells with the lowest and highest expression of Nanog (**Figure 2.1p, left**). These Nanog-GFP cells have previously been used to illustrate that "Nanog Low" cells are more prone to differentiate than their "Nanog High" counterparts[188,189]. Because of the inherent metastability of S/L-cultured ESCs, within three days of sorting

both “Nanog Low” and “Nanog High” sorted populations had begun to re-establish the variable Nanog expression that characterizes S/L-cultured ESCs (**Figure 2.1p, right**). Nevertheless, the ratio of αKG/succinate was significantly different in the two populations, with Nanog High cells characterized by an elevated αKG/succinate ratio consistent with their enhanced capacity for self-renewal (**Figure 2.1q**). Further supporting a tight correlation between the αKG/succinate ratio and ESC self-renewal, the αKG/succinate ratio increased progressively from Nanog-low to Nanog-intermediate and Nanog-high populations (**Figure 2.1r**).

### *2.2.2 ESCs with enhanced self-renewal exhibit reduced dependence on exogenous glutamine*

We next probed the functional outcome of reduced glutamine anaplerosis in order to further test whether altered proliferative metabolism is an inherent feature of cells with enhanced capacity for self-renewal. Glutamine is required to maintain proliferation, viability and self-renewal of ESCs in traditional S/L culture, and restoring anaplerosis with cell-permeable αKG is sufficient to compensate for glutamine withdrawal (**Figure 2.2a-c**). Therefore, we reasoned that decreased reliance on glutamine anaplerosis would enable cells to better tolerate withdrawal of exogenous glutamine. Indeed, Nanog-high, Nanog-intermediate, and Nanog-low cells were progressively more sensitive to glutamine withdrawal (**Figure 2.2d**). Even after several days in culture, “Nanog High” cells were significantly more resistant to apoptosis triggered by glutamine deprivation than their “Nanog Low” counterparts (**Figure 2.2e,f**). As a control, we included cells cultured in the

presence of 2i, which is sufficient to enable glutamine-independent proliferation[121] and blocked apoptosis induced by glutamine withdrawal (**Figure 2.2e,f**). Similarly, while only 40% of control ESCs remained viable after 48 h of glutamine withdrawal, over 60% remained viable in ESCs with constitutive JAK/STAT3 activation (**Figure 2.2g**). Furthermore, cells with enhanced self-renewal mediated by either JAK/STAT3 activation or Klf4/Nanog overexpression were able to increase the number of viable cells in the culture despite the absence of exogenous glutamine (**Figure 2.2h,i**). Conversely, pharmacologic inhibition of JAK/STAT3 signaling sensitized ESCs to glutamine deprivation (**Figure 2.2j**).

In order to determine which metabolic substrates are limiting for survival under conditions of glutamine deprivation, we cultured cells with cell-permeable analogs of pyruvate, αKG and succinate. Only αKG, the direct substrate for de novo glutamine biosynthesis, was capable of rescuing survival and proliferation in the absence of glutamine, and this rescue was contingent upon the ability of cells to use αKG to engage in de novo glutamine biosynthesis (**Figure 2.2k-p**). Therefore, we asked whether cells with enhanced self-renewal are better able to maintain αKG pools during conditions of glutamine withdrawal. In complete medium, even in cells with enhanced self-renewal, glutamine provides the dominant source of carbon for TCA cycle anaplerosis (**Figure 2.1d,i**). Glutamine withdrawal profoundly reduced steady-state levels of TCA cycle metabolites in all ESC lines tested (**Figure 2.3a,b**). However, both JAK/STAT3-activated and Klf4/Nanog-overexpressing cells were better than their control counterparts at sustaining intracellular pools of αKG, but not downstream TCA cycle metabolites (**Figure 2.3a-d**). As a result, JAK/STAT3 and Klf4/Nanog-overexpressing cells were

better able to maintain an elevated αKG /succinate ratio relative to control ESCs in the absence of exogenous glutamine (**Figure 2.3e,f**).

In addition to serving as an obligate substrate for de novo glutamine biosynthesis, intracellular αKG promotes Nanog expression and increases self-renewal[121,122,174]. Accordingly, while control cells rapidly lost Nanog expression upon glutamine deprivation such that both the overall Nanog expression and the proportion of cells in the Nanog-high population decreased, cells with JAK/STAT3 activation were able to retain Nanog expression and the fraction of cells in the Nanog-high population despite absence of exogenous glutamine (**Figure 2.3 g,h**). Together, these results indicate that stem cells with strengthened pluripotency networks are not only better able to survive glutamine deprivation but also able to withstand the destabilizing effect of loss of glutamine on markers of self-renewal.

The relative glutamine independence of cells with heightened self-renewal led us to speculate that we could exploit this metabolic property to select for cells with the highest potential for self-renewal. To test this idea, we performed competition assays in which GFP-tracked cells expressing empty vector, Klf4 or Nanog were mixed with parental ESCs and the proportion of GFP+ cells was assessed following 48 h culture in glutamine-replete or glutamine-free medium. Expression of Nanog or Klf4 resulted in a notable selective advantage in the absence of exogenous glutamine, such that the proportion of GFP+ cells increased by 41% (Nanog) or 69% (Klf4) relative to cells cultured in the continuous presence of glutamine (**Figure 2.3i**).

We next asked whether glutamine depletion could select for cells with endogenously strengthened self-renewal potential from within the heterogeneous

population characteristic of ESCs. In order to assess population heterogeneity, we developed a quantitative immunofluorescence (IF)-based assay that allowed us to measure the expression levels of pluripotency-associated transcription factors in individual cells. Consistent with previous reports, IF analyses demonstrated that S/L-cultured ESCs exhibit highly variable Nanog expression and relatively homogenous, unimodal Oct4 expression (**Figure 2.4a**)[175,190,191]. Addition of 2i increased both homogeneity and overall level of Nanog expression while having minimal effects on mean Oct4 expression (**Figure 2.4a**). Of note, 2i eliminated a long tail of "Oct4-low" cells representing approximately 10% of S/L-cultured ESC that have previously been reported to represent differentiated cells readily apparent in traditional S/L ESC cultures[190]. As Oct4 is required for pluripotency[192], Oct4-low cells represent the most committed cells within a heterogenous population. Therefore, we asked whether these cells were the most susceptible to glutamine withdrawal. Indeed, within 8 hours of glutamine withdrawal, the proportion of cells in the Oct4-low fraction declined by 50% and 24 h of glutamine deprivation almost entirely eliminated the population of Oct4-low cells (**Figure 2.4b**). Similarly, 24 h of glutamine deprivation eliminated the majority of Nanog-low cells; however, consistent with the observation that Nanog expression is sensitive to glutamine availability, glutamine deprivation also reduced the fraction of cells exhibiting the highest Nanog expression (**Figure 2.4c and Figure 2.5b**).

### *2.2.3 Transient withdrawal of exogenous glutamine selects for ESCs with enhanced self-renewal*

While Nanog expression is metastable and Nanog-low cells can remain undifferentiated and regenerate Nanog-high cells, cells with very low Oct4 represent differentiated cells that cannot self-renew[190]. As these Oct4-low cells were sensitive to glutamine deprivation, we hypothesized that transient glutamine deprivation would eliminate the most committed cells and thereby improve the overall self-renewal potential of a population. This simple procedure entailed subjecting regularly cultured ESCs to glutamine free medium for 24 h ("pulse") and then recovering the cells in complete medium before seeding for follow-up experiments (**Figure 2.4d**). Immunofluorescence assays confirmed that ESCs subjected to a 24 h period of glutamine withdrawal had higher Nanog and Oct4 on a per-cell basis, reflecting elimination of the most committed cells and the restoration of Nanog levels following glutamine re-addition (**Figure 2.4e**). Similarly, Nanog-GFP reporter cells demonstrated that "pulsed" ESCs were more likely to fall into the Nanog-high population than their conventionally cultured control counterparts (**Figure 2.5a,b**). In line with their enhanced expression of pluripotency-associated transcription factors, pulsed cells also exhibited enhanced self-renewal. Colony formation assays analyzed more than one week after the initial pulse demonstrated that pulsed cells were more likely to give rise to undifferentiated colonies and less likely to give rise to differentiated colonies (**Figure 2.5c,d**). Importantly, ESCs subjected to transient glutamine withdrawal remained competent for multi-linage differentiation, giving rise to all three germ layers *in vivo* during teratoma formation (**Figure 2.5e**).

We next performed a series of experiments to clarify how transient glutamine withdrawal improves the self-renewal potential of a population of ESCs. We first

compared pulsed glutamine withdrawal, which eliminates the most committed cells, with interventions that increase ESC self-renewal. In contrast to pulsed glutamine deprivation, pulsed treatment with 2i or αKG—interventions that transiently increase Nanog-GFP expression (**Figure 2.5f,g**)—had no durable effect on the self-renewal capacity of a population of ESC cells (**Figure 2.5h,i**). To confirm that selective elimination of cells that cannot survive glutamine deprivation is required for the benefit of the pulsed glutamine withdrawal, we supplemented cells with cell-permeable αKG at the time of glutamine withdrawal. Blocking cell death during glutamine deprivation eliminated the selective advantage of glutamine deprivation and abrogated the benefit of the pulse (**Figure 2.6a**). Further supporting the notion that the glutamine withdrawal pulse selects for cells that have the endogenous metabolic capacity to sustain *de novo* glutamine synthesis, inhibition of glutamine synthetase concurrent with glutamine withdrawal eliminated surviving cells and completely blocked the ability of transient glutamine withdrawal to improve the population self-renewal capacity (**Figure 2.6a,b**).

Enhanced self-renewal is associated with the ability to sustain intracellular αKG in the absence of exogenous glutamine (**Figure 2.3a-d**). In addition to enabling glutamine synthesis, intracellular αKG can also promote the activity of αKG-dependent chromatin modifying enzymes. The ability of surviving ESCs to preserve intracellular αKG pools to maintain αKG-dependent demethylation reactions may also contribute to the beneficial effect of transient glutamine withdrawal, as addition of the histone H3 trimethylated lysine 27 (H3K27me3) demethylase inhibitor GSK-J4 impaired ESC self-renewal both when administered during transient glutamine withdrawal and in the presence of exogenous glutamine (**Figure 2.6b,c**). In contrast to glutamine, glucose is required for the

viability of ESCs regardless of self-renewal capacity[121]. Accordingly, pulsed glucose withdrawal strongly reduced the colony-formation capacity of mouse ESCs (**Figure 2.6d,e**). Moreover, in line with previous reports that combined glucose and glutamine withdrawal eliminates undifferentiated stem cells[171], pulsed withdrawal of both glucose and glutamine decimated the ability of ESCS to form colonies (**Figure 2.6d**). Together, these findings support a model wherein glutamine deprivation selectively eliminates the most committed cells within a population thereby durably enhancing the overall self-renewal capacity of the remaining cells.

### *2.2.4 Transient glutamine withdrawal enhances mouse somatic cell reprogramming to pluripotency*

Reprogramming of somatic cells to pluripotency represents a major area in which stem cell heterogeneity poses a significant experimental hurdle. Reprogramming is an inefficient process hampered by low efficacy and the persistence of incompletely reprogrammed cells[193]. Interventions that consolidate the pluripotency network enhance reprogramming efficiency: for example, adding 2i to partially reprogrammed cells efficiently promotes the formation of fully reprogrammed cells[194]. Therefore, we tested whether glutamine withdrawal, which selects for cells with strengthened pluripotency gene networks, improves reprogramming efficiency. First, we utilized mouse embryonic fibroblasts (MEFs) harboring a polycistronic cassette enabling doxycycline (dox)-inducible expression of Oct4, Klf4, Sox2 and c-Myc (OKSM) (**Figure 2.7a**)[195]. After eight days of dox-induced OKSM expression, dox removal forces cells to rely on

reactivated endogenous pluripotency networks in order to sustain proliferation and ESC-like features including reactivity to alkaline phosphatase (AP). Consequently, cells that were never exposed to dox are fully AP-negative while control cells exposed to dox exhibit heterogeneous AP staining with numerous variably stained regions punctuated with discrete, well-stained colonies reminiscent of undifferentiated ESC colonies (**Figure 2.7b**). As expected, sustained 2i treatment over the last four days of reprogramming, which helps cells induce and consolidate pluripotency transcriptional networks[196] and blocks spontaneous differentiation[161], resulted in a marked increase in the number of discrete, ESC-like colonies (**Figure 2.7c,d**). Strikingly, just 24 h of glutamine deprivation two days after dox withdrawal was likewise sufficient to increase the overall number of ESC-like AP+ colonies (**Figure 2.7c,d**). Conversely, there was an overall reduction in flat, intermediately stained regions, consistent with selective elimination of cells with weak activation of pluripotency-associated gene networks (**Figure 2.7c**). Notably, transient glutamine withdrawal was just as effective at enhancing reprogramming efficiency as transient treatment with 2i (**Figure 2.7c,d**).

To determine whether glutamine deprivation indeed increased the proportion of cells with activated endogenous pluripotency gene networks, we utilized a second reprogramming system. Here, we infected MEFs harboring a GFP reporter knocked into the endogenous Oct4 locus[197] with viruses carrying dox-inducible OKSM. The Oct4-GFP reporter is helpful in distinguishing fully reprogrammed iPSCs from partially reprogrammed "pre-iPSCs" which, despite having ESC-like morphology, do not activate endogenous pluripotency genes[194] and thus cannot ultimately maintain stable Oct4-GFP expression. Once again, we subjected cells to sustained 2i (7 days) or a 24 h pulse of

either glutamine deprivation ("Pulse -Q") or 2i treatment ("Pulse 2i") beginning 2 days after dox withdrawal (**Figure 2.7e**). Consistent with the observation that glutamine withdrawal eliminates the most committed, Oct4-low cells, the number of Oct4-GFP+ cells decreased transiently during glutamine withdrawal but rebounded within 24 h of recovery in glutamine-replete medium (**Figure 2.7f**). By the end of the experiment, all interventions significantly increased the proportion of cells expressing Oct4-GFP and increased generation of tight, strongly AP+ ESC-like colonies (**Figure 2.7g,h**). Once again, 24 h of glutamine withdrawal was as effective as 24 h of 2i treatment in enhancing generation of Oct4+iPSCs (**Figure 2.7g,h**). Consistent with being fully reprogrammed iPSCs, cells isolated from colonies with compact, ESC-like morphology sustained Oct4-GFP expression for multiple passages in vitro and were able to generate colonies from single cells (**Figure 2.7i,j**) while remaining sensitive to LIF withdrawal (**Figure 2.7i,k**). These data suggest that transient glutamine deprivation is sufficient to increase the fraction of somatic cells that undergo successful reprogramming and further reveal that a metabolic intervention is as effective as well-described alterations in signal transduction pathways at improving reprogramming efficiency.

### *2.2.5 Transient glutamine withdrawal increases markers of pluripotency in human ESCs*

Finally, we asked whether glutamine withdrawal exerted similar effects in human pluripotent stem cells despite the fact that human ESCs are cultured with dramatically different growth factors and represent a more committed, post-implantation stage of

development[158]. As with mouse ESCs, pulsed glutamine withdrawal eliminated a sub-population of cells with low expression of OCT4 (**Figure 2.8a**). Moreover, pulsed glutamine withdrawal resulted in overall enhanced expression of key pluripotency factors SOX2 and OCT4 (**Figure 2.8a,b**). Thus, transient glutamine deprivation represents a general method to enhance expression of key pluripotency markers in both mouse and human pluripotent stem cells under a variety of culture conditions.

## 2.3 Discussion

Here we establish that a distinct metabolic phenotype of naïve mouse embryonic stem cells—reduced reliance on extracellular glutamine as an anaplerotic substrate—is a generalizable feature of cells with enhanced self-renewal. Enhancing ESC self-renewal, either through manipulation of signal transduction or pluripotency-associated transcription factors, is sufficient to alter cellular metabolism to support enhanced survival in the absence of exogenous glutamine. Conversely, cells with weak pluripotency-associated transcription networks are highly glutamine dependent and rapidly die in the absence of exogenous glutamine supplementation. This association between glutamine dependence and pluripotency offers a potent, non-invasive and reversible method to select for stem cells from a heterogeneous population without altering the biological properties of any individual cell. Recent reports demonstrating potential negative effects of other established methods to enhance ground state pluripotency underscore the potential value of this strategy[198,199]. Moreover, the generalizability of this method to human ESCs, in which the conditions required to

achieve the naïve ground state remain a source of continued investigation[200-202] underscores the potential utility of exploiting common metabolic features of cells with enhanced self-renewal.

The molecular drivers of reduced glutamine dependence in pluripotent stem cells remain to be fully elucidated. The subtly different effects of the various interventions that increase self-renewal on ESC metabolism may arise as a result of specific transcriptional profiles driven by each intervention or from additional consequences of altered signaling, such as mitochondrial translocation of STAT3[203]. We previously demonstrated that reduced glutamine anaplerosis enables naïve ESCs to maintain high levels of αKG, a critical co-substrate for demethylation reactions that are required to maintain the unique chromatin landscape of naïve ESCs[121,122,174]. This consequence of reduced glutamine oxidation may provide a general advantage for mouse pluripotent stem cells, particularly given that pluripotency transcription factor binding of DNA is highly associated with local DNA demethylation during the establishment of ground state pluripotency[204-206] and that fluctuations in glutamine-derived αKG levels have profound implications for maintenance of pluripotency[122,174]. However, decreased glutamine anaplerosis may provide additional advantages to naïve ESCs, independent of αKG. The ability to oxidize either glucose or glutamine to maintain energy homeostasis may be of particular value under conditions when either glucose or glutamine becomes limiting[88,207]. Furthermore, decreased glutamine anaplerosis may facilitate the utilization of glutamine for other purposes, including glutamate-dependent uptake of non-essential amino acids[208] as well as nucleotide biosynthesis[209]. Finally, glutamine not used as an anaplerotic substrate can

be utilized for the synthesis of glutathione, which is essential to prevent cysteine oxidation and degradation of Oct4 in human ESCs[210].

Prior studies have identified selective nutrient dependencies that can be exploited to preferentially eliminate ESCs from a population[211]. Our findings offer a strategy for the preferential enrichment of pluripotent ESCs. These results add to an increasing body of work supporting the idea that individual cell types may engage in distinct modes of nutrient utilization to support diverse cell fate decisions, including proliferation as well as regulation of gene expression. Further study of the specialized metabolism of individual cell types may deepen our understanding of how nutrient availability can affect cell fate decisions *in vivo* and provide further opportunities for intervention to select for cells with desired phenotypes.

## 2.4 Experimental Methods

*Cell Culture*

Mouse ESC lines (ESC-1, ESC-2) were previously generated from C57BL/6 x 129S4/SvJae F1 male embryos[121]. Nanog-GFP reporter ESCs were a gift from R. Jaenisch (MIT). Nanog-GFP lines expressing the chimeric LIF receptor (a gift from A. Smith)[180] and ESC-1 lines overexpressing Nanog or Klf4 were previously generated[212]. ESC-1 cells were used for all experiments unless otherwise noted. ESCs were maintained on gelatin-coated plates in serum/LIF (S/L) medium containing Knockout DMEM (Life 10829-018) supplemented with 10% FBS (Gemini), 0.1 mM 2-mercaptoethanol, 2 mM L-glutamine and 1000 U/mL LIF (Gemini). For culture in 2i (S/L+2i), S/L medium was supplemented with 3 μM CHIR99021 (Stemgent) and 1 μM PD0325901 (Stemgent).

Cells were adapted to 2i or GCSF (Gemini) by passaging cells in S/L+2i or S/L+GCSF medium at least three times prior to use in experiments. S/L+2i-adapted cells were maintained for a maximum of nine passages. All cells were routinely tested for mycoplasma. For human embryonic stem cells (hESC) culture, an H1 hESC line (NIHhESC-10-0043) with an inducible Cas9 insertion was used[213]. This line was maintained in chemically defined, serum-free E8 conditions (Thermo Fisher Scientific, A1517001) on tissue culture treated polystyrene plates coated with vitronectin (Thermo Fisher Scientific, A14700). hESCs were split with 0.5mM EDTA at a 1:10-1:20 split ratio every 3-5 days. Cells have been confirmed to be mycoplasma-free by the MSKCC Antibody and Bioresource Core Facility. All experiments were approved by the Tri-SCI Embryonic Stem Cell Research Oversight Committee (ESCRO).

*Nutrient deprivation experiments*

For glutamine deprivation experiments in mouse ESCs, cells were initially plated in standard S/L medium as described above. The following day, cells were washed with PBS and then cultured in experimental medium containing a 1:1 mix of glutamine-free DMEM (Gibco 11960-051) and glutamine-free Neurobasal medium (Gibco 21103-049) including 10% dialyzed FBS, 2-mercaptoethanol, and LIF as described above and containing ("+Q") or lacking ("-Q") L-glutamine (2 mM) as indicated. When indicated, dimethyl-α-ketoglutarate (Sigma 349631) dissolved in DMSO to 1 M was added to a final concentration of 4 mM. For glucose and glutamine deprivation experiments, cells were cultured in medium containing a 1:1 mix of glutamine and glucose-free DMEM (Gibco A14430-01) and glutamine and glucose-free Neurobasal-A medium (Gibco

A24775-01) including 10% dialyzed FBS and all supplements as described above and containing or lacking glucose or glutamine as indicated.

*Embryonic stem cell competition assays*

GFP-negative parental ESCs were mixed with GFP-positive vector or Klf4/Nanog-overexpressing transgenic ESCs and seeded at a concentration of 30,000 total cells per well of a 12-well plate in triplicate. The following day, cells were washed with PBS and then changed to experimental medium containing a 1:1 mix of glutamine-free DMEM and glutamine-free Neurobasal medium including 10% dialyzed FBS, 2-mercaptoethanol, LIF, and containing ("+Q") or lacking ("-Q") L-glutamine as indicated. After 48 h, cells were trypsinized for flow cytometry analysis. Cells were evaluated for GFP and DAPI on either a LSRFortessa or LSR-II machine (Beckman Dickinson). Analysis of DAPI exclusion and GFP mean fluorescence intensity was performed using FlowJo v9.0.

*Glutamine pulse experiments*

For transient glutamine withdrawal ("pulse") experiments, cells were initially plated in standard S/L medium as described above. The following day, cells were washed with PBS and then changed to experimental medium containing a 1:1 mix of glutamine-free DMEM and glutamine-free Neurobasal medium including 10% dialyzed FBS, 2-mercaptoethanol, LIF, and containing ("Ctrl") or lacking ("Pulse -Q") L-glutamine as indicated. 24 h later, cells were washed with PBS and then returned to glutamine-replete medium ("Recover"). 24 h later, cells were subjected to either image analysis, flow

cytometry, or plated for colony formation assays as indicated. For glutamine pulse experiments in human ESCs, cells were initially plated at a density of 300,000 cells/well in a tissue-culture treated polystyrene 12-well plate coated with vitronectin (Thermo Fisher Scientific, A14700) in E8 medium (Thermo Fisher Scientific, A1517001) containing 10 μM ROCK inhibitor Y-27632 (Selleck Chemicals S1049). 24 h after plating, medium was changed to modified E8 medium containing: DMEM high glucose without glutamine (Thermo Fisher 11960044), 10.7 mg/L Transferrin (Sigma T0665), 64 mg/L L-Ascorbic Acid (Sigma A890), 14 μg/L Sodium Selenite (Sigma S5261), 543 mg/L Sodium Bicarbonate (Research Products International 144558), 19.4 mg/L insulin (Sigma I9278), 100 μg/L bFGF (EMD Millipore GF003AF), 2 μg/L TGFβ1 (Peprotech 10021), and 2 mM L-glutamine. After 24 h of culture in modified E8 medium, medium was changed to modified E8 medium containing 2 mM or 0 mM L-glutamine for 24 h. All cells were then changed to modified E8 medium containing 2 mM L-glutamine and cultured for 24 h before harvest for analysis.

*Growth curves*

ESCs were seeded at a density of 30,000-40,000 cells per well of a 12-well plate. The following day, three wells of each line were counted to determine the starting cell number. The remaining cells were washed with PBS and cultured in medium containing a 1:1 mix of glutamine-free DMEM and glutamine-free Neurobasal medium including 10% dialyzed FBS, 2-mercaptoethanol, LIF, and containing or lacking L-glutamine or glucose as indicated and with or without the addition of supplements as indicated: dimethyl-α-ketoglutarate (4 mM), dimethyl-succinate (4 mM), methyl-pyruvate (2 mM), ruxolitinib

(500 nM), methionine sulfoximine (1 mM). Cells were counted on the indicated days thereafter using a Beckman Multisizer 4e with a cell volume gate of 400 – 10,000 fL. Cell counts were normalized to starting cell number. All curves were performed at least two independent times.

*Colony formation assays*

Cells were seeded at 200 or 500 cells per well in six-well plates in standard S/L medium. Medium was refreshed every 2-3 days. Six to seven days after initial seeding, wells were fixed with citrate/acetone/3% formaldehyde for 30 seconds and stained using the Leukocyte Alkaline Phosphatase Kit (Sigma) according to manufacturer instructions. Colonies were scored manually in a blinded fashion.

*Fluorescence activated cell sorting*

For evaluation of cell viability and Nanog-GFP expression, Nanog-GFP ESCs[188] were seeded at a concentration of 40,000 cells per well of a 12-well plate. The next day, cells were washed with PBS and medium was changed to experimental medium containing a 1:1 mix of glutamine-free DMEM and glutamine-free Neurobasal medium including 10% dialyzed FBS, 2-mercaptoethanol, LIF, and containing ("+Q") or lacking ("-Q") L-glutamine as indicated. On the day of analysis, cells were trypsinized and resuspended in FACS buffer (PBS + 2% FBS + 1 mM EDTA) containing DAPI (1 μg/mL). Cells were evaluated for GFP and DAPI on either a LSRFortessa or LSR-II machine and FACSDiva software (Beckman Dickinson). Viable cells were those excluding DAPI (100-fold less than DAPI-positive cells). Nanog-GFP expression was

measured by GFP mean fluorescence intensity and quantified using FlowJo v9.0. All experiments were performed at least two independent times.

For sorting of Nanog High, Nanog Medium, and Nanog Low populations, Nanog-GFP ESCs that were cultured either in S/L medium or adapted to S/L+2i medium as described above were resuspended in sterile FACS buffer containing DAPI. DAPI-excluding cells were evaluated for Nanog-GFP expression on a BD FACSAria III cell sorter (Beckman Dickinson). “Nanog High,” “Nanog Medium,” and “Nanog Low” populations were sorted based on Nanog-GFP expression levels in the highest 10%, median 10%, and lowest 10% of the population, respectively. Following sorting, cells were washed 2x with PBS to remove any residual FACS buffer and plated in 6-well gelatin-coated plates in standard S/L medium with the addition of penicillin/streptomycin (Life technologies). Cells were used 24 to 72 h later for experiments.

Evaluation of apoptosis was performed using an Annexin V Apoptosis Detection kit (BD Biosciences BDB556570). Nanog-GFP ESCs that had been sorted based on Nanog-GFP expression 24 h earlier as described above were plated in standard S/L medium. The next day, cells were washed with PBS and cultured in experimental medium containing a 1:1 mix of glutamine-free DMEM and glutamine-free Neurobasal medium including 10% dialyzed FBS, 2-mercaptoethanol, LIF, and containing (“+Q”) or lacking (“-Q”) L-glutamine as indicated. 24 h later, cells were trypsinized and resuspended in Annexin V binding buffer containing FITC-conjugated Annexin V and propidium iodide (PI) for 15 min at room temperature. Subsequently, excess binding buffer was added and both FITC and PI fluorescence was assessed on an LSRFortessa

machine (Becton Dickinson). Apoptosis was quantified as cells positive for Annexin V based on a 100-fold increase in fluorescence as compared to negative cells.

For evaluation of OCT4 and SOX2 expression in human ESCs, cells were dissociated using TryPLE-Select (Thermo Fisher 12563029) and resuspended in FACS buffer (5% FBS and 5 mM EDTA in FBS). Cells were first stained with LIVE/DEAD Violet (Molecular Probe, L34955, 1:1,000) for 30 min at room temperature. Cells were fixed and permeabilized in 1X fix/perm buffer (eBioscience, 00-5523-00) for 1 h at room temperature. Cells were then stained with fluorophore conjugated antibodies OCT4-APC (eBioscience 50-5841- 82, 1:25) and SOX2-Alexa488 (eBioscience 53-9811-82, 1:100) in permeabilization buffer (Thermo Fisher 00-8333-56) for 30 min at room temperature. Cells were washed by addition of FACS buffer and centrifugation between all steps. Analysis was performed after resuspension in FACs buffer using a BD Fortessa.

*Metabolic analyses*

For steady state TCA cycle metabolite measurements, cells were seeded in standard S/L medium in 6-well plates. 24 h later, cells were washed with PBS and changed into experimental medium containing a 1:1 mix of glutamine-free DMEM and glutamine-free Neurobasal medium including 10% dialyzed FBS, 2-mercaptoethanol, LIF, and 2 mM L-glutamine. The next day, cells were washed with PBS and subjected to the same experimental medium either with or without 2 mM glutamine. 8 h later, metabolites were extracted with 1 mL ice-cold 80% methanol containing 2 µM deuterated 2-hydroxyglutarate (D-2-hydroxyglutaric-2,3,3,4,4-$d_5$ acid, d5-2HG) as an internal standard. After overnight incubation at -80°C, lysates were harvested and

centrifuged at 21,000 *g* for 20 minutes to remove protein. Extracts were dried in an evaporator (Genevac EZ-2 Elite) and resuspended by incubating at 30°C for 2 h in 50 µL of 40 mg/mL methoxyamine hydrochloride in pyridine. Metabolites were further derivatized by addition of 80 µL of MSTFA + 1% TCMS (Thermo Scientific) and 70 µl ethyl acetate (Sigma) and then incubated at 37°C for 30 min. Samples were analyzed using an Agilent 7890A GC coupled to Agilent 5977C mass selective detector. The GC was operated in splitless mode with constant helium gas flow at 1 mL/min. 1 µl of derivatized metabolites was injected onto an HP-5MS column and the GC oven temperature ramped from 60°C to 290°C over 25 minutes. Peaks representing compounds of interest were extracted and integrated using MassHunter software (Agilent Technologies) and then normalized to both the internal standard (d5-2HG) peak area and protein content of duplicate samples as determined by BCA protein assay (Thermo Scientific). Ions used for quantification of metabolite levels are as follows: d5-2HG *m/z* 354; αKG*, m/z* 304; aspartate, *m/z* 334; citrate, *m/z* 465; fumarate, *m/z* 245; glutamate, *m/z* 363; malate, *m/z* 335 and succinate, *m/z* 247. All peaks were manually inspected and verified relative to known spectra for each metabolite.

For isotope tracing studies, cells were seeded in standard S/L medium in 6-well plates. 24 hours later, cells were washed with PBS and changed into experimental medium containing a 1:1 mix of glutamine-free DMEM and glutamine-free Neurobasal medium including 10% dialyzed FBS, 2-mercaptoethanol, LIF, and 2 mM L-glutamine. The next day, cells were washed with PBS and changed into medium containing a 1:1 combination of glucose- and glutamine-free DMEM (Gibco) and glucose- and glutamine-free Neurobasal-A medium (ThermoFisher A24775-01) supplemented with $^{12}$C-glucose

(Sigma) and $^{12}$C-glutamine (Gibco) or the $^{13}$C versions of each metabolite, [U-$^{13}$C]glucose or [U-$^{13}$C]glutamine (Cambridge Isotope Labs) to a final concentration of 20 mM (glucose) and 2 mM (glutamine) for 4 h. Enrichment of $^{13}$C was assessed by quantifying the abundance of the following ions: αKG, *m/z* 304-318; aspartate, *m/z* 334-346; citrate, *m/z* 465-482; fumarate, *m/z* 245-254; glutamate, *m/z* 363-377 and malate, *m/z* 335-347. Correction for natural isotope abundance was performed using IsoCor software[214].

*Immunofluorescence and microscopy*

For mouse ESCs, cells were seeded on 12-well MatTek glass-bottom dishes (P12G-1.0-10-F*) coated in laminin (Sigma, 10 μg/mL in PBS containing $Ca^{2+}$ and $Mg^{2+}$). Cells were fixed in 2% paraformaldehyde for 10 min and then permeabilized in 0.1% tween. Cells were washed with PBS and blocked for 1 h in 2.5% BSA in PBS. After blocking, cells were incubated overnight with primary antibodies diluted in blocking solution. The following antibodies were used: Oct3/4 (Santa Cruz Biotechnologies, sc-5279 at 1:100) and Nanog (eBioscience, 145761-80 at 1:125). The next day, cells were washed with PBS and incubated with secondary antibodies (AlexaFluor 488 or 594 or 647, Molecular Probes) diluted 1:500 in blocking solution for 1 h. For nuclear counterstaining, Hoechst 33342 (Molecular Probes, H3570 at 1 μg/mL) was added to the same secondary solution. After washing with PBS, cells were stored in the dark and imaged within 1 or 2 days. Cells were imaged using an AxioObserver.Z1 epifluorescence inverted microscope with a motorized stage. A CCD attached camera allowed digital image acquisition (Hammamatsu, Orca II). For multi-well and

multidimensional microscopy, definite focus was used and the microscope was programmed to image consecutive image fields (typically 60 per condition). These fields were stitched together using the built-in Axiovision function and exported as raw 16-bit TIFF files without further processing. Typically at least 10,000 cells per well at 200x magnification were imaged.

Image analysis required three steps: cell detection, nuclear segmentation and fluorescence detection in a per cell basis. These steps were implemented on custom-made Matlab (MathWorks) routines. First, cells were detected by adapting a Matlab implementation of the IDL particle tracking code developed by David Grier, John Crocker, and Eric Weeks (http://physics.georgetown.edu/matlab/). This algorithm finds cells as peaks in a Fourier space rather than by thresholding. This approach is less susceptible to problems that typically arise when segmenting large images such as autofluorescent and bright speckles or day-to-day variability in imaging conditions. Cell detection allowed us to count, identify and get the spatial coordinates (centroid) for each cell. Second, nuclear segmentation was achieved by a combination of regular thresholding together with a watershed process based on the distance of cell centroids determined in the previous step. Obtained nuclear regions were then used as masks to quantify pixel intensities for all the fluorescent channels (that reported levels of different proteins) on a per cell basis. We used cumulative values, which were then normalized to the Hoechst staining to correct for area, cell location along the Z-axis and DNA condensation differences. After image analysis, data was processed and plotted also with Matlab. Raw data, image analysis, and data processing routines are available upon request.

*Quantification of gene expression*

RNA was isolated from six-well plates using Trizol (Invitrogen) according to manufacturer instructions. 200 ng RNA was used for cDNA synthesis using iScript (BioRad). Quantitative real-time PCR analysis was performed in technical triplicate using QuantStudio 7 Flex (Applied Biosystems) with Power SYBR Green (Life Technologies). All data were generated using cDNA from triplicate wells for each condition. *Actin* was used as an endogenous control for all experiments.

**Table 1: Chapter 2 qRT-PCR primer sequences**

| | |
|---|---|
| *Actin*, forward | 5'- GCTCTTTTCCAGCCTTCCTT-3' |
| *Actin*, reverse | 5'- CTTCTGCATCCTGTCAGCAA -3' |
| *Nanog*, forward | 5'-AAGATGCGGACTGTGTTCTC-3' |
| *Nanog*, reverse | 5'-CGCTTGCACTTCATCCTTTG-3' |
| *Stat3*, forward | 5'-GTCCTTTTCCACCCAAGTGA-3' |
| *Stat3*, reverse | 5'-TATCTTGGCCCTTTGGAATG-3' |
| *Tfcp2l1*, forward | 5'-GGGGACTACTCGGAGCATCT-3' |
| *Tfcp2l1*, reverse | 5'-TTCCGATCAGCTCCCTTG-3' |
| *Esrrb*, forward | 5'- AACAGCCCCTACCTGAACCT-3' |
| *Esrrb*, reverse | 5'- TGCCAATTCACAGAGAGTGG -3' |
| *Klf4*, forward | 5'-CGGGAAGGGAGAAGACACT-3' |
| *Klf4*, reverse | 5'-GAGTTCCTCACGCCAACG-3' |

| | |
|---|---|
| *Zfp42*, forward | 5'-TCCATGGCATAGTTCCAACAG-3' |
| *Zfp42*, reverse | 5'-TAACTGATTTTCTGCCGTATGC-3' |
| *Fgf5*, forward | 5'-AAACTCCATGCAAGTGCCAAAT-3' |
| *Fgf5*, reverse | 5'-TCTCGGCCTGTCTTTTCAGTTC-3' |

*Western blotting*

Protein lysates were extracted in 1X RIPA buffer (Cell Signaling Technology), separated by SDS–PAGE and transferred to nitrocellulose membranes (Bio-Rad). Membranes were blocked in 3% milk in Tris-buffered saline with 0.1% Tween-20 (TBST) and incubated at 4 °C with primary antibodies overnight. After TBST washes the next day, membranes were incubated with horseradish peroxidase-conjugated secondary antibodies for 2 hours, incubated with ECL (Thermo Scientific) and imaged using an SRX-101A X-Ray Film Processor (Konica Minolta). Antibodies used (at 1:1,000 unless otherwise noted) were: Nanog (AF2729, R&D Systems), Klf4 (ab129473, Abcam), phospho-Stat3 (9138, Cell Signaling Technology), Stat3 (9139, Cell Signaling Technology), and a-Tubulin (1:10,000, T9026, Sigma).

*Reprogramming of mouse embryonic fibroblasts to induced pluripotent stem cells*

For assessment of colony formation, Collagen-OKSM MEFs which contain an optimized reverse tetracycline-dependent transactivator (M2-rtTA) targeted to the constitutively active *Rosa26* locus (https://www.jax.org/strain/006965) and a polycistronic cassette encoding Oct4, Klf4, Sox2, and c-Myc targeted to the *Col1a1* locus

under control of a tetracycline-dependent minimal promoter (tetOP)[195] were plated 10,000 cells per plate on gelatin-coated 6-well plates. 24 h later, cells were washed with PBS and changed to S/L medium containing 1 μg/mL of doxycycline. Medium was replaced every 2 days. After 8 days of culture in S/L medium containing doxycycline, cells were washed with PBS and changed into experimental medium containing a 1:1 mix of glutamine-free DMEM and glutamine-free Neurobasal medium including 10% dialyzed FBS, 2-mercaptoethanol, LIF, and 2 mM L-glutamine without doxycycline. On day 10, all cells were washed with PBS and changed into experimental medium containing 2 mM L-glutamine ("Ctrl"), no glutamine ("Pulse -Q") or 2 mM L-glutamine plus 3 μM CHIR99021 (Stemgent) and 1 μM PD0325901 (Stemgent) ("2i" and "Pulse 2i"). 24 hours later, all cells were washed with PBS and returned to experimental medium containing 2 mM L-glutamine. "2i continuous" treated samples were supplemented with 2i from day 10 for the duration of the experiment. After 14 days, cells were stained for alkaline phosphatase expression and manually scored for colony formation in a blinded fashion as described above.

For assessment of Oct4-GFP expression, MEFs containing a GFP allele targeted to the endogenous *Oct4/Pou5f1* locus (https://www.jax.org/strain/008214)[215] were plated at 20,000 cells per well on gelatin-coated 6-well plates in DMEM medium containing 10% FBS. 24 hours later, cells were infected with lentivirus containing Oct4, Sox2, Klf4, and c-Myc under control of the tetracycline operator and a minimal CMV promoter (a gift from R. Jaenisch, Whitehead Institute, Addgene plasmid #20321). 24 h after infection, plates were washed with PBS and changed to standard S/L medium containing 1 μg/mL of doxycycline. Medium was replaced every 2 days. After 12 days of culture in

S/L medium containing doxycycline, cells were washed with PBS and changed into experimental medium containing a 1:1 mix of glutamine-free DMEM and glutamine-free Neurobasal medium including 10% dialyzed FBS, 2-mercaptoethanol, LIF, and 2 mM L-glutamine without doxycycline. On day 14, all cells were washed with PBS and changed into experimental medium containing 2 mM L-glutamine ("Ctrl"), no glutamine ("Pulse -Q") or 2 mM L-glutamine plus 3 μM CHIR99021 (Stemgent) and 1 μM PD0325901 (Stemgent) ("2i", "Pulse 2i"). 24 hours later, all cells were washed with PBS and returned to experimental medium containing 2 mM L-glutamine. "2i continuous" treated samples were supplemented with 2i from day 14 for the duration of the experiment. On day 20 or other days as indicated, cells were trypsinzed, resuspended in FACS buffer containing DAPI and assessed for GFP expression by flow cytometry as described above. Oct4-GFP positivity was defined by expression of GFP at least 10-fold higher than that of negative cells.

*Teratomas*

ESCs were initially plated in standard S/L medium as described above. The following day, cells were washed with PBS and then changed to experimental medium containing a 1:1 mix of glutamine-free DMEM and glutamine-free Neurobasal medium including 10% dialyzed FBS, 2-mercaptoethanol, LIF, and containing ("Ctrl") or lacking ("Pulse -Q") L-glutamine as indicated. 24 h later, cells were washed with PBS and then returned to glutamine-replete medium ("Recover"). 24 h later, $1 \times 10^6$ cells per replicate were harvested from each group and mixed 1:1 with medium plus Matrigel Basement Membrane Matrix (BD) and injected into the flanks of recipient female SCID littermate

mice aged 8–12 weeks (NOD *scid* gamma JAX 005557 purchased from Jackson Laboratories). All conditions produced tumors in 4–8 weeks. Mice were euthanized before tumor size exceeded 1.5 cm in diameter. Tumors were excised and fixed in 4% paraformaldehyde overnight at 4 °C. Tumors were paraffin-embedded and sections were stained with haematoxylin and eosin according to standard procedures by HistoWiz.

*Statistical analyses*

GraphPad PRISM 7 software was used for statistical analyses except for IF data. Error bars, *P* values and statistical tests are reported in figure legends. Statistical analyses on images were performed using Matlab. We set the threshold to define "Oct4-low" cells as one standard deviation below the mean values of the control population (typically S/L in the presence of glutamine).

## 2.5 Acknowledgments

We thank Dr. Austin Smith (University of Exeter) for the gift of the chimeric LIF receptor and Dr. Rudolf Jaenisch (Whitehead Institute for Biomedical Research) for the gift of the Nanog-GFP ESCs. We also thank Dr. Danwei Huangfu and Bess P. Rosen (Memorial Sloan Kettering Cancer Center) for collaborating with us and performing the human ESC experiments outlined here.

## 2.6 Figures

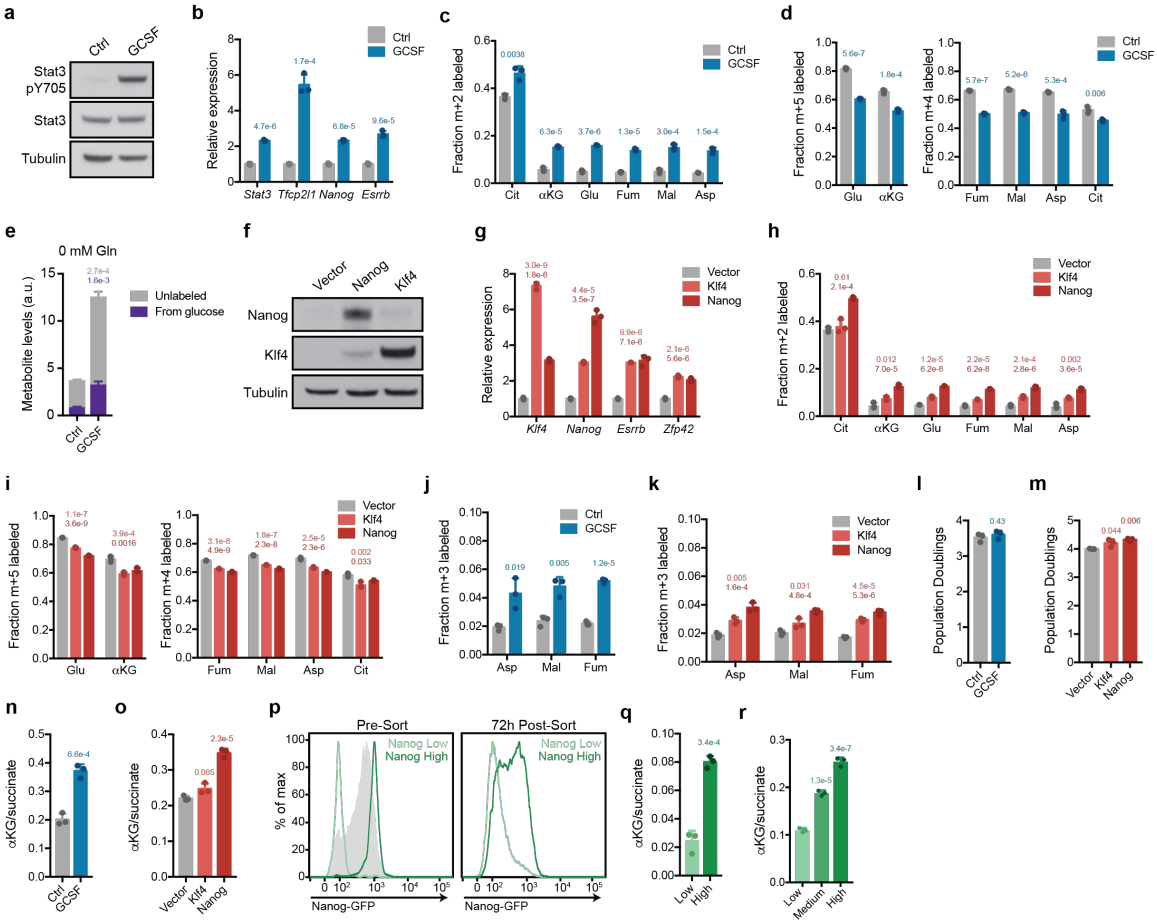


**Figure 2.1 Glutamine anaplerosis is reduced in ESCs with enhanced self-renewal.** **a,b,** Immunoblot of phospho-STAT3 and total STAT3 (**a**) or qRT-PCR of STAT3-target genes and other key pluripotency genes (**b**) in ESCs expressing GCSF-activated LIF receptor transgene cultured with or without GCSF.**c,** Fractional m+2 labeling of citrate (Cit), α-ketoglutarate (αKG), glutamate (Glu), fumarate (Fum), malate (Mal) and aspartate (Asp) in ESCs expressing GCSF-activated LIF receptor transgene cultured with or without GCSF cultured in medium containing [U-$^{13}$C]glucose. **d,** Fractional m+5 labeling of Glu and αKG and m+4 labeling of Fum, Mal, Asp and Cit in ESCs expressing GCSF-activated LIF receptor transgene cultured with or without GCSF cultured in medium containing [U-$^{13}$C]glutamine. **e,** Quantification of glutamate pools in ESCs expressing GCSF-activated LIF receptor transgene cultured with or without GCSF in medium containing [U-$^{13}$C]glucose and following 4 h of glutamine withdrawal. Quantification of pools either labeled or not labeled by glucose-derived [U-$^{13}$C] are indicated. **f,g,** Immunoblot of Nanog and Klf4 (**f**) or qRT-PCR of key pluripotency genes (**g**) in ESCs expressing empty vector, Klf4, or Nanog. **h,** Fractional m+2 labeling of Cit, αKG, Glu, Fum, Mal and Asp in ESCs expressing empty vector, Klf4 or Nanog cultured in medium containing [U-$^{13}$C]glucose. **i,** Fractional m+5 labeling of Glu and αKG and m+4 labeling of Fum, Mal, Asp and Cit in ESCs expressing empty vector, Klf4, or Nanog cultured in medium containing [U-$^{13}$C]glutamine. **j,k,**

Fractional m+3 labeling of Asp, Mal and Fum in ESCs expressing GCSF-activated LIF receptor transgene cultured with or without GCSF (**j**) or ESCs expressing empty vector, Klf4 or Nanog (**k**) cultured in medium containing [U-$^{13}$C]glucose. **l,m,** Population doublings of ESCs expressing GCSF-activated LIF receptor transgene cultured with or without GCSF (**l**) or ESCs expressing empty vector, Klf4 or Nanog (**m**) during 48 h of culture in glutamine-replete medium. **n,o,** Quantification of the αKG/succinate ratio in ESCs expressing GCSF-activated LIF receptor transgene cultured with or without GCSF (**n**) or ESCs expressing empty vector, Klf4 or Nanog (**o**). **p,** Separation of Nanog Low and Nanog High populations by FACS. Left, shaded grey represents the parental Nanog-GFP population cultured in S/L medium; the top 10% and bottom 10% populations (outlined in green) were sorted and plated for subsequent experiments. Right, flow cytometry analysis of Nanog Low and Nanog High populations 72 h after initial sort. **q,** Quantification of the αKG/succinate ratio in Nanog Low and Nanog High populations shown in panel **i** (right). **r,** Quantification of the αKG/succinate ratio in Nanog Low, Nanog Medium, and Nanog High populations. Nanog-GFP ESCs cultured in S/L medium were sorted based on GFP expression; the top 10%, bottom 10%, and median 10% populations were sorted and cultured for 48 h prior to harvesting for metabolite extraction and analysis. *P* values were calculated by unpaired, two-tailed Student's *t*-test (**b-e,j,l,n,q**) or one-way ANOVA with Sidak's multiple comparisons post-test (**g,h,i,k,m,o,r**), relative to control ESCs or Nanog Low ESCs. Data are presented as the mean ± SD, $n = 3$ biologically independent samples from a representative experiment. Panels **a-r** were generated by the author of this thesis, Santosha A. Vardhana, and Lydia W. S. Finley (adapted from Vardhana, Arnold et al., *Nature Metabolism* 2019).

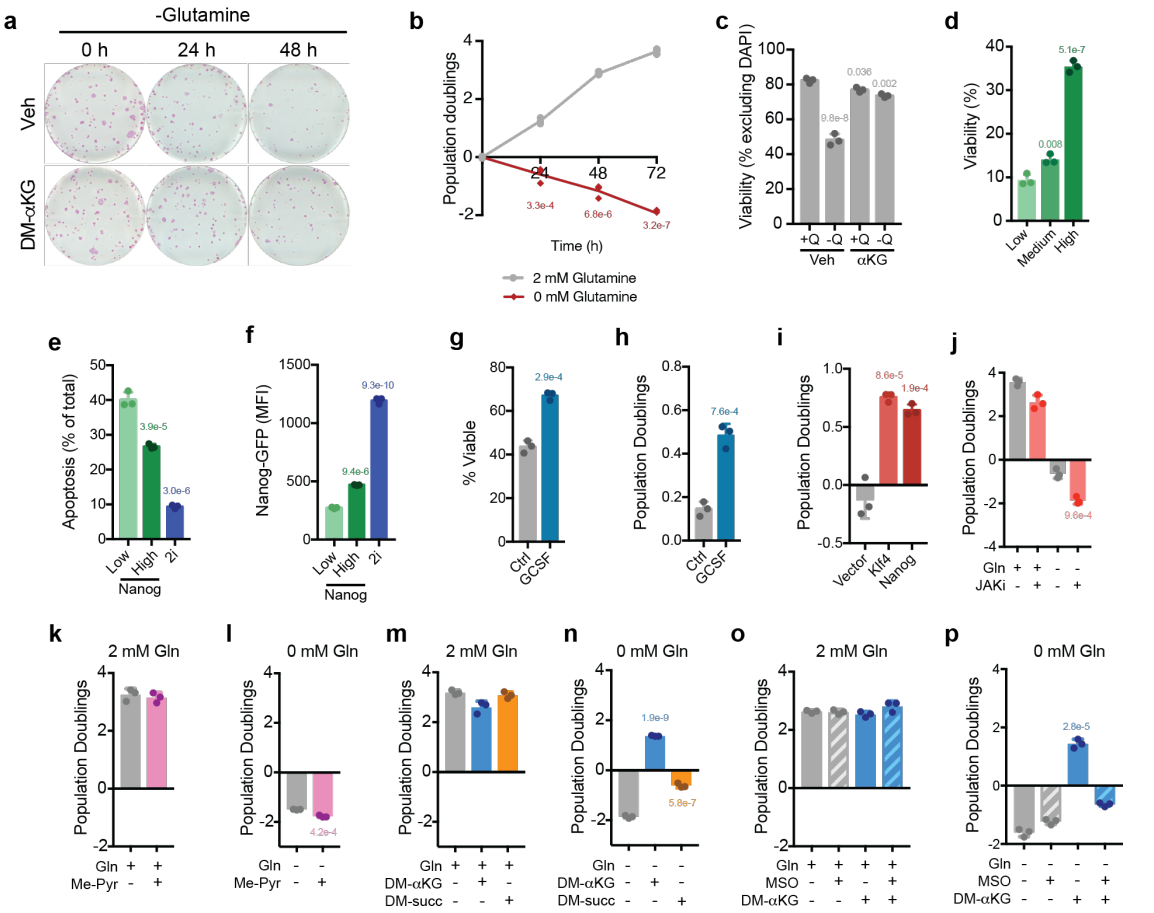


**Figure 2.2 Enhanced self-renewal improves glutamine-independent survival.**
**a,** Alkaline phosphatase staining of colony formation assays of ESCs subjected to transient glutamine withdrawal for the indicated times in the presence of DMSO (Veh) or dimethyl-α-ketoglutarate (DM-αKG). One representative well is shown. Experiment was repeated two independent times with similar results. **b,** Population doublings of ESCs in medium containing or lacking glutamine as indicated. **c,** Viability of ESCs after 24 hours of culture in medium containing glutamine, with or without the addition of 4 mM cell-permeable dimethyl-α ketoglutarate (DM-αKG) as measured by DAPI exclusion. **d,** Quantification of viability in Nanog High, Nanog Medium, and Nanog Low ESCs sorted based on Nanog-GFP expression and deprived of glutamine for 24 h. All cells were recovered in medium 2 mM glutamine for 24 h prior to culturing in media lacking glutamine. **e,** Quantification of apoptosis in Nanog High and Nanog Low ESCs 72 h after sorting based on Nanog-GFP expression. Cells were deprived of glutamine for the final 24 h. **f,** Median Nanog-GFP expression in Nanog High and Nanog Low ESCs 72h after sorting based on Nanog-GFP expression and deprived of glutamine for the final 24 h. **g,h,** Viability (measured by DAPI exclusion) (**g**) or population doublings (**h**) of ESCs expressing GCSF-activated LIF receptor transgene cultured with or without GCSF and deprived of glutamine for 48 h. **i,** Population doublings of ESCs expressing empty vector, Klf4 or Nanog during 48 h of culture in glutamine-free medium. **j,** Population doublings of ESCs cultured for 48 h in glutamine-free medium in the presence or absence of JAKi (ruxolitinib, 500 nM). **k,l,** Population doublings of ESCs cultured for 48 h in the presence or absence of methyl-pyruvate (Me-Pyr, 2 mM) in glutamine-replete (**k**) or glutamine-free (**l**) medium. **m,n,** Population

doublings of ESCs cultured for 48 h in the presence or absence of DM-αKG (4 mM) or dimethyl-succinate (DM-succ, 4 mM) in glutamine-replete (**m)** or glutamine-free (**n**) medium. **o,p,** Population doublings of ESCs cultured for 48 h in the presence or absence of a glutamine synthetase inhibitor methionine sulfoximine (MSO, 1 mM) in glutamine-replete (**o**) or glutamine-free (**p**) medium. *P* values were calculated by unpaired, two-tailed Student's *t*-test (**g,h,j,l,p**) or one-way ANOVA with Sidak's multiple comparisons post-test (**c,d,e,f,i**) relative to Nanog low cells (**d-f**), control ESCs (**g-i**), or cells cultured in glutamine-deficient medium alone (**c,j-p**). Data are presented as the mean ± SD, $n = 3$ biologically independent samples from a representative experiment. Panels **a-p** were generated by the author of this thesis and Santosha A. Vardhana (adapted from Vardhana, Arnold et al., *Nature Metabolism* 2019).

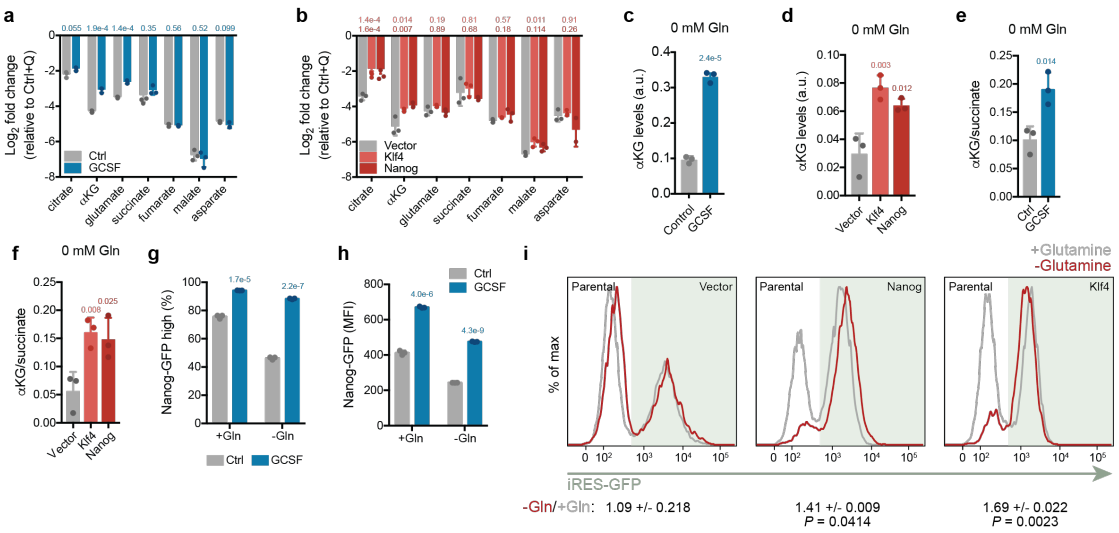


**Figure 2.3 Enhancing ESC self-renewal leads to decreased glutamine anaplerosis.** **a,b,** Relative abundance of intracellular TCA cycle metabolites following 8 h of glutamine withdrawal in ESCs expressing GCSF-activated LIF receptor transgene cultured with or without GCSF (**a**) or ESCs expressing empty vector, Klf4 or Nanog relative to empty vector ESCs (**b**) cultured in glutamine-replete medium. **c,d,** Quantification of intracellular αKG pools, in ESCs expressing GCSF-activated LIF receptor transgene cultured with or without GCSF (**c**) or ESCs expressing empty vector, Klf4 or Nanog (**d**) cultured in medium lacking glutamine for 4 hours. **e,f,** Quantification of the αKG/succinate ratio in ESCs expressing GCSF-activated LIF receptor transgene cultured with or without GCSF following 8 h of glutamine deprivation (**e**) or ESCs expressing empty vector, Klf4 or Nanog following 4 h of glutamine deprivation (**f**). **g,** Fraction of Nanog-GFP ESCs expressing GCSF-activated LIF receptor transgene cultured with or without GCSF exhibiting high Nanog-GFP expression after culture in the presence or absence of glutamine for 48 h. **h,** Median Nanog-GFP expression in ESCs expressing GCSF-activated LIF receptor transgene cultured with or without GCSF and grown in the presence or absence of glutamine for 48 h. **i,** Relative accumulation of GFP+ ESCs expressing empty vector, Klf4, or Nanog compared to parental controls following culture in the presence of absence of 2 mM glutamine (+/-Gln) for 48 h. Ratio represents the fraction of GFP+ cells after culture -Gln relative to the fraction of GFP+ cells after culture +Gln. *P* values were calculated by unpaired, two-tailed Student's *t*-test (**a,c,e,g,h**) or one-way ANOVA with Sidak's multiple comparisons post-test (**b,d,f,i**) relative to control ESCs. Data are presented as the mean ± SD, $n = 3$ biologically independent samples from a representative experiment. Panels **a-i** were generated by the author of this thesis, Santosha A. Vardhana, and Lydia W. S. Finley (adapted from Vardhana, Arnold et al., *Nature Metabolism* 2019).

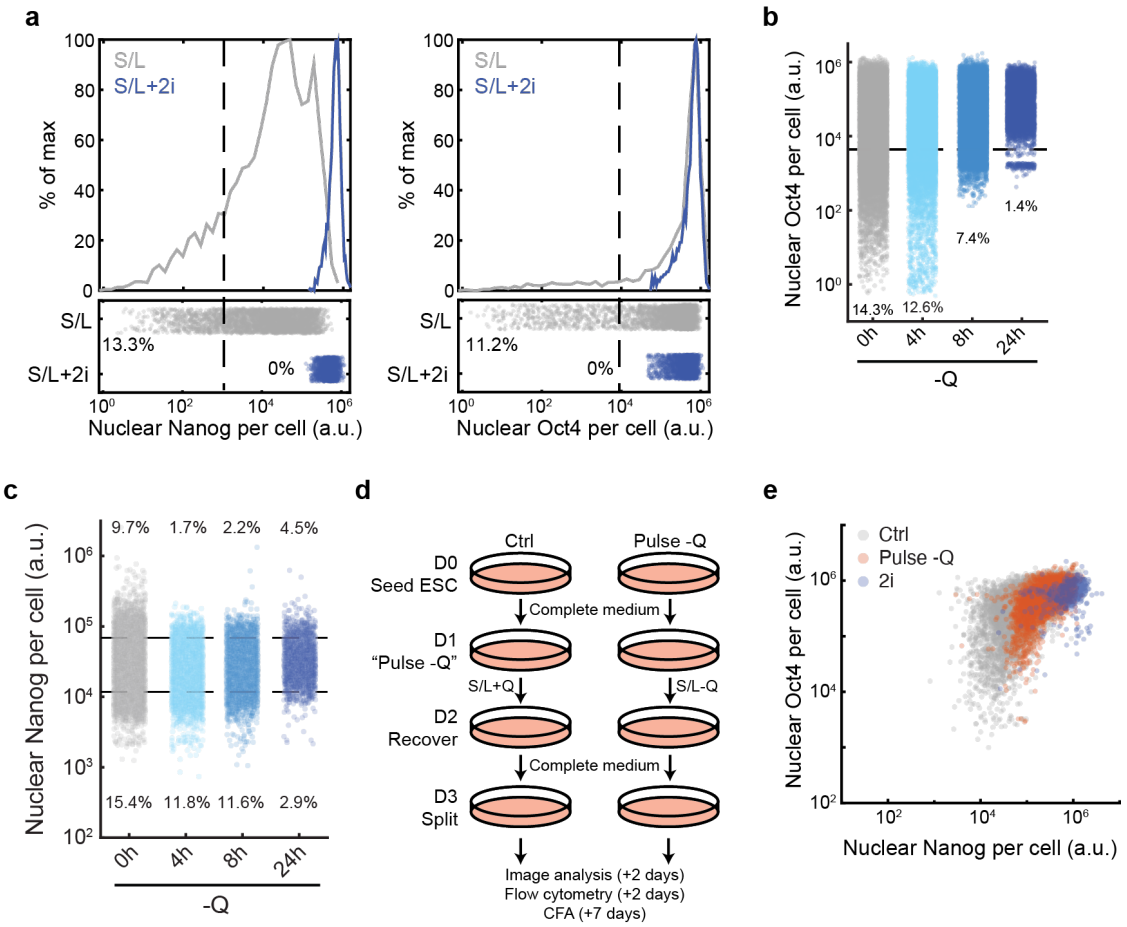


**Figure 2.4. More committed ESCs are most susceptible to elimination upon glutamine deprivation.**

**a,** Quantification of nuclear Nanog (left) and Oct4 (right) immunofluorescence in ESCs cultured in either S/L (grey) or S/L+2i (blue) medium. Dashed line denotes an estimated threshold for "Nanog-low" and "Oct4 low" cells, respectively, defined as cells as one standard deviation below the mean values of the control population (here, S/L). **b,** Quantification of Oct4 immunofluorescence in ESCs cultured in the absence of glutamine (Q) for the indicated times. Dashed line denotes threshold for "Oct4 low" cells, defined as one standard deviation below the mean values of the control population. **c,** Nanog immunofluorescence in ESCs cultured in the absence of glutamine for the indicated times. Dashed lines denote estimated thresholds for "Nanog low" and "Nanog high" cells, defined as cells 0.25 standard deviations below and one standard deviation above the mean values of the control population, respectively. **d,** Experimental design for transient glutamine withdrawal ("Pulse -Q"). **e,** Quantification of Oct4 and Nanog immunofluorescence in control (Ctrl) or S/L+2i (2i)-cultured ESCs or ESCs previously subjected to 24 h of glutamine deprivation (Pulse -Q). Data are presented as >10,000 cells pooled from $n$ = 3 biologically independent samples from a representative experiment (**a-c, e**). Panels **a-e** were generated by the author of this thesis, Santosha A. Vardhana, and Carlos Carmona-Fontaine (adapted from Vardhana, Arnold et al., *Nature Metabolism* 2019).

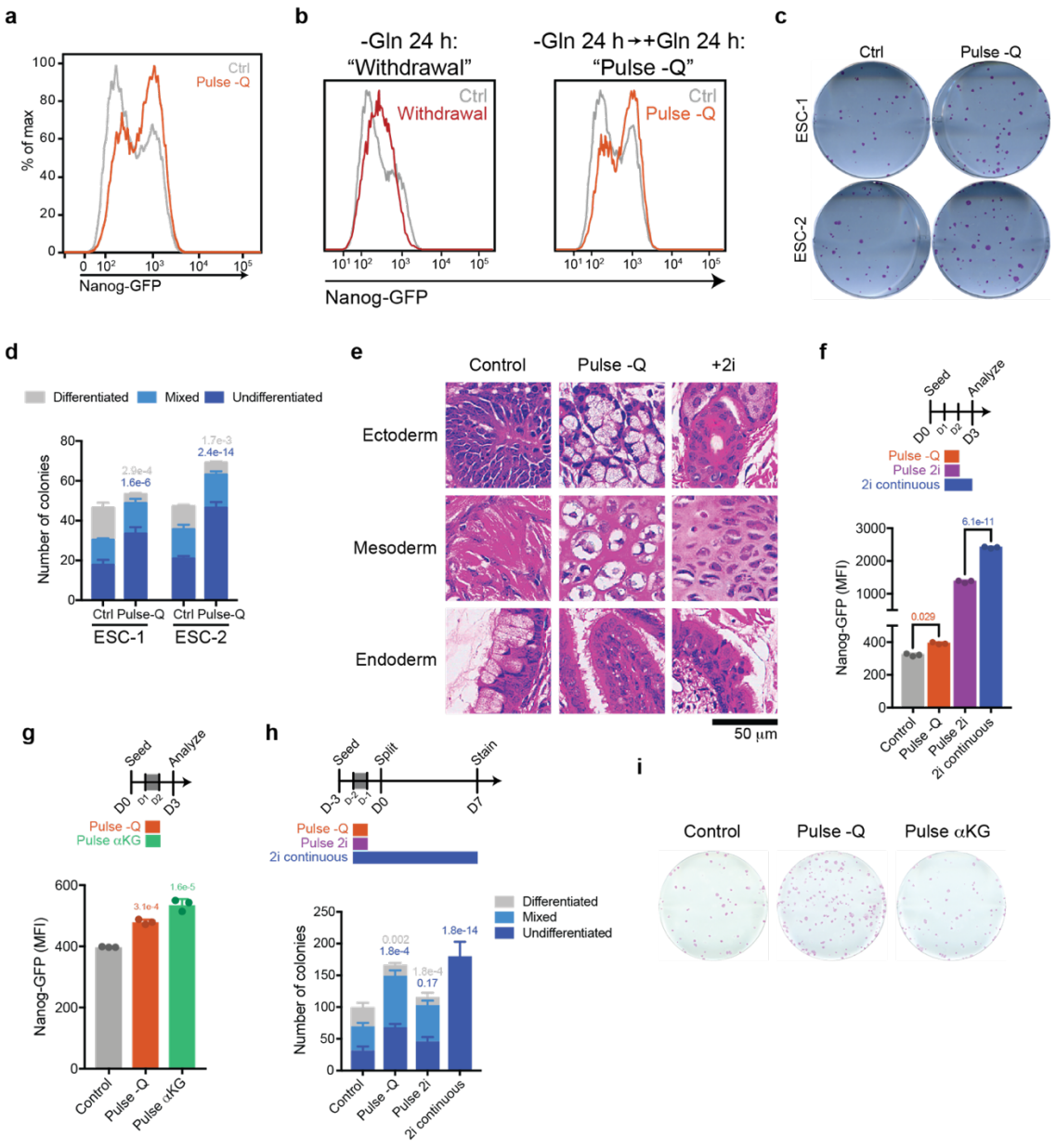


**Figure 2.5 Transient glutamine withdrawal enhances ESC self-renewal.**
**a,** Expression of Nanog-GFP in ESCs subjected to glutamine withdrawal for 24 h and then recovered with glutamine-replete medium for 24 h (Pulse -Q) or maintained in glutamine-replete medium (Ctrl). **b,** Nanog-GFP expression in ESCs subjected to 24 h of glutamine withdrawal (Withdrawal), subjected to 24 h of glutamine withdrawal followed by 24 h of culture in glutamine-replete medium (Pulse -Q), or maintained continuously in glutamine-replete medium (Ctrl). **c,** Alkaline phosphatase (AP) staining of colony formation assays in which two different ESC lines were maintained in glutamine-replete medium (Ctrl) or subjected to transient glutamine withdrawal for 24 h and then recovered in glutamine-replete medium for 24 h prior to plating (Pulse -Q). One representative well is shown. **d,** Quantification of colonies formed in (**c**). Colonies were scored manually as undifferentiated, mixed, or differentiated based on AP staining. **e,** Teratoma formation from ESC grown either in glutamine-replete S/L medium (Control), subjected to 24 h of glutamine deprivation followed by recovery with media containing glutamine

for 24 h (Pulse -Q), or adapted to S/L+2i medium for 3 passages (2i). Representative images of haematoxylin and eosin staining revealing differentiation into ectoderm, mesoderm, and endoderm-derived tissue. Scale bar, 50 μm. **f,** Nanog-GFP expression in ESCs subjected to 24 h of glutamine withdrawal (Pulse -Q) or 24 hours of S/L medium containing 2i and then recovered with glutamine-replete S/L medium for 24 h (Pulse 2i) or maintained continuously in either S/L medium containing glutamine (Control) or S/L medium containing glutamine and 2i (2i continuous). **g,** Expression of Nanog-GFP in ESCs subjected to 24 h of glutamine withdrawal (Pulse -Q) or 24 h of S/L medium containing 4 mM DM-αKG (Pulse αKG) and then recovered with glutamine-replete S/L medium for 24 h. **h,** Quantification of colony formation assays in which ESCs were maintained continuously in S/L medium containing glutamine (Control) or subjected to 24 h of glutamine withdrawal followed by recovery in control medium for 24 h prior to plating (Pulse -Q). Additional manipulations included exposing cells to 2i continuously (2i continuous) or for 24 h (Pulse 2i). **i,** AP staining of colony formation assays in which ESCs subjected to 24 h of glutamine withdrawal (Pulse -Q) or 24 h of S/L medium containing 4 mM DM-αKG (Pulse αKG) and then recovered with glutamine-replete medium for 24 hours or maintained continuously in S/L medium containing glutamine (Control), prior to plating at single cell density. One representative well of a six-well plate is shown. *P* values were calculated by unpaired, two-tailed Student's *t*-test (**d,f**) or one-way ANOVA with Sidak's multiple comparisons post-test relative to control ESCs (**g,h**). Data are presented as the mean ± SEM (**d**) or SD (**f-h**) of $n = 6$ (**d,h**) or $n = 3$ (**f,g**) biologically independent samples from a representative experiment. Panels **a-d** and **f-i** were generated by the author of this thesis and Santosha A. Vardhana; panel **e** was generated by Santosha A. Vardhana (adapted from Vardhana, Arnold et al., *Nature Metabolism* 2019).

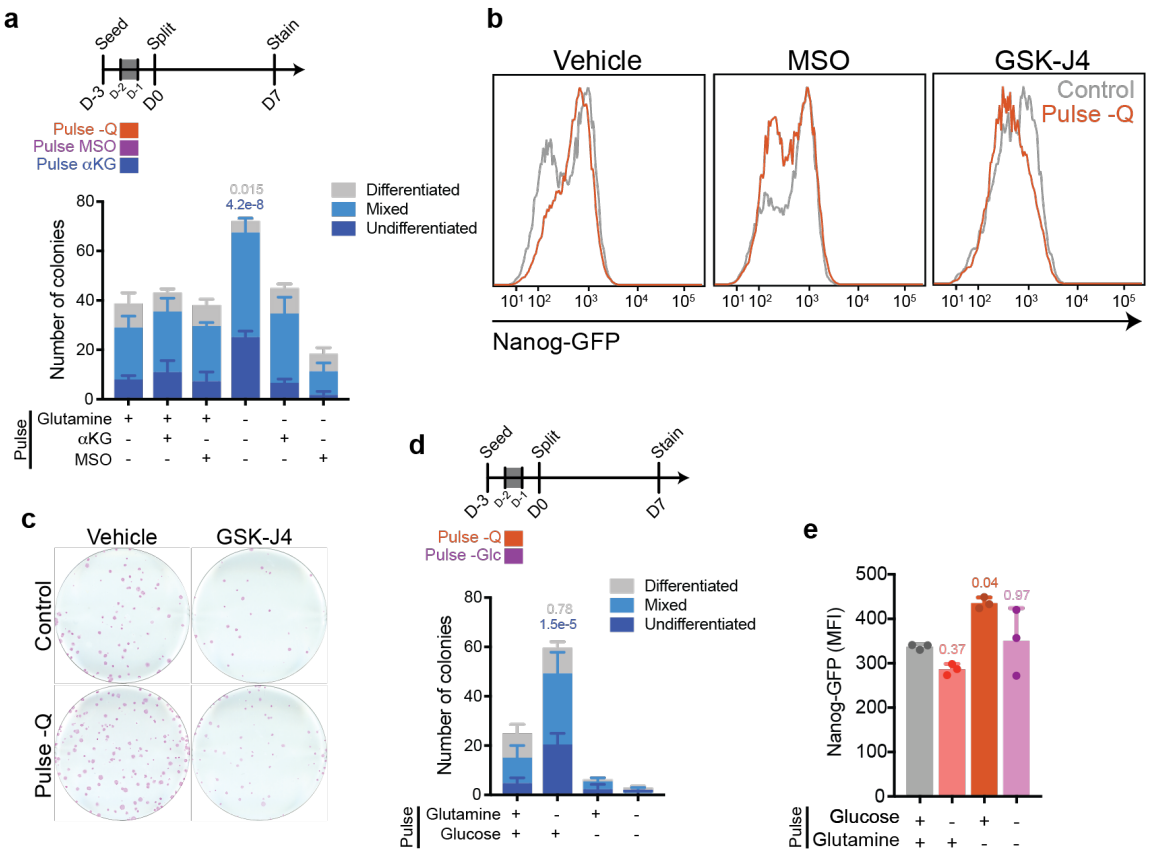


**Figure 2.6 Pulsed glutamine withdrawal selects for ESCs with durable self-renewal.** **a,** Quantification of colony formation assays in which ESCs were maintained continuously in S/L medium containing glutamine or subjected to 24 h of glutamine withdrawal followed by recovery in control medium for 24 h prior to plating (Pulse -Q). Additional manipulations included the addition of 4 mM dimethyl-α-ketoglutarate (DM-αKG) or 1 mM methionine sulfoximine (MSO) during the "pulse." **b,** Nanog-GFP expression in ESCs subjected to 24 h of glutamine withdrawal (Pulse -Q) or maintained in standard glutamine-replete medium (Control) in the presence or absence of MSO or the H3K27me3 demethylase inhibitor GSK-J4 and then recovered with glutamine-replete, inhibitor-free medium for 24 h. **c,** AP staining of colony formation assays in which ESCs subjected to 24 h of glutamine withdrawal (Pulse -Q) or maintained in standard glutamine-replete medium (Control) in the presence or absence of GSK-J4 and then recovered with glutamine-replete, inhibitor-free medium for 24 hours, prior to plating at single cell density. One representative well of a six-well plate is shown. **d,** Quantification of colony formation assays in which ESCs were maintained continuously in S/L medium containing glutamine and glucose or subjected to 24 h of glutamine and/or glucose withdrawal followed by recovery in control medium for 24 h prior to plating. **e,** Nanog-GFP expression in ESCs subjected to withdrawal of either glutamine, glucose, or both glutamine and glucose for 24 h and then recovered with glutamine and glucose-replete medium for 24 h or maintained in glutamine and glucose-replete medium as indicated. *P* values were calculated by one-way ANOVA with Sidak's multiple comparisons post-test (**a,d,e**) relative to control ESCs. Data are presented as the mean ± SD, $n = 3$ biologically independent samples from a representative experiment. Panels **a-e** were generated by the author of this thesis and Santosha A. Vardhana (adapted from Vardhana, Arnold et al., *Nature Metabolism* 2019).

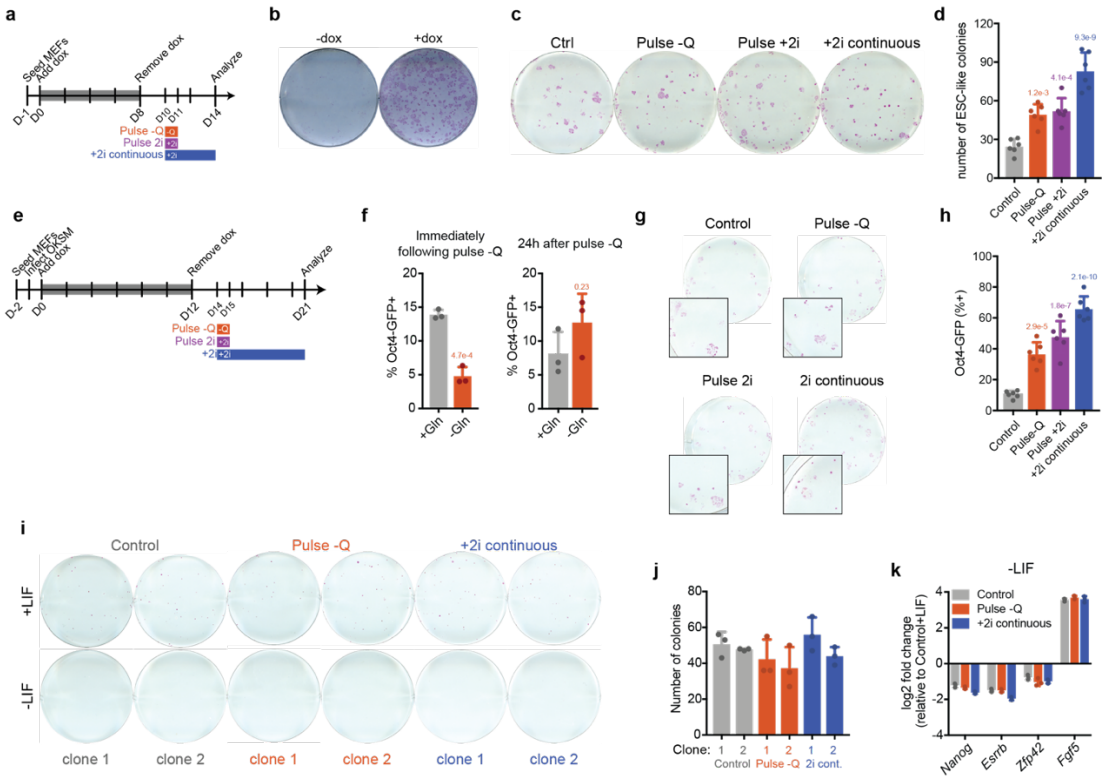


**Figure 2.7 Transient glutamine withdrawal improves mouse somatic cell reprogramming to pluripotency.**

**a,** Experimental design for reprogramming of mouse embryonic fibroblasts (MEFs) expressing doxycycline (dox)-inducible Oct4, Sox2, Klf4 and c-Myc (OSKM). Cells were subjected to dox for 8 days. On day 10, cells were exposed to 2i for the duration of the experiment (+2i), 24 h of glutamine deprivation (Pulse -Q), 24 h of 2i (Pulse 2i), or maintained in glutamine-replete medium (Control). **b,** Alkaline phosphatase (AP) staining of a representative well of mouse embryonic fibroblasts (MEFs) expressing doxycycline (dox)-inducible Oct4, Sox2, Klf4 and c-Myc (OSKM), either treated with (+dox) or without (-dox) doxycycline for 8 days, followed by culture in S/L medium without dox for 6 days. Experiment was repeated twice with similar results. **c,** AP staining of a representative well of cells reprogrammed as described in (**a**). **d,** Quantification of the number of round, highly-AP stained colonies representing successfully reprogrammed colonies formed from OSKM-MEFs 14 d after initial dox addition. **e,** Experimental design for reprogramming of Oct4-GFP MEFs. Cells were infected with OKSM virus the day after seeding. The following day, cells began 12 d of dox exposure. On day 14, cells were exposed to 2i for the duration of the experiment (+2i), 24 h of glutamine deprivation (Pulse -Q), 24 h of 2i (Pulse 2i), or maintained in glutamine-replete medium (Control). **f,** Percentage of Oct4-GFP-expressing cells as an indicator of successful reprogramming on day 15 (immediately following 24 h of culture in medium containing or lacking glutamine), and day 16 (following 24 h of recovery in glutamine-replete medium). **g,** AP staining of a representative well of cells reprogrammed as described in (**e**). **h,** Percentage of Oct4-GFP-expressing cells as an indicator of successful reprogramming at day 21 following initial dox induction. **i,** AP staining of colony formation assays in which successfully reprogrammed OKSM MEFs were plated at single cell density in the presence or absence of LIF. One representative well of a six-well plate is shown. **j,** Quantification of the number of AP stained colonies formed by successfully reprogrammed MEFs in the presence of LIF shown in (**i**). **k,** qRT-PCR of pluripotency associated (Nanog, Esrrb, Zfp42) and epiblast-associated (Fgf5) genes in successfully reprogrammed OKSM MEFs cultured

in the absence of LIF. *P* values were calculated by unpaired, two-tailed Student's *t*-test (**f**) or a one-way ANOVA with Sidak's multiple comparisons post-test (**d,h**) relative to ESCs maintained in glutamine-replete medium. Data are presented as the mean ± SD, $n = 6$ (**d,h**) or $n = 3$ (**f,j,k**) biologically independent samples from a representative experiment. Panels **a-k** were generated by the author of this thesis and Santosha A. Vardhana (adapted from Vardhana, Arnold et al., *Nature Metabolism* 2019).

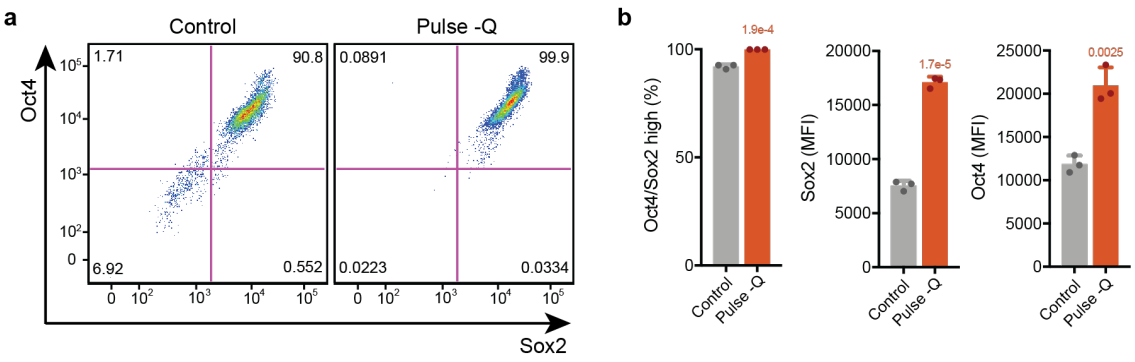


**Figure 2.8 Transient glutamine withdrawal enhances human ESC self-renewal.**
**a,** Expression of OCT4 and SOX2 in human ESCs subjected to glutamine withdrawal for 24 h and then recovered with glutamine-replete medium for 24 h (Pulse -Q) or maintained in glutamine-replete medium (Control). **b,** Quantification of OCT4 and SOX2 mean fluorescence intensity as well as percentage of OCT4/SOX2 high cells as depicted in (**a**). *P* values were calculated by unpaired, two-tailed Student's t-test relative to control ESCs maintained in glutamine-replete medium. Data are presented as the mean ± SD, $n = 3$ biologically independent samples from a representative experiment. Panels **a-b** were generated by Bess P. Rosen with assistance from the author of this thesis (adapted from Vardhana, Arnold et al., *Nature Metabolism* 2019).

# CHAPTER 3: A NON-CANONICAL TCA CYCLE UNDERLIES CELLULAR IDENTITY

## 3.1 Introduction

The TCA cycle is a central metabolic hub, oxidizing nutrients to generate reducing equivalents for energy production and critical metabolites for biosynthetic reactions[83,111]. Despite the ubiquitous importance of TCA cycle products for cell viability and proliferation, mammalian cells display considerable diversity in TCA cycle activity. While our understanding of why TCA cycle activity varies between different cells is incomplete, emerging evidence indicates that the choice of nutrients to fuel the TCA cycle and the activity of many enzymatic reactions is determined by a combination of cell genotype, phenotype, lineage and environmental milieu[83,145,216]. For example, while cancer cells growing in vitro rely on glutamine as a major source of TCA cycle intermediates, glutamine is a relatively minor source of TCA cycle carbon for cancer cells growing in vivo[45,90,147]. Likewise, stem cells alter TCA cycle substrate preferences as they undergo lineage commitment and terminal differentiation[22,152,155]. These observations suggest that cells can selectively engage components of the TCA cycle to meet their metabolic demands.

---

Chapter 3 is adapted from Arnold, P.K.*, Jackson, B.T.*, Paras, K.I. *et al.* A non-canonical tricarboxylic acid cycle underlies cellular identity. *Nature* **603,** 477-481 (2022).

We therefore asked whether enzymes involved in the TCA cycle might form discrete functional modules beyond the canonical pathway delineated by Sir Hans Krebs. The variable essentiality of TCA cycle enzymes across hundreds of cultured cancer cell lines provides a unique opportunity to uncover potential metabolic networks that may underlie cell-state specific metabolic diversity, as genes participating in the same metabolic pathway exhibit similar patterns of essentiality[217,218]. Studies correlating gene essentiality profiles have been used to delineate functional gene networks, enabling identification of previously unknown members of specific metabolic pathways and assigning function to unidentified genes[219,220]. While the enzymes that comprise the TCA cycle are well defined, how these enzymes assemble into functional networks remains largely unexplored.

## 3.2 Results

### *3.2.1 Two modes of TCA cycle metabolism*

To identify metabolic networks involving TCA cycle proteins, we analyzed gene essentiality scores generated by the DepMap project of 769 cancer cell lines[221]. Genes involved in glycolysis, fatty acid oxidation, 1-carbon metabolism or the TCA cycle were clustered based on pairwise correlation of gene essentiality scores (**Figure 3.1**). The vast majority of genes were weakly correlated, perhaps reflecting inherent metabolic plasticity of cultured cells and/or variable isoform expression. Of the clusters that emerged, one contained genes involved in glycolysis and one contained genes required for 1-carbon

metabolism, consistent with the notion that these proteins comprise distinct functional modules (**Figure 3.1**).

In contrast, TCA cycle-associated genes separated into two distinct clusters (**Figure 3.1**). Two-dimensional mapping of correlation distance demonstrated that these clusters were linked by shared co-dependency for *Dld*, a subunit required for both the pyruvate and oxoglutarate dehydrogenase complexes (**Figure 3.2a**). Mapping genes in each cluster onto the canonical TCA cycle pathway underscored a clear division of the TCA cycle into two segments upstream and downstream of citrate (**Figure 3.2b**), raising the question of how cells sustain citrate production if oxidative production of oxaloacetate via the TCA cycle is not tightly linked to citrate synthesis. Suggestively, enzymes involved in cytosolic citrate metabolism, including the mitochondrial citrate/malate antiporter (*Slc25a1*) and ATP citrate lyase (*Acly*) correlated with enzymes involved in citrate production (**Figure 3.2a,b**). Catabolism of mitochondrially-derived citrate via ACL provides the cytoplasmic acetyl-CoA required for protein acetylation and lipid biosynthesis[31,32]. The co-dependency of ACL with TCA cycle enzymes suggests that ACL may also support cellular metabolic demands by forming a non-canonical TCA cycle capable of continuous oxaloacetate regeneration for citrate production.

TCA cycle metabolism can be monitored by tracing [U-$^{13}$C]glucose, which generates m+2 labeled citrate following oxidative decarboxylation of glucose-derived pyruvate (**Figure 3.2c**). Further metabolism by mitochondrial aconitase (ACO2) generates m+2 labeled TCA cycle intermediates, whereas metabolism by ACL liberates m+2 labeled acetyl-CoA, thereby generating unlabeled oxaloacetate and downstream derivatives. Thus, a drop in m+2 labeling of TCA cycle intermediates downstream of

citrate can partly reflect the degree to which cells engage a non-canonical TCA cycle. Many cultured cells show a disconnect between m+2 labeling of citrate and downstream metabolites, as shown in 82 non-small cell lung cancer (NSCLC) lines[222] (**Figure 3.2d**). To determine whether loss of glucose label downstream of citrate is due in part to flux through ACL, we treated select NSCLC lines with an ACL inhibitor. ACL inhibition increased the proportion of malate containing two labeled carbons while having only a minor effect on the fraction of citrate m+2 (**Figure 3.2e**). Although glutamine anaplerosis will also contribute to a disconnect between fractional labeling of citrate and malate[223], ACL inhibition did not uniformly affect glutamine anaplerosis, indicating that the effect of ACL on label loss downstream of citrate is not merely due to glutamine-derived label dilution (**Figure 3.2f**). Within an individual cell line, the degree to which malate is derived from the canonical TCA cycle can be represented as the ratio of malate m+2 relative to citrate m+2 (mal+2/cit+2). ACL inhibition increased the mal+2/cit+2 ratio in all cell lines, consistent with the model that citrate metabolism via ACL represents a significant alternative to the canonical TCA cycle (**Figure 3.2g**).

As an orthogonal labeling strategy, human osteosarcoma cells expressing guinea pig asparaginase[224] were incubated with [U-$^{13}$C]asparagine to produce m+4 labeled citrate, which will lose labeled carbons when metabolized by the traditional TCA cycle (**Figure 3.2h**). Here, ACL inhibition significantly increased the ratio of cit+2/cit+4, reflecting citrate regeneration through the oxidative TCA cycle (**Figure 3.2i,j**). These results are consistent with the model that citrate metabolism via ACL represents a significant alternative to the canonical TCA cycle.

### *3.2.2 ESCs engage a non-canonical TCA cycle*

To determine whether an ACL-mediated TCA cycle exists in non-transformed cells, we traced the fate of [U-$^{13}$C]glucose in mouse ESCs, which self-renew indefinitely when cultured with serum and leukemia inhibitory factor (LIF). Like cancer cells, ESCs exhibit reduced enrichment of malate m+2 relative to citrate that is mitigated by ACL inhibition (**Figure 3.3a,b**). To compare the effects of ACL inhibition with disruption of the canonical TCA cycle, we generated clonal ESC lines with genetic disruption of *Acly* or *Aco2* (**Figure 3.3c,d**). *Acly* disruption had no consistent effect on m+2 enrichment in citrate but consistently increased m+2 enrichment in downstream TCA cycle metabolites, thereby elevating the mal+2/cit+2 ratio (**Figure 3.3e,f**). Conversely, *Aco2* disruption reduced m+2 enrichment of downstream TCA cycle metabolites and decreased the mal+2/cit+2 ratio (**Figure 3.3g**). Surprisingly, despite ACO2's role as a canonical TCA cycle enzyme, *Aco2* disruption minimally affected steady-state levels of TCA cycle metabolites (**Figure 3.3h**). In contrast, *Acly* mutation dramatically altered levels of TCA cycle metabolites associated with cytosolic citrate processing (citrate, malate, aspartate, and fumarate), but not canonical TCA cycle metabolism (succinate, α-ketoglutarate) (**Figure 3.3i**).

To test the hypothesis that a portion of the TCA cycle flows through ACL, we directly tested whether ACL mediates citrate recycling. Cytosolic processing of citrate to malate requires hydride donation from NADH, which can be traced by culturing cells with [4-$^{2}$H]glucose to label up to half of cytosolic NADH pools[225] (**Figure 3.3j**). *Acly* mutation did not affect NADH labeling from [4-$^{2}$H]glucose: both control and edited cells exhibit similar fractional enrichment of NADH and lactate, which becomes labeled when

lactate dehydrogenase reduces cytosolic pyruvate (**Figure 3.3k,l**). *Acly*-edited clones did, however, display significantly lower m+1 enrichment of malate, indicating that wild-type cells generate a portion of malate by reducing ACL-derived cytosolic oxaloacetate (**Figure 3.3m**). Critically, *Acly* mutation more than halved the fraction of labeled citrate, suggesting that cytosolic malate is indeed recycled back into the mitochondria for citrate regeneration, and that this process is impaired in the absence of ACL (**Figure 3.3n-q**). Consistent with impaired transfer of cytosolic reducing equivalents to the mitochondria, *Acly* mutation increased the cytosolic NADH/$NAD^+$ ratio, measured as the ratio of lactate/pyruvate[226], and decreased mitochondrial oxygen consumption (**Figure 3.3r,s**).

To further test whether SLC25A1, ACL and MDH1 form a non-canonical TCA cycle, we generated clonal ESC lines deficient for SLC25A1 and MDH1 (**Figure 3.4a,b**). Deuterated glucose tracing revealed that, like ACL, both SLC25A1 and MDH1 were required for citrate regeneration from cytosolic oxaloacetate (**Figure 3.4c,d**). Accordingly, *Slc25a1*- and *Mdh1*-edited cells exhibited [U-$^{13}$C]glucose labeling patterns consistent with reduced non-canonical TCA cycle activity, including increased enrichment of m+2 isotopologues in TCA cycle metabolites downstream of citrate and an elevated mal+2/cit+2 ratio (**Figure 3.4e-h**). Furthermore, *Slc25a1* and *Mdh1* mutation, like *Acly* mutation, reduced malate and fumarate pools (**Figure 3.4i**). SLC25A1 loss also reduced aspartate pools, but MDH1 loss did not, consistent with its role in the malate-aspartate shuttle that consumes cytosolic aspartate[33]. These data demonstrate that SLC25A1, ACL and MDH1 coordinate a cross-compartment cycle of citrate metabolism.

### *3.2.3 TCA cycle choice is cell-state dependent*

As Krebs originally elucidated the canonical TCA cycle in pigeon breast muscle[27], we assessed TCA cycle choice in C2C12 myoblasts and differentiated myotubes. Compared to myoblasts, myotubes exhibited increased incorporation of glucose-derived carbons into TCA cycle intermediates and a mal+2/cit+2 ratio over five-fold higher than proliferating myoblasts (**Figure 3.5a-c**). Consistent with switching from the non-canonical to canonical TCA cycle, [4-$^{2}$H]glucose tracing revealed diminished production of malate, fumarate and citrate from cytosolic oxaloacetate in myotubes compared with myoblasts (**Figure 3.5d**). To further assess TCA cycle engagement, we engineered cells to express doxycycline-inducible hairpins targeting *Acly* or *Aco2* (**Figure 3.5e**). ACL inhibition significantly increased the mal+2/cit+2 ratio in myoblasts, but not myotubes (**Figure 3.5f-i**). Conversely, while ACO2 inhibition decreased the mal+2/cit+2 ratio in myoblasts, this effect was larger in myotubes, consistent with canonical TCA cycle engagement following differentiation (**Figure 3.5f-i**). As in ESCs, ACL inhibition significantly increased citrate pools and decreased levels of fumarate, malate and aspartate, and this effect was stronger in myoblasts than in myotubes (**Figure 3.5j**). In contrast, ACO2 inhibition had little effect on levels of TCA cycle metabolites in myoblasts and surprisingly tended to increase metabolite levels in myotubes, indicating that ACO2 loss causes greater metabolic disruption in myotubes relative to myoblasts (**Figure 3.5j**). Collectively, these results indicate that the degree to which cells employ the canonical TCA cycle is at least partially determined by cell state.

To identify potential drivers of TCA cycle choice, we compared gene expression with TCA cycle activity in NSCLC lines. TCA cycle genes were highly enriched among

genes positively correlated with the mal+2/cit+2 ratio (**Figure 3.6a**). Similarly, myogenic differentiation significantly induced most TCA cycle genes, many of which are targets of the myogenic transcription factor MYOD[227] (**Figure 3.6b**). As all subunits of the PDHC that initiates carbon entry into the TCA cycle were upregulated upon myogenic differentiation, we tested whether modulating pyruvate entry into the TCA cycle affected TCA cycle choice. Both myoblasts and ESCs treated with dichloroacetate to potentiate PDHC activity[228] increased incorporation of glucose-derived carbons not only into citrate but also into downstream metabolites, thereby elevating the mal+2/cit+2 ratio consistent with enhanced canonical TCA cycle activity (**Figure 3.6c-f**). Reciprocally, pharmacological inhibition of the mitochondrial pyruvate carrier reduced incorporation of glucose-derived carbons into TCA cycle metabolites and repressed the mal+2/cit+2 ratio (**Figure 3.6c-f**). Thus, TCA cycle choice is partly determined by the amount of pyruvate captured for oxidation by PDHC.

### *3.2.4 TCA cycle switch upon pluripotency exit*

We next asked whether changes in TCA cycle configuration are required for changes in cell state. ESCs cultured with LIF and inhibitors against GSK3β and MEK (2i) represent the naïve ground state of pluripotency reminiscent of the pre-implantation epiblast; withdrawal of these factors (-2i/LIF) allows cells to exit the naïve pluripotent state and gain differentiation competence (**Figure 3.7a-c**)[229]. Loss of naïve pluripotency triggers major changes in TCA cycle dynamics: cells induced to exit naïve pluripotency decrease incorporation of glucose-derived carbon while increasing incorporation of

glutamine-derived carbon (**Figure 3.7d,e**), consistent with our previous report demonstrating enhanced glutamine dependence in more committed ESCs[230]. The high mal+2/cit+2 ratio of naïve ESCs is progressively reduced during exit from naïve pluripotency alongside a concomitant increase in production of malate, aspartate, and citrate from cytosolic intermediates (**Figure 3.7f-h**).

Together, these results indicate that ESCs switch from canonical to non-canonical TCA cycle activity as they dismantle naïve pluripotency. Accordingly, metabolic rewiring during exit from pluripotency required ACL: *Acly*-edited clones maintained higher incorporation of glucose-derived carbons and lower incorporation of glutamine-derived carbons than their control counterparts grown -2i/LIF (**Figure 3.8a,b**). ACL loss did not affect the mal+2/cit+2 ratio or steady-state levels of TCA cycle metabolites in naïve ESCs but doubled the mal+2/cit+2 ratio and triggered up to 7-fold changes in TCA cycle metabolite levels in cells grown -2i/LIF (**Figure 3.8c-f**). Consequently, ACL was required for inducing large changes in TCA cycle metabolites and maintaining viability specifically upon exit from naïve pluripotency (**Figure 3.8g,h**). Impaired viability was not due simply to deficient cytosolic acetyl-CoA following ACL loss: exogenous acetate restored histone acetylation and supported *de novo* lipid synthesis—processes requiring cytosolic acetyl-CoA[32]—but minimally rescued viability (**Figure 3.9a-d**). Thus, upon exit from naïve pluripotency, cells rely on the non-canonical TCA cycle to maintain TCA cycle intermediates and cell viability.

### *3.2.5 Exit from pluripotency requires ACL*

We therefore tested whether exit from naïve pluripotency required ACL. Using ESCs harboring a reporter of naïve pluripotency (*Rex1::GFPd2*)[231], we found that the expected reporter downregulation following 2i/LIF withdrawal[229] was almost completely prevented by ACL inhibition (**Figure 3.10a,b**). Similarly, *Acly*-edited clones subjected to 2i/LIF withdrawal demonstrated increased expression of naïve pluripotency genes *Nanog*, *Esrrb* and *Rex1*, impaired induction of the differentiation marker *Sox1*, and enhanced ability to form alkaline phosphatase positive colonies when reseeded into medium containing 2i/LIF (**Figure 3.10c-e**). None of these phenotypes were reversed by exogenous acetate, which rather tended to increase colony formation (**Figure 3.10f-h**) consistent with reports that acetate promotes ESC self-renewal[173]. These results demonstrate that ACL loss selectively impairs metabolism and viability of cells during 2i/LIF withdrawal, independent of cytosolic acetyl-CoA.

Like ACL, neither SLC25A1 nor MDH1 was required for viability of naïve pluripotent ESCs (**Figure 3.11a**). Moreover, like ACL, SLC25A1 loss specifically impaired viability of cells -2i/LIF, but MDH1 loss did not (**Figure 3.11b**). Notably, while ACL, SLC25A1 and MDH1 were all required to sustain TCA cycle metabolites fumarate and malate during exit from naïve pluripotency, only SLC25A1 and ACL were required to maintain aspartate pools (**Figure 3.11c**). Aspartate, which contributes to protein and nucleotide biosynthesis, is a critical output of the TCA cycle in proliferating cells[33,34]. Consistently, when induced to exit naïve pluripotency, both *Acly*- and *Slc25a1*-edited cells, but not *Mdh1*-edited cells, had impaired protein synthesis and reduced proliferation (**Figure 3.11d-g**). Accordingly, while *Acly*- and *Slc25a1*-edited cells preserved naïve pluripotency gene signatures, this effect was blunted in *Mdh1*-edited cells (**Figure**

**3.11h,i**). Together, these results demonstrate that SLC25A1, ACL and MDH1 establish metabolic identity as cells exit the naïve pluripotent state, and cells unable to activate ACL-dependent non-canonical TCA cycle metabolism exhibit compromised viability.

To further test the model that appropriate TCA cycle engagement enables establishment of cell identity, we tested whether efficient induction of the naïve, ground state of pluripotency required canonical TCA cycle metabolism. *Aco2* disruption did not affect proliferation in serum/LIF-cultured ESCs, which exhibit non-canonical TCA cycle activity (**Figure 3.12a**). Supplementing 2i to initiate conversion to naïve pluripotency slowed proliferation of *Aco2*-edited clones and delayed induction of naïve pluripotency markers (**Figure 3.12b,c**). Collectively, these results underscore the role of TCA cycle configuration in facilitating cell state transitions.

## 3.3 Discussion

Here, we identify a non-canonical TCA cycle active in both normal and transformed cells. The possibility of a similar citrate-malate shuttle has been proposed but never demonstrated[31,232,233]. By combining isotope tracing with genetic manipulation of ACL, SLC25A1 and MDH1, we provide direct evidence that the proposed citrate-malate shuttle indeed represents a *bona fide* cycle with differential activity across mammalian cell states. Potential advantages to non-canonical TCA cycle engagement include retaining, rather than combusting, reduced carbon and regenerating cytosolic $NAD^+$ required to sustain glycolysis. By circumventing several steps of the mitochondrial TCA cycle, the non-canonical TCA cycle maintains oxaloacetate regeneration while

minimizing mitochondrial NADH production, which may restrain cell proliferation[234]. Notably, in contrast to their *in vitro* counterparts, cancer cells growing *in vivo* exhibit little loss of glucose label between citrate and malate[90,147], suggesting that differential TCA cycle engagement contributes to the discrepancy between *in vitro* and *in vivo* metabolic phenotypes. Consistently, pancreatic cancer cells are more reliant on *Acly in vitro* and more dependent upon *Aco2 in vivo*[235]. Collectively, these studies underscore the diversity of metabolic strategies that support cellular bioenergetics and reveal that TCA cycle behavior is dynamic and entwined with cell state.

## 3.4 Experimental Methods

*Metabolic co-essentiality analysis and network modeling*

To obtain metabolic gene essentiality scores, we analyzed CERES gene dependency values from the DepMap Portal Project Achilles[236,237] 20Q2 release in which 18,119 genes were perturbed by genome-wide loss of function CRISPR screens in 769 human cancer cell lines. We utilized two gene lists to perform our analysis. To focus on an unbiased set of metabolic genes corresponding to well-defined metabolic pathways, we created a gene set of 122 genes derived from four gene ontology (GO) terms[238,239]: tricarboxylic acid cycle (GO:0006099), canonical glycolysis (GO:0061621), 1-carbon metabolic process (GO:0006730) and fatty-acyl-CoA metabolic process (GO:0035337). To focus more specifically on TCA cycle-centered analysis, we used a list of 27 core TCA cycle genes and then identified the top 10 correlates of these TCA genes using Pearson correlation coefficients from DepMap gene essentiality scores above a minimum

threshold ($r$>0.25). Next, we identified the top 5 correlates of this expanded list again above a minimum threshold ($r$>0.25), resulting in a list of 115 TCA-cycle associated genes.

To examine genetic co-dependency in these gene lists, Pearson correlation coefficients were calculated between metabolic gene essentiality scores across the 769 human cancer cell lines surveyed to generate a correlation matrix heatmap of codependent gene modules. To create the heatmap, the correlations were hierarchically clustered with the UPGMA algorithm using the scipy.cluster.hierarchy.linkage function from the *SciPy* Python package[240], with the method argument set to 'average'. The heatmap was graphed using the *Seaborn* Python package (https://seaborn.pydata.org/citing.html). To visualize codependent gene modules as a network diagram, we utilized the Python package *NetworkX* (http://networkx.org). Genes with no correlation partners or with low correlation scores ($r$ < 0.25) were filtered out, and spring model layouts were generated using the method 'neato' from the Python package Py*Graphviz* (http://pygraphviz.github.io). Graph edges were weighted according to the strength of pairwise gene correlations and the final network diagram was created using the *NetworkX* draw function. Gene clusters with less than 3 members were removed.

*Gene expression correlation*

NSCLC cell line isotope tracing data was obtained from Chen et al., 2019 (ref[222]). Gene expression data was obtained from the DepMap Cancer Cell Line Encyclopedia[241]. For the 68 cell lines present in both datasets, expression of each gene was correlated with

the fractional enrichment of malate m+2 relative to citrate m+2 (Mal+2/Cit+2) derived from [U-$^{13}$C]glucose. Genes were ranked by correlation with Mal+2/Cit+2, and gene set enrichment analysis[242] of the gene set KEGG citric acid (TCA) cycle-associated genes (KEGG_CITRATE_CYCLE_TCA_ CYCLE; M3985) was performed using GSEAPreranked version 4 with default parameters. Data were exported and graphed in GraphPad Prism version 9.

*Cell culture*

Mouse embryonic stem cells (ESCs) were previously generated from C57BL/6 × 129S4/SvJae F1 male embryos[121]. *Rex1::GFPd2* ESCs[231] were a kind gift from Austin Smith, University of Exeter, United Kingdom. All other cell lines were obtained from ATCC. ESCs were maintained on gelatin-coated plates in the following media: serum/LIF, serum/LIF+2i, or 2i/LIF. Serum/LIF medium contained knockout DMEM (catalog no. 10829018; Thermo Fisher Scientific) supplemented with 10% fetal bovine serum (FBS; Gemini), 0.1 mM 2-mercaptoethanol, 2 mM L-glutamine and 1,000 U mlL$^{-1}$ LIF (Gemini). To generate serum/LIF+2i maintenance medium, serum/LIF medium was supplemented with 3 μM CHIR99021 (Stemgent) and 1 μM PD0325901 (Stemgent) (2i). 2i/LIF medium contained a 1:1 mix of DMEM/F-12 (catalog no. 11320033; Gibco) and Neurobasal medium (catalog no. 21103049; Gibco) including N-2 supplement (catalog no. 17502048; Gibo), B-27 supplement (catalog no. 17504044; Gibco), 2-mercaptoethanol, 2 mM L-glutamine, LIF and 2i. To generate ESCs in the naïve ground state of pluripotency, serum/LIF-cultured ESCs were adapted for 3 passages

to serum/LIF+2i medium or 2i/LIF medium. Adapted cells were used for a maximum of 9 passages.

For exit from naïve pluripotency, serum/LIF+2i-cultured ESC were seeded at least 24 h prior to washing with PBS and changing into medium containing a 1:1 mix of glutamine-free DMEM (catalog no. 11960051; Gibco) and Neurobasal medium including N-2 supplement, B-27 supplement, 2-mercaptoethanol and 2 mM L-glutamine at the indicated time before harvest (24 or 40 h). 2i/LIF-cultured ESCs were seeded at least 24 h prior to being washed with PBS and changed into serum-free maintenance medium without 2i or LIF at the indicated time before harvest (12, 24 or 40 h). Unless otherwise noted, cells were adapted to serum/LIF+2i culture prior to exit from naïve pluripotency.

C2C12 cells were maintained at sub-confluence as myoblasts unless otherwise noted. All myoblast experiments were performed in high glucose DMEM supplemented with 10% FBS and 4 mM L-glutamine. For differentiation into myotubes, C2C12 cells were grown to 100% confluence for three days and then washed with PBS and changed into differentiation medium composed of high glucose DMEM supplemented with 2% horse serum (catalog no. 26050070; Gibco), 4 mM L-glutamine and 100X insulin-transferrin-selenium-ethanolamine (ITS-X; catalog no. 51500056; Gibco) for the indicated length of time (3, 5 or 7 days). Differentiation medium was refreshed every day. For non-small cell lung cancer (NSCLC) cell line studies, H2170, A549, and Calu-1 cell lines were thawed and passaged in RPMI-1640 supplemented with 10% FBS before being transitioned to high glucose DMEM supplemented with 10% FBS and 4mM L-glutamine for several passages prior to experiments. 143B cells were maintained in high glucose DMEM supplemented with sodium pyruvate, 10% FBS and penicillin-

streptomycin. Cell lines treated with inhibitors were cultured as described above but medium was supplemented with DMSO, 50 μM BMS-303141 (catalog no. SML0784; Sigma), 5 mM dichloroacetate (catalog no. 3447795; Sigma) or 10 μM UK-5099 (catalog no. 4186; Tocris) for 24 h prior to harvest or for the duration of the exit from pluripotency. All cells routinely tested negative for *Mycoplasma*.

*Generation of clonal ESC lines*

Single guide (sg)RNA sequences targeting *Acly*, *Aco2, Slc25a1, Mdh1* or a control, non-genic region on mouse chromosome 8 (chr8)[243] were cloned into the pSpCas9(BB)-2A-GFP plasmid (PX458, Addgene plasmid number 48138), as previously described[244]. A list of sgRNA sequences is provided in Table 2. ESCs ($4 \times 10^5$ per condition) were electroporated using a 4D-Nucleofector (Amaxa, Lonza) with 5 μg PX458 plasmid encoding Cas9, EGFP and sgRNA sequences. After electroporation, cells were plated onto a layer of irradiated feeder mouse embryonic fibroblasts (MEFs). After 48 h, cells were dissociated with Accutase (Invitrogen) and sorted using the BD FACSAria III sorter (BD Biosciences) to enrich for GFP-positive cells. Approximately 10,000 fluorescence-activated cell sorting (FACS)-sorted GFP-positive cells per experimental condition were immediately re-seeded onto 10 cm plates (on feeder MEFs) to enable clonal growth. After 7 days, individual clones were picked and expanded (initially on feeder MEFs then on gelatin-coated tissue culture plates) and loss of target gene expression was validated by immunoblot (see below).

**Table 2. Chapter 3 sgRNA primer sequences**

| | |
|---|---|
| **Ch.8 control** | CACCGACATTTCTTTCCCCACTGG |
| | AAACCCAGTGGGGAAAGAAATGTC |
| ***Acly* sg1** | CACCGGGGCGTACTTGAACCGGTTC |
| | AAACGAACCGGTTCAAGTACGCCCC |
| ***Acly* sg2** | CACCGGAACCGGTTCAAGTACGCCC |
| | AAACGGGCGTACTTGAACCGGTTCC |
| ***Aco2* sg1** | CACCGGCCAACCAGGAGATCGAGCG |
| | AAACCGCTCGATCTCCTGGTTGGCC |
| ***Slc25a1* sg1** | CACCGCTTCACGTATTCGGTCGGGA |
| | AAACTCCCGACCGAATACGTGAAGC |
| ***Slc25a1* sg2** | CACCGGAGAGGACTATTGTGCGGTC |
| | AAACGACCGCACAATAGTCCTCTCC |
| ***Mdh1* sg1** | CACCGTTGGACATCACCCCCATGAT |
| | AAACATCATGGGGGTGATGTCCAAC |
| ***Mdh1* sg2** | CACCGTCAGCCAGCTGTCGTCTTTC |
| | AAACGAAAGACGACAGCTGGCTGAC |
| **sg*Tcf7l1*** | CACCGCCGGGCAAGCTCATAGTATT |
| | AAACAATACTATGAGCTTGCCCGGC |

*Lentiviral production and infection*

Renilla Luciferase-, *Acly*- and *Aco2*-targeting shRNAs were introduced into C2C12 cells to enable doxycycline-inducible expression using lentiviral LT3GEPIR[245] (see Table 3 for shRNA sequences). Lentivirus was generated by the co-transfection of shRNA-expressing viral vectors with the packaging plasmids psPAX2 and pMD2.G (Addgene) into 293T cells. Virus-containing supernatants were cleared of cellular debris by 0.45-μm filtration and mixed with 8 μg/mL polybrene. C2C12 cells were exposed to viral supernatants for two 24 h periods before being passaged and grown for 24 h in fresh medium and then subjected to antibiotic selection with 1 μg/mL puromycin. Cells were maintained under antibiotic selection until all cells on an uninfected control well were eliminated.

**Table 3. Chapter 3 shRNA sequences**
XhoI/EcoRI for mir30-based shRNA cloning, 5'-3'

| | |
|---|---|
| **shRen** | TGCTGTTGACAGTGAGCGCAGGAATTATAATGCTTATCTATAGT GAAGCCACAGATGTATAGATAAGCATTATAATTCCTATGCCTA CTGCCTCGGA |
| **shAcly-1** | TGCTGTTGACAGTGAGCGCCTGTATTAATCTGATTTTTAATAGT GAAGCCACAGATGTATTAAAAATCAGATTAATACAGTTGCCTA CTGCCTCGGA |
| **shAcly-2** | TGCTGTTGACAGTGAGCGCTGTAACATACAAGTGTTTAAATAG TGAAGCCACAGATGTATTTAAACACTTGTATGTTACAATGCCTA CTGCCTCGGA |
| **shAco2-1** | TGCTGTTGACAGTGAGCGCTCACCAGATCATTCTAGAAAATAG TGAAGCCACAGATGTATTTTCTAGAATGATCTGGTGAATGCCT ACTGCCTCGGA |

| | |
|---|---|
| **shAco2-2** | TGCTGTTGACAGTGAGCGACAGTATGACCAAGTGATTGAATAG TGAAGCCACAGATGTATTCAATCACTTGGTCATACTGGTGCCTA CTGCCTCGGA |

*Viability assays*

Serum/LIF+2i-adapted ESCs were seeded at a density of 24,000 cells per well of a 24-well plate in triplicate or quadruplicate. 24 h later, cells were washed with PBS and changed into either fresh serum/LIF+2i medium or medium containing a 1:1 mix of glutamine-free DMEM and Neurobasal medium including N-2 supplement, B-27 supplement, 2-mercaptoethanol and 2 mM L-glutamine for 40 h. Cells were evaluated for propidium iodide (PI) on an LSRFortessa flow cytometer using FACSDiva software v8.0 (BD Biosciences). Analysis of PI exclusion was performed with FCS Express v.7.05 or FlowJo v10.8.0.

*Growth curves*

ESCs were seeded at a density of 40,000 cells per well of a 12-well plate. The following day, three wells of each line were counted to determine starting cell number. The remaining cells were washed with PBS and changed to either media containing serum+2i/LIF or induced to exit from naïve pluripotency as indicated above. Cells were counted 40 h later using a Beckman Coulter Multisizer 4e with a cell volume gate of 400-10,000 fl. Cell counts were normalized to starting cell number. All curves were performed at least two independent times.

*Naïve pluripotency conversion growth curve*

ESCs were seeded in standard culture medium (serum/LIF) in six-well plates; 48 h later, cells were counted to establish a baseline measurement of proliferation for each line under serum/LIF culturing conditions. Following this count, ESCs were seeded into serum/LIF+2i maintenance medium and passaged and counted every 48 h for 6 days (3 passages). Cumulative population doublings were assessed by summing population doublings measured at each passage. Cells were counted using a Beckman Coulter Multisizer 4e with a cell volume gate of 400-10,000 fl.

*O-propargyl-puromycin (OP-puro) assay*

60 min prior to harvest all cells were washed with PBS and changed into fresh medium. For cycloheximide control samples, 10 μg/mL cycloheximide was added to wells at this time. At 30 min prior to harvest, 20 μM O-propargyl-puromycin (OP-puro, catalog no. HY-15680; MedChemExpress) was added to cells. Cells were harvested and stained with fixable viability dye (catalog no. 65-0863-14; Thermo Fisher Scientific), followed by fixation with 4% PFA in PBS and permeabilization with 0.25% Triton-X-100. Fixed and permeabilized cells were stained using Click-iT Plus Alexa Fluor 647 Picolyl Azid Toolkit (catalog no. C10643; Thermo Fisher Scientific) and AZDye 647 Picoyl Azide (catalog no. 1300-1; Click Chemistry Tools) according to manufacturer's instructions and analyzed on a LSRFortessa flow cytometer using FACSDiva software v8.0 (BD Biosciences). Analysis of OP-puro incorporation was performed with FCS Express v7.05 or FlowJo v10.8.0.

*Rex1::GFPd2 analysis*

On the day of analysis, cells were trypsinized and resuspended in FACS buffer (PBS + 2% FBS + 1mM EDTA) containing 4,6-diamidino-2-phenylindole (DAPI,1 μg/mL). Cells were evaluated for DAPI and GFP on an LSRFortessa flow cytometer using FACSDiva software v8.0 (BD Biosciences). Viable cells were those excluding DAPI. *Rex1::GFPd2* expression was measured by GFP mean fluorescence intensity (MFI) and quantified using FCS Express v7.0.5 or FlowJo v10.8.0.

*Metabolic analyses*

For isotope tracing experiments, ESCs were seeded in standard culture medium in six-well plates; 24 h or 48 h later, cells were washed with PBS and changed into experimental medium containing a 1:1 mix of glutamine-free DMEM and glutamine-free Neurobasal medium including 10% dialyzed FBS, 2-mercaptoethanol, LIF and 2 mM L-glutamine with or without 2i. The next day, cells were washed with PBS and changed into medium containing a 1:1 combination of glucose- and glutamine-free DMEM and glucose- and glutamine-free Neurobasal-A medium including 10% dialyzed FBS, 2-mercaptoethanol, LIF and 2i as specified and supplemented with [$^{12}$C]glucose (Sigma-Aldrich) and [$^{12}$C]glutamine (Gibco) or the labeled versions of each metabolite: [U-$^{13}$C]glucose, [4-$^{2}$H]glucose or [U-$^{13}$C]glutamine (Cambridge Isotope Laboratories) to a final concentration of 20 mM (glucose) and 2 mM (glutamine) for 4 h prior to harvest. To analyze metabolites in serum/LIF+2i-cultured ESCs undergoing exit from pluripotency, ESCs were seeded in maintenance medium in six-well plates overnight. Either 24 or 40 h prior to harvest, cells were washed with PBS and changed into medium containing a 1:1 mix of glutamine-free DMEM and Neurobasal medium including N-2 supplement, B-27

supplement, 2-mercaptoethanol and 2 mM L-glutamine. To analyze metabolites in 2i/LIF-cultured ESCs undergoing exit from pluripotency, ESCs were seeded in serum-free maintenance medium in six-well plates overnight. Either 24 or 40 h prior to harvest, cells were washed with PBS and changed into serum-free maintenance medium without 2i or LIF. In all cases, 4 h prior to harvest, cells were washed with PBS and changed into medium containing a 1:1 combination of glucose- and glutamine-free DMEM and glucose- and glutamine-free Neurobasal-A medium including N-2 and B-27 supplements and 2-mercaptoethanol and supplemented with [$^{12}$C]glucose and [$^{12}$C]glutamine or the labeled versions of each metabolite to a final concentration of 20 mM (glucose) and 2 mM (glutamine).

For mass spectrometric analyses in C2C12 myoblasts and NSCLC cell lines, cells were seeded in six-well plates and medium was changed 24 h later. The next day, cells were washed with PBS and changed into medium containing glucose- and glutamine-free DMEM including 10% dialyzed FBS and supplemented with [$^{12}$C]glucose and [$^{12}$C]glutamine or the labeled versions of each metabolite to a final concentration of 20 mM (glucose) and 4 mM (glutamine) for 4 h prior to harvest. 48 h prior to harvest, myoblasts were supplemented with 1 μg/mL doxycycline to induce shRNA expression. For analysis of myotubes, cells seeded in six-well plates were grown to 100% confluence for 3 days, washed with PBS and changed to differentiation medium that was refreshed every day for 7 days. On the final day of differentiation, cells were washed with PBS and changed to experimental medium described above. For analysis of C2C12 myotube genetic hairpin lines, cells were processed as described above but medium was supplemented with 1 μg/mL doxycycline for the final four days of differentiation to

induce shRNA expression. Cell lines treated with inhibitors were processed as described above but medium was supplemented with DMSO, 50 μM BMS-303141, 5 mM dichloroacetate or 10 μM UK-5099 for 24 h prior to harvest. At harvest, metabolites were extracted with 1 mL ice-cold 80% methanol containing 2 μM deuterated 2-hydroxyglutarate (d-2-hydroxyglutaric-2,3,3,4,4-$d_5$ acid (d5-2HG)). After overnight incubation at −80 °C, lysates were collected and centrifuged at 21,000*g* for 20 min to remove protein. All extracts were further processed by LCMS (for analysis of NADH, lactate and pyruvate (deuterium labeling and lactate/pyruvate ratio) and succinate (deuterium labeling only) or GCMS (for all other analyses) as described below.

143B cells were plated in six-well plates; 24 h later, media was changed to DMEM supplemented with 10% dialyzed FBS, 1 mM asparagine and DMSO or 50 μM BMS-303141. After 20 h, media was changed to DMEM supplemented with 10% dialyzed FBS, 1 mM [U-$^{13}$C]asparagine and DMSO or 50 μM BMS-303141. Cells were extracted with 300 uL 80% methanol containing Valine-D8 as an internal control. 143B extracts were further processed by LCMS, described below.

*Fatty acid analyses*

To analyze fatty acids in serum/LIF+2i-cultured ESCs undergoing exit from pluripotency, ESCs were seeded in maintenance medium in six-well plates overnight. The next day, cells were washed with PBS and changed into medium containing a 1:1 mix of glutamine-free DMEM and Neurobasal medium including N-2 supplement, B-27 supplement, 2-mercaptoethanol and 2 mM L-glutamine. 24 h prior to harvest, cells were washed with PBS and changed into medium containing a 1:1 combination of glucose-

and glutamine-free DMEM and glucose- and glutamine-free Neurobasal-A medium including N-2 supplement, B-27 supplement, 2-mercaptoethanol, 2mM L-glutamine and 20 mM glucose supplemented with 5 mM [1,2-$^{13}$C]sodium acetate (Cambridge Isotope Laboratories). At harvest, lysates were collected in PBS and centrifuged at 6,800 *g* for 5 min to pellet cells. To isolate fatty acids, cell pellets were resuspended in 400 µl HPLC grade methanol followed by 800 µl HPLC grade chloroform and samples were vortexed for 10 min at 4°C. 300 µl HPLC grade water then added to induce phase separation. 800 µl of the bottom chloroform layer was moved to a new tube and lyophilized. Dried samples were saponified by resuspending in 1 ml of 80% methanol with 0.3 M KOH and heating at 80°C for 1 h in a glass vial. Next, 1 ml of HPLC grade hexanes were added to the vial and briefly vortexed. 800 µl of the top hexane layer was moved to a new tube and lyophilized. Extracts were then further processed by LCMS, described below.

*Gas chromatography-mass spectrometry (GCMS) analysis*

Extracts were dried in an evaporator (Genevac EZ-2 Elite) and resuspended by incubating with shaking at 30 °C for 2 h in 50 µl of 40 mg ml$^{-1}$ methoxyamine hydrochloride in pyridine. Metabolites were further derivatized by adding 80 µl of N-methyl-N-(trimethylsilyl) trifluoroacetamide + 1% TCMS (Thermo Fisher Scientific) and 70 µl ethyl acetate (Sigma-Aldrich) and then incubated at 37 °C for 30 min. Samples were analyzed using an Agilent 7890A Gas Chromatograph coupled to an Agilent 5977C mass selective detector. The gas chromatograph was operated in splitless injection mode with constant helium gas flow at 1 ml min$^{-1}$; 1 µl of derivatized metabolites was injected onto an HP-5ms column and the gas chromatograph oven temperature ramped from 60 to

290 °C over 25 min. Peaks representing compounds of interest were extracted and integrated using the MassHunter software v.B.08 (Agilent Technologies) and then normalized to both the internal standard (d5-2HG) peak area and protein content of triplicate samples as determined by bicinchoninic acid assay (Thermo Fisher Scientific). Steady-state metabolite pool levels were derived by quantifying the following ions: d5-2HG, 354 *m/z*; αKG, 304 *m/z*; aspartate, 334 *m/z*; citrate, 465 *m/z*; fumarate, 245 *m/z*; malate, 335 *m/z*; and succinate, 247 *m/z.* All peaks were manually inspected and verified relative to known spectra for each metabolite. Enrichment of [$^{13}$C] or [$^{2}$H] was assessed by quantifying the abundance of the following ions: aspartate, 334-346 *m/z*; citrate, 465–482 *m/z*; fumarate, 245–254 *m/z*; and malate, 335–347 *m/z*. Correction for natural isotope abundance was performed using IsoCor software v.1.0 or v.2.0[246].

*Liquid chromatography-mass spectrometry (LC-MS) analysis*

Lyophilized samples were resuspended in 80% methanol in water and transferred to liquid chromatography-mass spectrometry (LCMS) vials for measurement by LCMS. Metabolite quantitation was performed using a Q Exactive HF-X Hybrid Quadrupole-Orbitrap Mass Spectrometer equipped with an Ion Max API source and H-ESI II probe, coupled to a Vanquish Flex Binary UHPLC system (Thermo Scientific). Mass calibrations were completed at a minimum of every 5 days in both the positive and negative polarity modes using LTQ Velos ESI Calibration Solution (Pierce).

Polar Samples: Polar samples were chromatographically separated by injecting a sample volume of either 1 µL in the MS1 mode or 5 µL in the SIM mode into a SeQuant ZIC-

pHILIC Polymeric column (2.1 x 150 mm 5 mM, EMD Millipore). The flow rate was set to 150 mL/min, autosampler temperature set to 10 °C, and column temperature set to 30 °C. Mobile Phase A consisted of 20 mM ammonium carbonate and 0.1 % (v/v) ammonium hydroxide, and Mobile Phase B consisted of 100 % acetonitrile. The sample was gradient eluted (%B) from the column as follows: 0-20 min.: linear gradient from 85 % to 20 % B; 20-24 min.: hold at 20 % B; 24-24.5 min.: linear gradient from 20 % to 85 % B; 24.5 min.-end: hold at 85 % B until equilibrated with ten column volumes. Mobile Phase was directed into the ion source with the following parameters: sheath gas = 45, auxiliary gas = 15, sweep gas = 2, spray voltage = 2.9 kV in the negative mode or 3.5 kV in the positive mode, capillary temperature = 300 °C, RF level = 40 %, auxiliary gas heater temperature = 325 °C. Mass detection was conducted with a resolution of 240,000 in full scan mode or 120,000 in SIM mode, with an AGC target of 3,000,000 and maximum injection time of 250 msec for the full scan mode, or 100,000 and 100 msec for the SIM mode. Metabolites were detected over mass range of 70-1050 *m/z* in full scan positive mode, or SIM in positive mode using a quadrupole isolation window of 0.7 *m/z*.

Non-Polar Samples: Non-polar samples were chromatographically separated by injecting 2 µL into an Accucore Vanquish C18+ column (2.1 x 100 mm, 1.5µm particle size, p/n 27101-102130, Thermo Scientific). The autosampler temperature was set at 10°C and the flow rate was 500 µL/minwith the column temperature set at 50°C. The largely isocratic gradient consisted of a mixture of water/5 mM ammonium acetate as “A” and acetonitrile as “B” where between 0-6.5 min, the solvent composition was held at 60% “B”, followed by a change to 98% “B” between 6.5-6.6 min. The composition was held at 98% “B”

between 6.6-9.0 min, and then returned back to starting conditions at 60% “B” between 9.0-9.1 minutes. It was then held for an additional 4.4 minutes to re-equilibrate the column for the next run. Non-polar analytes were detected in the negative polarity mode at a resolution of 240,000 in the full scan setting, using a mass range of 240-650 m/z. The AGC target value was 3,000,000 with a maximum injection time of 200 ms. The chromatography peak width setting was 10 seconds (FWHM), and data were collected in profile mode. The parameters for the H-ESI source were as follows: sheath gas flow rate of 53 units, aux gas flow rate of 14 units, sweep gas flow rate of 3 units, with the spray voltage set at 3.00 kV. The funnel RF level was set at 40%, and the capillary and auxiliary gas heater temperatures were held at 300°C and 400°C respectively. Quantitation of all metabolites was performed using Tracefinder 4.1 (Thermo Scientific) referencing an in-house metabolite standards library using ≤ 5 ppm mass error. Data from stable isotope labeling experiments includes correction for natural isotope abundance using IsoCor software v.2.2.

*Oxygen consumption*

Oxygen consumption rate (OCR) was measured using a Seahorse XFe96 Extracellular Flux Analyzer (Agilent Technologies). ESCs were plated on gelatin-coated tissue culture-treated XF96 96-well plates (Agilent Technologies) at $2 \times 10^4$ cells per well in standard maintenance medium. The following day, cells were washed twice with assay medium (Seahorse XF DMEM Medium supplemented with 10 mM glucose) and changed to assay medium containing 2 mM L-glutamine for 2 h prior to the assay. Baseline measurements of OCR were obtained three times. Following the assay, protein content

was determined and averaged per condition and the OCR measurements were normalized to these values. The third baseline OCR reading was averaged across all 12 replicates; averaged values from three independent experiments are shown.

*Western blotting*

Protein lysates were extracted in 1X RIPA buffer (Cell Signaling Technology), separated by SDS–polyacrylamide gel electrophoresis and transferred to nitrocellulose membranes (Bio-Rad). For histone blots, cell pellets were flash frozen in ethanol and resuspended in Laemmli buffer for sonication. Samples were mixed with 5% BME and 0.01% bromophenol blue prior to identical separation as for protein lysates. Membranes were blocked in 3% milk in Tris-buffered saline with 0.1% Tween 20 (TBST) or 5% BSA in TBST and incubated at 4 °C with primary antibodies overnight. After TBST washes the next day, membranes were incubated with horseradish peroxidase-conjugated secondary antibodies (mouse catalog no. NA931; rabbit catalog no. NA934; Cytiva) for at least 2 h, incubated with enhanced chemiluminescence (Thermo Fisher Scientific) and imaged with an SRX-101A X-ray Film Processor (Konica Minolta).

The antibodies used (at 1:1,000) were: ACL (catalog no. 4332; Cell Signaling Technologies), ACO2 (catalog no. MA1-029; ThermoFisher ), SLC25A1 (catalog no. 15235-1-AP; ProteinTech), MDH1 (catalog no. sc-166879; Santa Cruz Biotechnology), ACACA (catalog no. MAB6898; R&D Systems), AceCS1/ACSS2 (catalog no. 3658; Cell Signaling Technologies), TCF7L1 (catalog no. sc-166411; Santa Cruz Biotechnology), Myogenin/MYOG (catalog no. 14-5643-82; ThermoFisher), MYH3 (catalog no. 22287-1-AP; ProteinTech), Vinculin (catalog no. V9131; Sigma), Tubulin (catalog no. T9026; Sigma-Aldrich), H3K9ac (catalog no. 9469; Cell Signaling

Technology), H3K14ac (catalog no. 07-353; Millipore Sigma), H3K27ac (catalog no. 39133; Active Motif), H4K16ac, (catalog no. 39167; Active Motif), H3 (catalog no. Ab1791; Abcam), and H4 (catalog no. 07-108; Millipore Sigma). C2C12 myoblast genetic hairpin lines were maintained in medium supplemented with 1 μg/mL doxycycline for 48 h prior to protein lysate extraction to induce shRNA expression.

*Colony formation assay*

ESCs adapted to 2i/LIF or serum/LIF+2i were subjected to exit from pluripotency in triplicate for 12, 24 or 40 h. On the day of harvest, cells were counted and re-seeded at a density of 2,000 cells per well in technical triplicate in maintenance medium containing 2i and LIF. Medium was refreshed every 3 days. Six days after initial seeding, cells were fixed with citrate/acetone/3% formaldehyde for 30 s and stained with the Leukocyte Alkaline Phosphatase Kit (Sigma-Aldrich) according to the manufacturer's instructions. Colonies were quantified using ImageJ's particle analysis function and technical triplicates were averaged for each condition.

*Quantification of gene expression*

RNA was isolated from six- or twelve-well plates using TRIzol (Invitrogen) according to the manufacturer's instructions and 200 ng RNA was used for complementary DNA (cDNA) synthesis using the iScript cDNA Synthesis Kit (Bio-Rad). Quantitative real-time PCR analysis was performed in technical triplicate using QuantStudio 5 or 6 Flex (Applied Biosystems) with Power SYBR Green Master Mix (Thermo Fisher Scientific). All data were generated using cDNA from 3 independent

wells for each condition. Actin was used as an endogenous control for all experiments. See Table 3 for qRT-PCR primer sequences.

**Table 4. Chapter 3 qRT-PCR primer sequences**

| | |
|---|---|
| *Actin*, forward | GCTCTTTTCCAGCCTTCCTT |
| *Actin*, reverse | CTTCTGCATCCTGTCAGCAA |
| *Nanog*, forward | AAGATGCGGACTGTGTTCTC |
| *Nanog*, reverse | CGCTTGCACTTCATCCTTTG |
| *Esrrb*, forward | AACAGCCCCTACCTGAACCT |
| *Esrrb*, reverse | TGCCAATTCACAGAGAGTGG |
| *Klf2*, forward | TAAAGGCGCATCTGCGTACA |
| *Klf2*, reverse | CGCACAAGTGGCACTGAAAG |
| *Rex1*, forward | TCCATGGCATAGTTCCAACAG |
| *Rex1*, reverse | TAACTGATTTTCTGCCGTATGC |
| *Klf4*, forward | CGGGAAGGGAGAAGACACT |
| *Klf4*, reverse | GAGTTCCTCACGCCAACG |
| *Sox1*, forward | CCTCGGATCTCTGGTCAAGT |
| *Sox1*, reverse | GCAGGTACATGCTGATCATCTC |
| *Otx2*, forward | GACCCGGTACCCAGACATC |
| *Otx2*, reverse | GCTCTTCGATTCTTAAACCATACC |
| *Fgf5*, forward | AAACTCCATGCAAGTGCCAAAT |
| *Fgf5*, reverse | TCTCGGCCTGTCTTTTCAGTTC |
| *Oct4*, forward | TGGATCCTCGAACCTGGCTA |

| | |
|---|---|
| *Oct4*, reverse | CCCTCCGCAGAACTCGTATG |

*RNAseq of myoblasts and myotubes*

RNA was isolated as described above and quantified using a Qubit 3.0 fluorometer. RNA-seq libraries were generated using TruSeq Stranded mRNA Library Prep Kit (catalog no. 20020594; Illumina) according to the manufacturer's instructions. Samples were pooled and sequenced at the Memorial Sloan Kettering Cancer Center Integrated Genomics Operation. RNA-seq libraries were filtered and trimmed using fastp[247] and mapped with STAR aligner[248] against the mm10 mouse genome assembly using default parameters. featureCounts[249] was used to calculate gene counts for input into DESeq2[250] for quality control analysis, size normalization and variance dispersion corrections.

*Statistics and reproducibility*

Prism 9 (GraphPad Software) software was used for statistical analyses except for DepMap data. Error bars, *P* values and statistical tests are reported in the figure legends. Statistical analyses on DepMap data were performed with Python v3.8. Experiments were performed in biological triplicate or as noted in the figure legends at least two, often many more, times.

## 3.5 Acknowledgments

We thank Dr. Austin Smith (University of Exeter) for the gift of the *Rex1::GFPd2* cells.

## 3.6 Figures

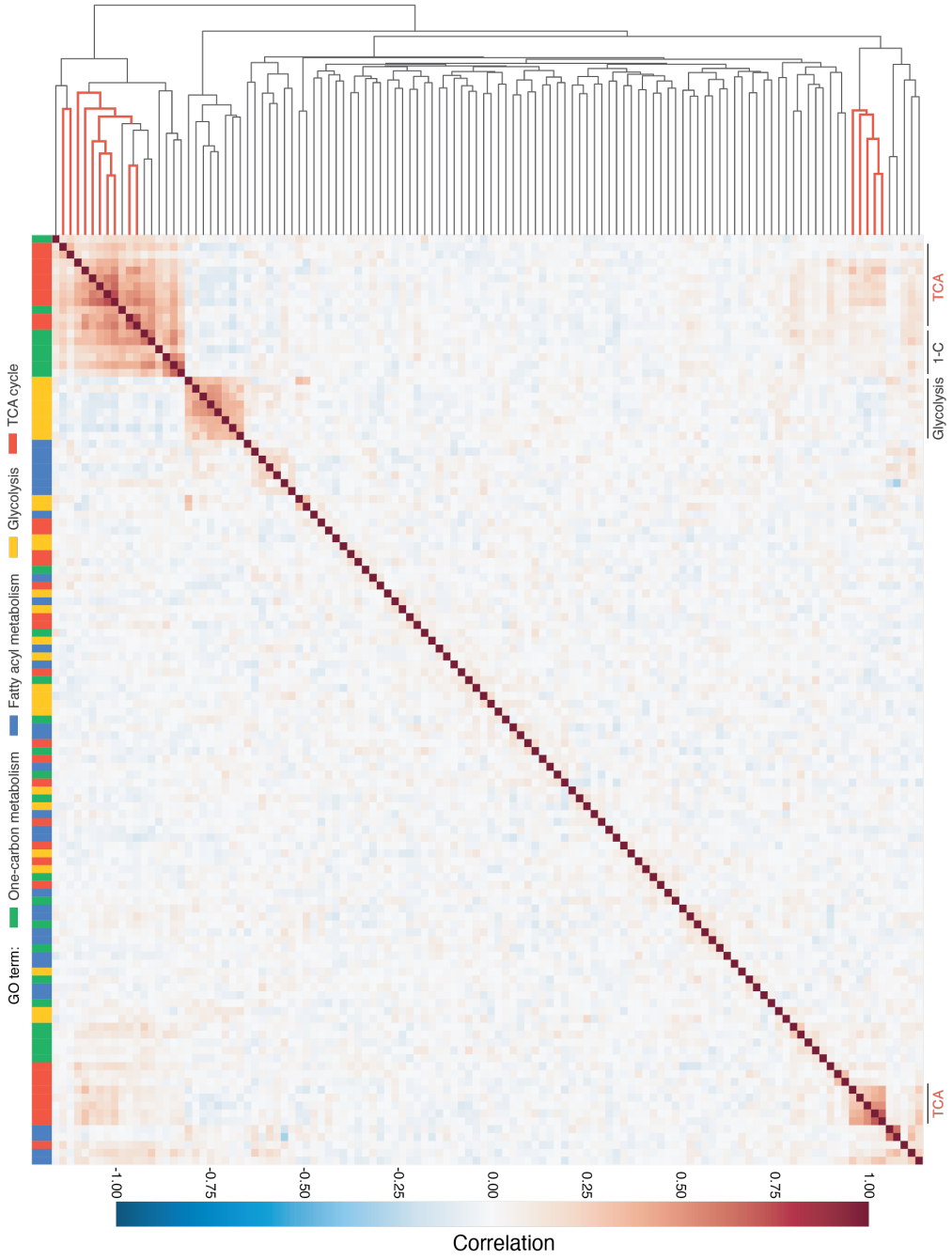


**Figure 3.1 Metabolic gene essentiality correlations across cancer cell lines.**
Heatmap depicting hierarchical clustering of pairwise gene essentiality score correlations of core metabolic pathway genes derived from four GO terms: tricarboxylic acid (TCA) cycle, canonical glycolysis, one-carbon metabolic process and fatty-acyl-CoA metabolic process. Genes are color coded to the left of the heatmap according to the GO term. TCA cycle genes are highlighted (red) in the dendrogram. This analysis was performed by Benjamin T. Jackson (from Arnold*, Jackson* et al., *Nature* 2022).

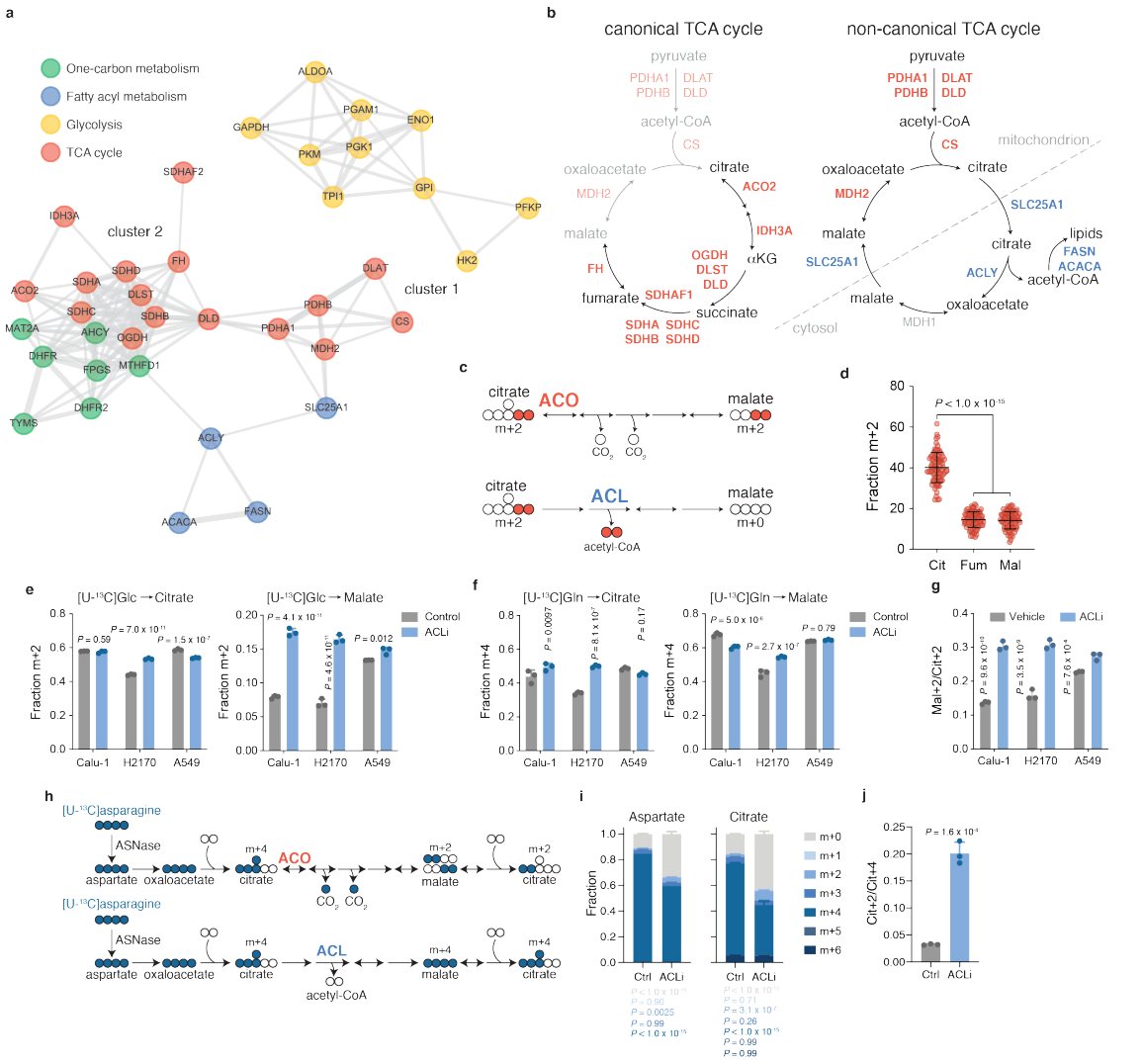


**Figure 3.2 Genetic co-essentiality mapping of metabolic enzymes reveals two TCA cycle modules.**

**a,** Two-dimensional network diagram representing gene essentiality score correlations between genes from indicated pathways (GO terms: TCA cycle, canonical glycolysis, 1-carbon metabolic process and fatty-acyl-CoA metabolic process). Correlation strength is depicted by the length and thickness of the connecting edge. **b,** Schematic representing two TCA cycle modules that emerge from gene clustering in **a**. Left, cluster 2 genes annotated on the traditional TCA cycle in bold. Right, cluster 1 genes annotated on a 'non-canonical' TCA cycle in which citrate is exported to the cytoplasm and cleaved by ACL to liberate acetyl-CoA and regenerate oxaloacetate, which can yield malate for mitochondrial import and oxaloacetate regeneration. Genes are colored according to their GO term or grey (no significant correlation). **c,** Schematic depicting possible fates for citrate containing 2 carbons derived from [U-$^{13}$C]glucose. Top, m+2 labeled citrate metabolized by aconitase in the traditional TCA cycle generates m+2 labeled malate. Bottom, m+2 labeled citrate cleaved in the cytoplasm by ACL loses two heavy-labeled carbons, producing unlabeled four-carbon derivatives. **d,** Fractional m+2 enrichment of TCA cycle intermediates in 82 non-small cell lung cancer (NSCLC) cell lines cultured with [U-$^{13}$C]glucose for 6 h. Data mined from Chen et al., 2019. **e,f,** Fractional enrichment of citrate (left) and malate (right) in three non-small cell lung cancer (NSCLC) cell lines cultured in medium containing [U-$^{13}$C]glucose (**e**) or [U-

$^{13}$C]glutamine (**f**) and treated with vehicle or 50 μM BMS-303141(ACLi) for 24 h. **g,** Fractional enrichment of glucose-derived malate m+2 relative to citrate m+2 (Mal+2/Cit+2) in NSCLC cell lines following incubation with vehicle or 50 μM BMS-303141 (ACLi) for 24 h. **h,** Schematic depicting [U-$^{13}$C]asparagine labeling of aspartate and citrate in cells expressing guinea pig asparaginase (ASNase). Asparagine-derived aspartate will generate m+4 labeled citrate. Top, m+4 labeled citrate metabolized via the canonical TCA cycle will lose two labeled carbons as $CO_2$, ultimately regenerating citrate that retains two labeled carbons (m+2). Bottom, m+4 labeled citrate metabolized by ACL will yield m+4 labeled oxaloacetate that will ultimately regenerate m+4 labeled citrate. **i,j,** Fractional labeling of aspartate (left) and citrate (right) (**i**) or citrate m+2 relative to citrate m+4 (Cit+2/Cit+4) (**j**) in ASNase-expressing 143B human osteosarcoma cells cultured in medium containing [U-$^{13}$C]asparagine and treated with vehicle or 50 μM ACLi for 24 h. Significance was assessed using unpaired, two-tailed Student's *t* test (**j**), in comparison to citrate by one-way ANOVA (**d**) or vehicle-treated cells by two-way ANOVA (**e-g,i**) with Sidak's multiple comparisons post-test. Data are mean ± SD, $n = 3$ independent replicates. Co-essentiality analysis (panel **a**) was performed by Benjamin T. Jackson. Panels **b-g** were generated by the author of this thesis and panels **i-j** were generated by Sydney P. Alibeckoff and Madeleine L. Hart (adapted from Arnold*, Jackson* et al., *Nature* 2022).

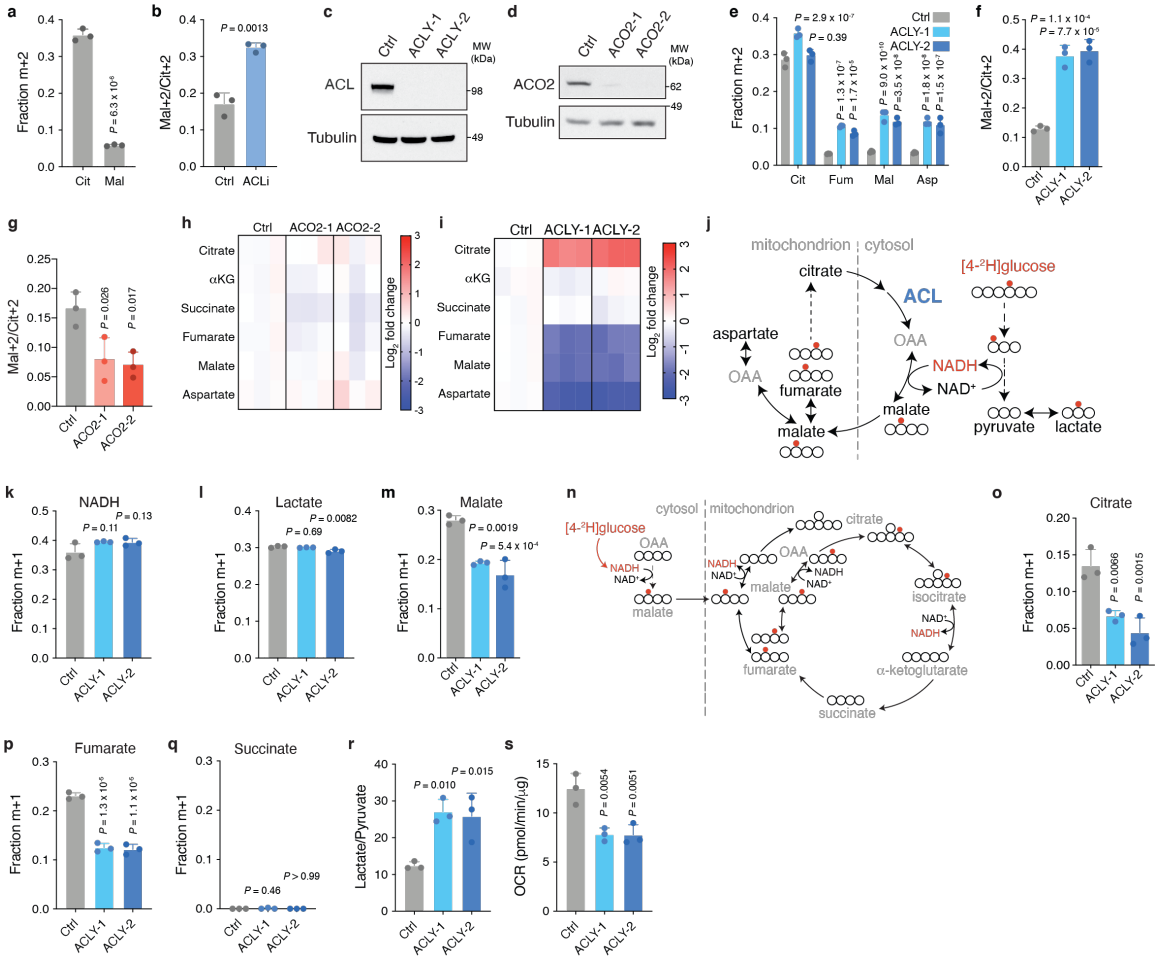


**Figure 3.3 ACL loss disrupts TCA cycle metabolism in ESCs.**

**a,** Fractional m+2 enrichment of citrate (Cit) and malate (Mal) in mouse embryonic stem cells (ESCs) cultured in medium containing [U-$^{13}$C]glucose. **b,** Fractional enrichment of malate m+2 relative to citrate m+2 (Mal+2/Cit+2) derived from [U-$^{13}$C]glucose in ESCs following treatment with vehicle or 50 µM BMS-303141 (ACLi) for 24 h. **c,d,** Immunoblot of clonal ESCs in which CRISPR/Cas9-mediated editing was used to target either a non-genic region of chromosome 8 (Ctrl) and *Acly* (ACLY-1 and ACLY-2) (**c**) or *Aco2* (ACO2-1 and ACO2-2) (**d**). **e,f,** Fractional m+2 enrichment of citrate (Cit), fumarate (Fum), malate (Mal) and aspartate (Asp) (**e**) or malate m+2 relative to citrate m+2 (Mal+2/Cit+2) (**f**) in control (Ctrl) and *Acly*-edited (ACLY-1 and ACLY-2) mouse ESCs cultured in medium containing [U-$^{13}$C]glucose. **g,h,** Assessment of the [U-$^{13}$C]glucose-derived Mal+2/Cit+2 ratio (**g**) or steady-state levels of TCA cycle metabolites represented as the fold change (expressed in $\log_2$) relative to Ctrl (**h**) in control and *Aco2*-edited ESCs. **i,** Steady-state levels of TCA cycle metabolites in *Acly*-edited mouse ESCs. Levels are represented as the fold change (expressed in $\log_2$) relative to control cells. **j,** Schematic depicting deuterium label transfer from [4-$^{2}$H]glucose first onto NADH during glycolysis and subsequently onto either malate or lactate in the cytoplasm through MDH1 or LDH activity, respectively. Following mitochondrial import, deuterium-labeled malate can be converted to fumarate. The symmetry of fumarate allows the deuterium label to be scrambled, enabling generation of deuterium-labeled citrate. **k,l,m,** Fractional m+1 enrichment of NADH (**k**), lactate (**l**), and malate

(**m**) in control and *Acly*-edited ESCs cultured in medium containing [4-$^{2}$H]glucose. **n,** Schematic depicting deuterium transfer from [4-$^{2}$H]glucose first onto malate in the cytoplasm then onto TCA cycle metabolites in the mitochondria. **o,p,q,** Fractional m+1 enrichment of citrate (**o**), fumarate (**p**) or succinate (**q**) in control and *Acly*-edited ESCs cultured in medium containing [4-$^{2}$H]glucose. **r,** Quantification of the lactate over pyruvate ratio in control and *Acly*-edited ESCs. **s,** The baseline oxygen consumption rate (OCR) in control and *Acly*-edited ESCs normalized to protein content. Twelve technical replicates were averaged for each of three independent experiments. Significance was assessed using unpaired two-tailed Student's t-test (**a, b**) or in comparison to control cells by one-way ANOVA with Sidak's multiple comparisons post-test for all other panels. Data are mean ± SD, n = 3 independent replicates. Panels **a-s** were generated by the author of this thesis with assistance from Madeleine L. Hart for panels **k-l** (adapted from Arnold*, Jackson* et al., *Nature* 2022).

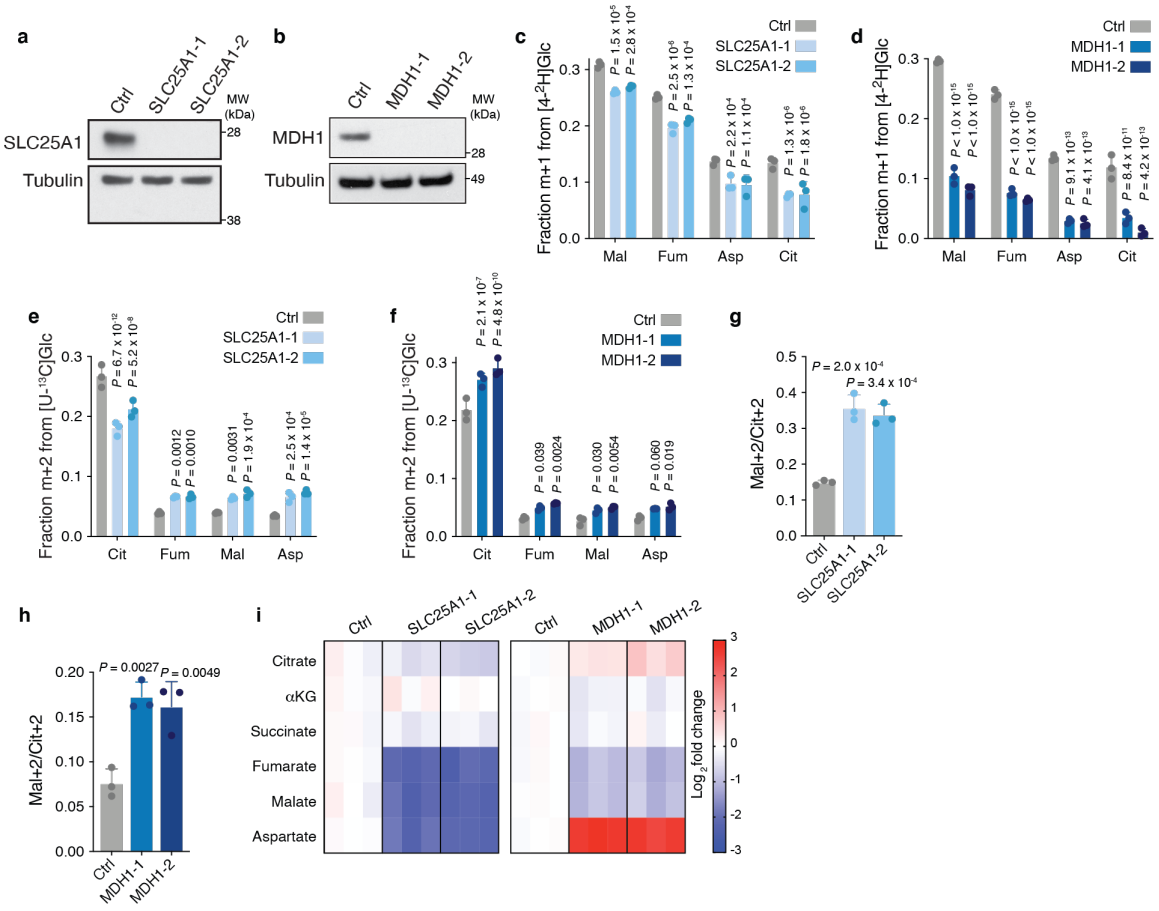


**Figure 3.4 SLC25A1 and MDH1 contribute to TCA cycle metabolism in ESCs.**
**a,b,** Immunoblot of clonal mouse embryonic stem cells (ESCs) in which CRISPR/Cas9-mediated editing was used to target either a non-genic region of chromosome 8 (Ctrl) and *Slc25a1* (SLC25A1-1 and SLC25A1-2) (**a**) or *Mdh1* (MDH1-1 and MDH1-2) (**b**). **c,d,** Fractional m+1 enrichment of malate (Mal), fumarate (Fum), aspartate (Asp) and citrate (Cit) in control (Ctrl) and *Slc25a1*-edited ESCs (**c**) or *Mdh1*-edited ESCs (**d**) cultured in medium containing [4-$^{2}$H]glucose. **e, f,** Fractional m+2 enrichment of citrate, fumarate, malate and aspartate derived from [U-$^{13}$C]glucose in control and *Slc25a1*-edited (**e**) or *Mdh1*-edited (**f**) ESCs. **g,h,** Mal+2/Cit+2 derived from [U-$^{13}$C]glucose in control and *Slc25a1*-edited (**g**) or *Mdh1*-edited (**h**) ESCs**. i,** Steady-state levels of TCA cycle metabolites in *Slc25a1*-edited (left) or *Mdh1*-edited ESCs (right). Levels are represented as the fold change (expressed in $\log_2$) relative to chromosome 8-targeted control cells. Significance was assessed in comparison to control cells by two-way ANOVA (**c-f**) or one-way ANOVA (**g,h**) with Sidak's multiple comparisons post-test. Data are mean ± SD, n = 3 independent replicates. Panels **a-i** were generated by the author of this thesis (adapted from Arnold*, Jackson* et al., *Nature* 2022).

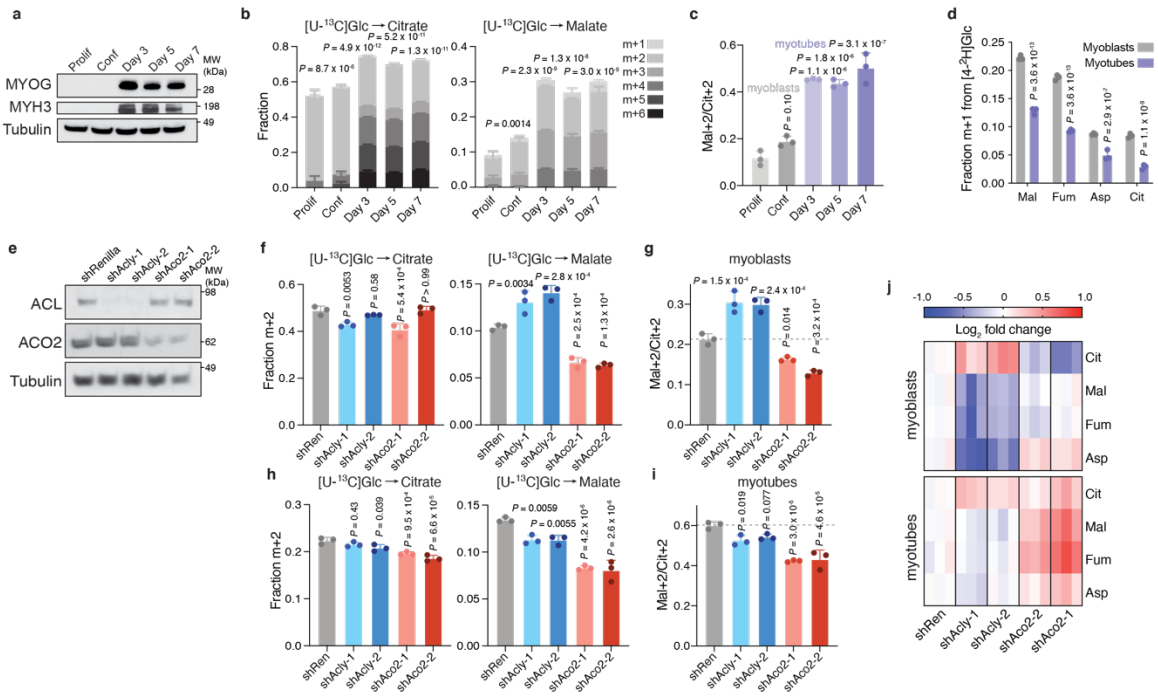

**Figure 3.5 Engagement of the non-canonical TCA cycle is cell-state dependent.**
**a,** Immunoblot comparing expression of myogenesis markers MYOG and MYH3 between proliferating (Prolif) and 100% confluent (Conf) myoblasts and myotubes differentiated for 3, 5 or 7 days. **b,** Fractional labeling of citrate (left) and malate (right) in proliferating and confluent myoblasts and myotubes differentiated for 3, 5 or 7 days cultured in medium containing [U-$^{13}$C]glucose. **c,** Fractional enrichment of malate m+2 relative to citrate m+2 (Mal+2/Cit+2) derived from [U-$^{13}$C]glucose in proliferating and confluent myoblasts and myotubes differentiated for 3, 5 or 7 days. **d,** Fractional m+1 enrichment from [4-$^{2}$H]glucose of malate (Mal), fumarate (Fum), aspartate (Asp) and citrate (Cit) in myoblasts and myotubes differentiated for 5 days. **e,** Immunoblot comparing expression of ACL and ACO2 in C2C12 cells expressing doxycycline-inducible shRNAs targeting *Acly* (shAcly-1 and shAcly-2), *Aco2* (shAco2-1 and shAco2-2) or *Renilla* luciferase (shRen, used as a control). Cells were cultured on doxycycline for two days to induce shRNA expression. **f-i,** Fractional m+2 enrichment of citrate (left) and malate (right) or malate m+2 relative to citrate m+2 (Mal+2/Cit+2) in myoblasts (**f,g**) or myotubes (**h,i**) expressing doxycycline-inducible shRNAs targeting *Acly, Aco2* or *Renilla* luciferase cultured in medium containing [U-$^{13}$C]glucose. Myoblasts and myotubes were cultured on doxycycline for two or four days, respectively, to induce shRNA expression. **j,** Measurement of steady-state levels of Cit, Fum, Mal and Asp, expressed as the $\log_2$ fold change relative to shRenilla, in myoblasts (top) and myotubes (bottom). Myoblasts and myotubes expressing doxycycline-inducible shRNAs targeting *Acly, Aco2* or *Renilla* luciferase were cultured on doxycycline for two or four days, respectively, to induce shRNA expression. In **b,** significance was assessed using one-way ANOVA with Sidak's multiple comparisons post-test to compare total metabolite fraction labeled relative to proliferating myoblasts. In remaining panels, significance was assessed in comparison to proliferating myoblasts (**c,d**) or shRen-expressing myoblasts (**f-i**) by one-way ANOVA (**c,f-i**) or two-way ANOVA (**d**) with Sidak's multiple comparisons post-test. Data are mean ± SD, n = 3 independent replicates. Panels **a-j** were generated by the author of this thesis (adapted from Arnold*, Jackson* et al., *Nature* 2022).

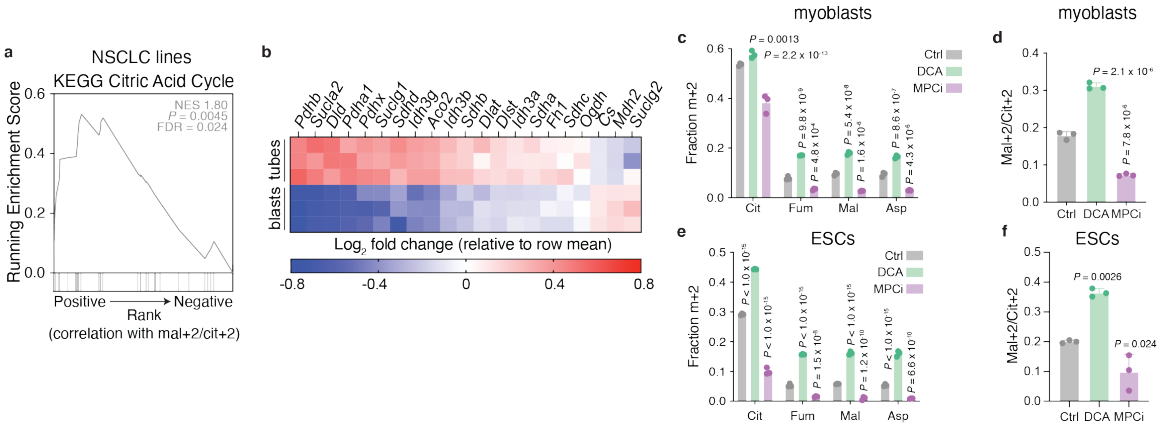


**Figure 3.6 Modulation of pyruvate oxidation alters TCA cycle choice.**
**a,** Gene set enrichment analysis showing that genes positively correlated with fractional enrichment of malate m+2 relative to citrate m+2 (Mal+2/Cit+2) derived from [U-$^{13}$C]glucose in 68 non-small cell lung cancer (NSCLC) are enriched for KEGG citric acid (TCA) cycle-associated genes. **b,** RNA-seq of TCA cycle-associated genes in myoblasts and myotubes differentiated for 5 days. Levels are represented as the $\log_2$ fold change relative to the row mean. $n = 3$ independently derived samples. **c,d,** Fractional m+2 enrichment of citrate (Cit), fumarate (Fum), malate (Mal) and aspartate (Asp) (**c**) or Mal+2/Cit+2 (**d**) derived from [U-$^{13}$C]glucose in myoblasts following treatment with vehicle, 5 mM dichloroacetate (DCA) or 10 μM UK-5099 (MPCi) for 24 h. **e,f,** Fractional m+2 enrichment of Cit, Fum, Mal and Asp (**e**) or Mal+2/Cit+2 (**f**) derived from [U-$^{13}$C]glucose in mouse embryonic stem cells (ESCs) following treatment with vehicle, 5 mM DCA or 10 μM MPCi for 24 h. In **c-f**, significance was assessed in comparison to vehicle treatment by two-way ANOVA (**c,e**) or one-way ANOVA **(d,f)** with Sidak's multiple comparisons post-test. Data are mean ± SD, $n = 3$ independent samples. Panels **a-f** were generated by the author of this thesis; RNA-seq analysis (panel **b**) was performed by Katrina I. Paras (adapted from Arnold*, Jackson* et al., *Nature* 2022).

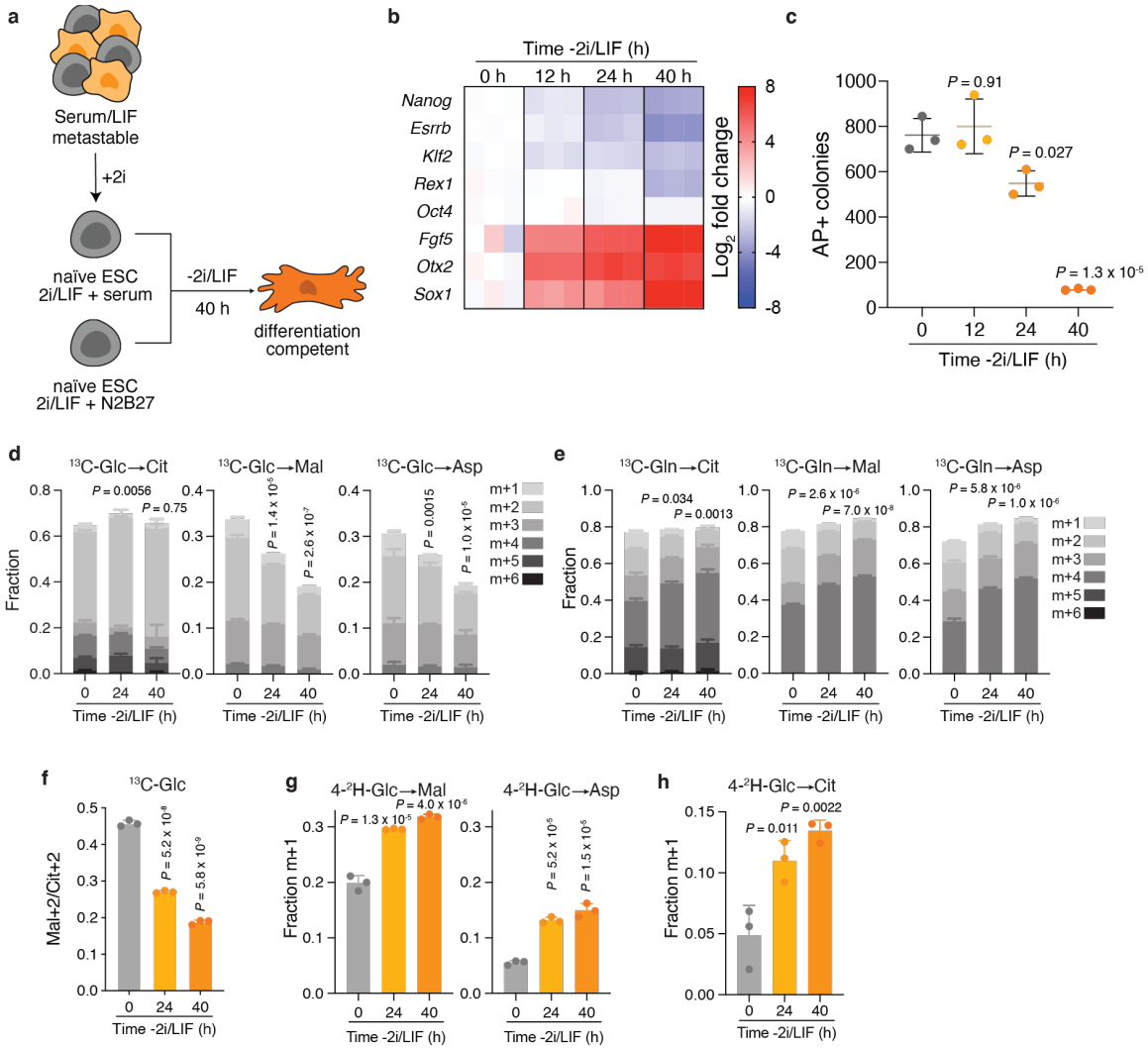


**Figure 3.7 Exit from pluripotency is accompanied by increased non-canonical TCA cycle engagement.**

**a,** Experimental setup for cell fate transitions. Mouse embryonic stem cells (ESCs) cultured in serum and leukemia inhibitory factor (LIF) are a heterogenous population that can be converted to the naïve, ground state of pluripotency by addition of MEK and GSK3β inhibitors (2i). Transition to serum-free medium lacking 2i/LIF (-2i/LIF) induces exit from the naïve pluripotent state, enabling ESCs to gain differentiation competence. **b,** qRT-PCR of pluripotency-associated (Nanog, Esrrb, Klf2, Rex1 and Oct4) and early differentiation-associated (Fgf5, Otx2 and Sox1) genes in 2i/LIF-cultured ESCs subjected to 2i/LIF withdrawal for 12, 24 or 40 h. Levels are represented as the fold change (expressed in $\log_2$) relative to naïve, 2i/LIF-cultured ESCs (0 h). **c,** Quantification of alkaline phosphatase (AP)-positive colonies representing ESCs that failed to exit from the pluripotent state. 2i/LIF-cultured ESCs were subjected to 2i/LIF withdrawal for 0, 12, 24 or 40 h and then reseeded at clonal density into medium containing 2i and LIF. **d,e,** Fractional labeling of citrate (Cit), malate (Mal) and aspartate (Asp) in serum/LIF+2i-cultured ESCs incubated with [U-$^{13}$C]glucose (**d**) or [U-$^{13}$C]glutamine (**e**) subjected to exit from pluripotency for the indicated times. **f,** Fractional enrichment of glucose-derived malate m+2 relative to citrate m+2 (Mal+2/Cit+2) in ESCs subjected to 2i/LIF withdrawal for the indicated times. **g,h,** Fractional m+1 enrichment of malate (**g**, left), aspartate (**g**, right), or citrate (**h**) derived from [4-$^{2}$H]glucose in ESCs subjected to 2i/LIF withdrawal for the indicated times. In **d-**

**e**, significance was assessed using one-way ANOVA with Sidak's multiple comparisons post-test to compare total metabolite fraction labeled relative to the 0 h timepoint. In remaining panels, significance was assessed relative to the 0 h timepoint using one-way ANOVA with Sidak's multiple comparisons post-test. Data are mean ± SD, $n = 3$ independent replicates. Panels **a-h** were generated by Benjamin T. Jackson with assistance from the author of this thesis (adapted from Arnold*, Jackson* et al., *Nature* 2022).

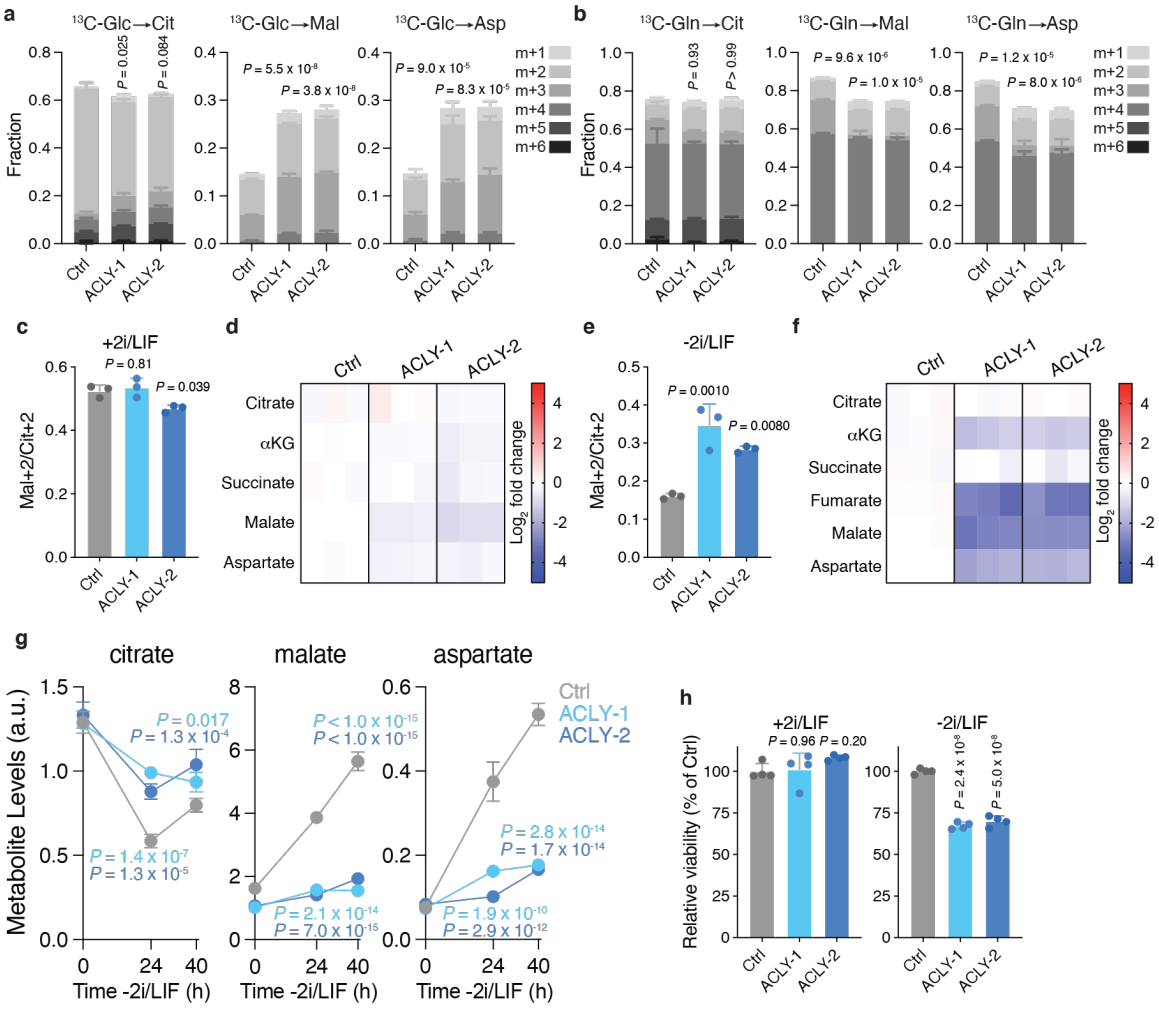


**Figure 3.8 ACL is required for metabolic rewiring during exit from pluripotency.** **a,b,** Fractional labeling of citrate (Cit), malate (Mal) and aspartate (Asp) in control and *Acly*-edited ESCs cultured in medium containing [U-$^{13}$C]glucose (**a**) or [U-$^{13}$C]glutamine (**b**) following 40 h of 2i/LIF withdrawal. **c,d,** Fractional enrichment of malate m+2 relative to citrate m+2 (Mal+2/Cit+2) derived from [U-$^{13}$C]glucose (**c**) or steady-state levels of TCA cycle metabolites (**d**) in naïve, 2i-adapted control (Ctrl) and *Acly*-edited (ACLY-1 and ACLY-2) ESCs. Steady-state levels are represented as the fold change (expressed in log2) relative to control cells. **e,f,** Assessment of the [U-$^{13}$C]glucose-derived Mal+2/Cit+2 ratio (**e**) and steady-state levels of TCA cycle metabolites (**f**) in control and *Acly*-edited ESCs subjected to 2i/LIF withdrawal for 40 h. **g,** Steady-state levels of metabolites in control and *Acly*-edited ESCs grown -2i/LIF for the indicated times. **h,** Relative viability (measured by PI exclusion) of control and *Acly*-edited ESCs maintained in the naïve pluripotent state (+2i/LIF, left) or subjected to 2i/LIF withdrawal for 40 h (-2i/LIF, right). In **a-b,** significance was assessed using one-way ANOVA with Sidak's multiple comparisons post-test to compare total metabolite fraction labeled relative to control cells. In remaining panels, significance was assessed by two-way ANOVA with Sidak's multiple comparisons post-test relative to control cells at each timepoint with stars colored according to comparison (**g**), or by one-way ANOVA in comparison to control cells (**c,e,h**) with Sidak's multiple comparisons post-test. Data are mean ± SD, $n = 4$ (**h**) or $n = 3$ (all other experiments) independent replicates. Panels **a-h** were generated by Benjamin T. Jackson with assistance from the author of this thesis (adapted from Arnold*, Jackson* et al., *Nature* 2022).

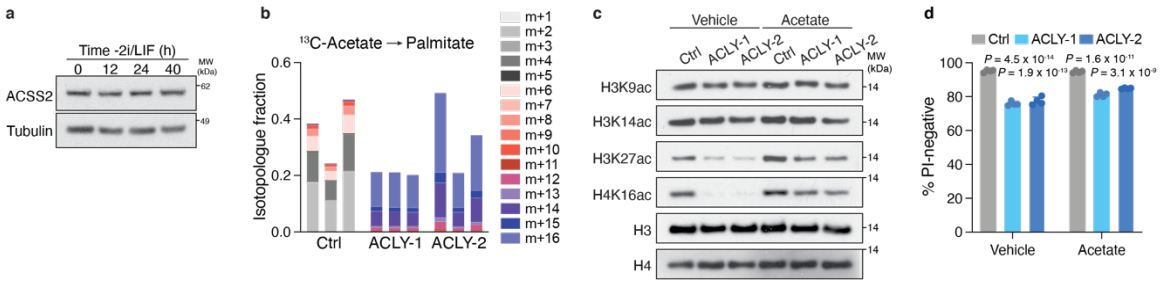


**Figure 3.9 Acetate does not reverse the effects of ACL loss on exit from pluripotency.** **a,** Immunoblot showing expression of ACSS2, the enzyme that converts acetate to acetyl-CoA in the cytosol, in naïve, ground state ESCs subjected to 2i/LIF withdrawal for the indicated times. **b,** Fractional labeling of palmitate in control and *Acly*-edited ESCs cultured in medium containing [U-$^{13}$C]acetate following 40 h of 2i/LIF withdrawal. Each bar represents one independent sample. **c,** Immunoblot comparing levels of acetylation (ac) at indicated histone lysine residues in control and *Acly*-edited ESCs subjected to 2i/LIF withdrawal for 40 h in the presence of vehicle or 5 mM sodium acetate. **d,** Relative viability of control and *Acly*-edited ESCs subjected to 2i/LIF withdrawal for 40 h in the presence of vehicle or 5 mM sodium acetate. Significance was assessed by two-way ANOVA relative to control cells with Sidak's multiple comparisons post-test. Data are mean ± SD, $n = 4$ (**d**) independent replicates. Panels **a-d** were generated by Benjamin T. Jackson and the author of this thesis with assistance from Oliver J. Newsom for panel **b** (adapted from Arnold*, Jackson* et al., *Nature* 2022).

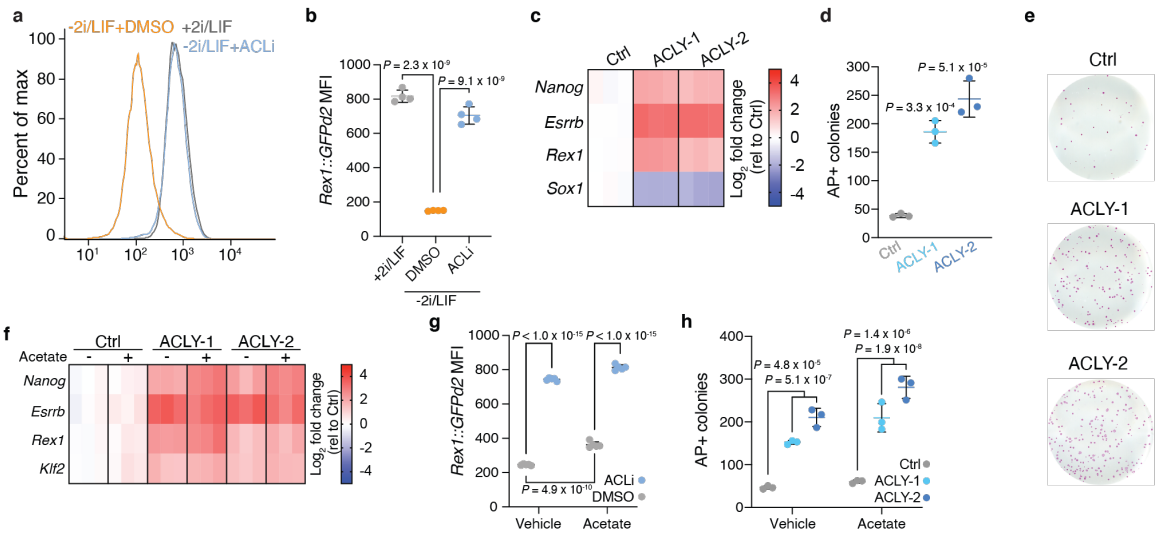


**Figure 3.10 Exit from pluripotency requires ACL.**
**a,** Representative histogram of GFP intensity encoded by the Rex1::GFPd2 reporter in ESCs subjected to 2i/LIF withdrawal for 40 h in the presence of vehicle or 50 μM BMS-303141 (ACLi). Naïve ESCs (+2i/LIF) are included as a control. **b,** Quantification of GFP mean fluorescence intensity (MFI) encoded by the Rex1::GFPd2 reporter in ESCs subjected to 2i/LIF withdrawal for 40 h in the presence of vehicle or 50 μM BMS-303141 (ACLi). Naïve ESCs (+2i/LIF) are included as a control. Representative histograms are shown in **a. c,** qRT-PCR of pluripotency-associated (Nanog, Esrrb and Rex1) and early differentiation-associated (Sox1) genes in control and *Acly*-edited ESCs subjected to 2i/LIF withdrawal for 40 h. Levels are represented as the fold change (expressed in $\log_2$) relative to chromosome 8-targeted control cells. **d,** Quantification of alkaline phosphatase positive (AP+) colonies representing control and *Acly*-edited ESCs that failed to exit the naïve pluripotent state. 2i-adapted ESCs subjected to 2i/LIF withdrawal for 40 h were reseeded at clonal density into medium containing 2i/LIF. **e,** Representative AP-stained wells from the quantification shown in **d.** AP-positive colonies represent control and *Acly*-edited ESCs that failed to exit the naïve pluripotent state. **f,** qRT-PCR of pluripotency-associated genes in control and *Acly*-edited ESCs subjected to 2i/LIF withdrawal for 40 h in the presence of vehicle or 5 mM sodium acetate. **g,** Quantification of GFP MFI encoded by the Rex1::GFPd2 reporter in ESCs subjected to 2i/LIF withdrawal for 40 h in the presence of DMSO or 50 μM BMS-303141(ACLi) and vehicle or 5 mM sodium acetate. **h,** Quantification of AP-positive colonies representing control and *Acly*-edited ESCs that failed to exit from the pluripotent state. ESCs were subjected to 2i/LIF withdrawal for 40 h in the presence of vehicle or 5 mM sodium acetate prior to reseeding at clonal density into medium containing 2i and LIF. One histogram representative of 3 replicates with similar results shown in **a**. Significance was assessed by two-way ANOVA with Sidak's multiple comparisons post-test relative to control cells (**h**) or DMSO treatment (**g**), or by one-way ANOVA with Sidak's multiple comparisons post-test (**d**) or in the indicated comparisons with Tukey's multiple comparisons post-test (**b**). All other panels depict data as mean ± SD, $n = 4$ (**b,g**) or $n = 3$ (**d,h**) independent replicates. Panels **a-h** were generated by Benjamin T. Jackson with assistance from the author of this thesis (adapted from Arnold*, Jackson* et al., *Nature* 2022).

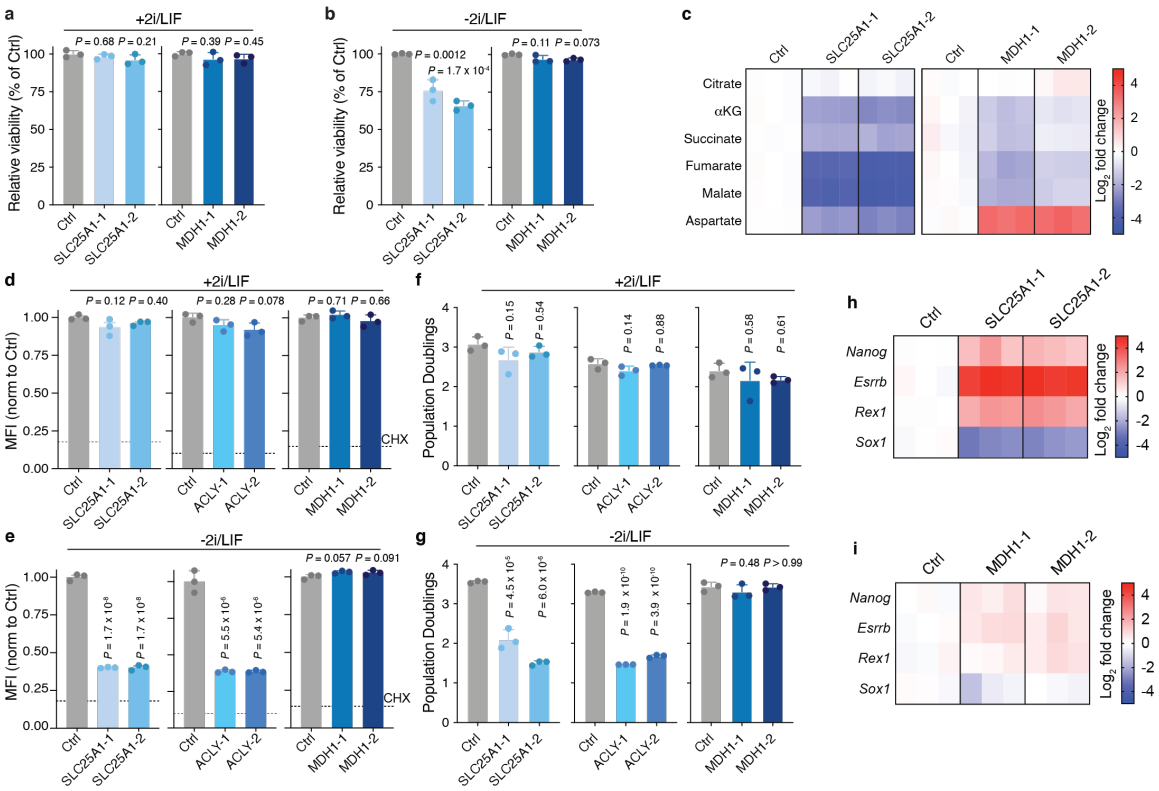


**Figure 3.11 Effect of SLC25A1 and MDH1 loss in exit from naïve pluripotency.**
**a,b,** Relative viability (measured by PI exclusion) of control and *Slc25a1*-edited (left) and *Mdh1*-edited (right) ESCs maintained in the naïve pluripotent state (+2i/LIF, **a**) or subjected to 2i/LIF withdrawal for 40 h (-2i/LIF, **b**). **c,** Steady-state levels of TCA cycle metabolites in control and *Slc25a1*-edited (left) and *Mdh1*-edited (right) ESCs subjected to 2i/LIF withdrawal for 40 h. Steady-state levels are represented as the fold change (expressed in $\log_2$) relative to control cells. **d, e,** Relative O-propargyl-puromycin (OP-puro) mean fluorescence intensity (MFI) in control, *Slc25a1*-edited, *Acly*-edited and *Mdh1*-edited ESCs that have been maintained in the naïve pluripotent state (**d**) or subjected to 2i/LIF withdrawal for 40 h (**e**). Dotted line represents OP-puro MFI following cycloheximide (CHX) treatment as a control. **f,g,** Population doublings of control, *Slc25a1*-edited, *Acly*-edited and *Mdh1*-edited ESCs that have been maintained in the naïve pluripotent state (**f**) or subjected to 2i/LIF withdrawal for 40 h (**g**). **h,i,** qRT-PCR of pluripotency-associated (Nanog, Esrrb and Rex1) and early differentiation-associated (Sox1) genes in control and *Slc25a1*-edited (**h**) and *Mdh1*-edited (**i**) ESCs subjected to 2i/LIF withdrawal for 40 h. Significance was assessed in comparison to control cells by one-way ANOVA with Sidak's multiple comparisons post-test. Data are mean ± SD, $n = 3$ independent samples. Panels **a-i** were generated by Benjamin T. Jackson with assistance from the author of this thesis (adapted from Arnold*, Jackson* et al., *Nature* 2022).

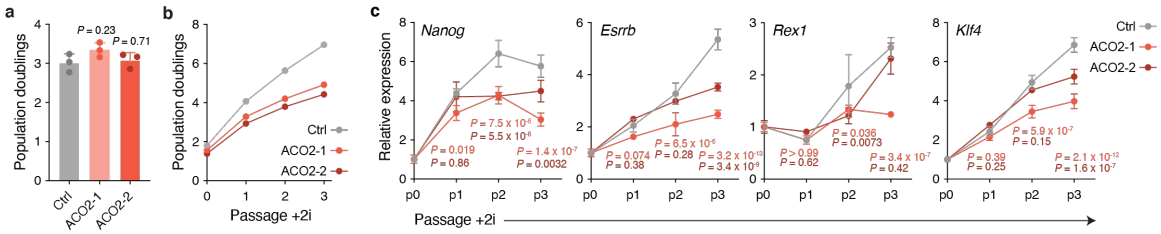


**Figure 3.12 Conversion to naïve pluripotency requires ACO2.**
**a,** Population doublings of control and *Aco2*-edited ESCs cultured in metastable (serum/LIF) conditions. **b,** Cumulative population doublings over the indicated passages of control and *Aco2*-edited ESCs upon conversion to the naïve, ground state of pluripotency via addition of MEK and GSK3β inhibitors (+2i). **c,** qRT-PCR of pluripotency-associated genes at the indicated passages in control and *Aco2*-edited ESCs following addition of 2i. Gene expression at every passage was normalized to passage 0 (p0). Data are mean ± SD, $n = 1$ (**b**) or $n = 3$ (**a**, **c**) independent replicates. Significance was assessed in comparison to control cells by one-way ANOVA with Sidak's multiple comparisons post-test (**a**) or relative to control cells at each timepoint with stars colored according to comparison by two-way ANOVA with Sidak's multiple comparisons post-test (**c**). Panels **a-c** were generated by the author of this thesis (adapted from Arnold*, Jackson* et al., *Nature* 2022).

# CHAPTER 4: CONCLUSIONS AND FUTURE DIRECTIONS

Different cell types possess distinct metabolic profiles, and it is increasingly appreciated that metabolism changes during cell fate transitions. Emerging evidence suggests that metabolic activity can be dictated by the bioenergetic requirements of specialized cell types or by differences in growth rate, local nutrient availability, or metabolic enzyme expression or activity. However, whether metabolic profiles are functionally linked with cell identity remains poorly explored. In this thesis, we sought to determine whether metabolic diversity is an intrinsic feature of cell identity and identify drivers of this diversity in mammalian cells.

## 4.1 Summary

Most proliferating cultured cells rely on glutamine oxidation to fuel the TCA cycle, but mouse ESCs cultured under conditions that drive enhanced self-renewal display a unique, glutamine-independent metabolic phenotype. Mouse ESCs maintained in a state of naïve pluripotency by the addition of inhibitors against MEK and GSK3β display altered glucose and glutamine metabolism that enables proliferation in the absence of exogenous glutamine[121]. However, whether these metabolic features are a specific consequence of the altered signal transduction mediated by the inhibitors or a more generalizable feature of pluripotent ESCs remained an open question. In **Chapter 2**, we found that glutamine independence is so intricately entwined with the pluripotent state that transient glutamine deprivation is sufficient to select for ESCs with the highest self-

renewal capacity from within a heterogeneous population. These findings indicate that glutamine independence is an intrinsic component of pluripotent cell identity and reveal that understanding metabolic profiles provides an opportunity to design strategies to select for or against specific cell types of interest. Moreover, this work reveals that TCA cycle wiring functions as a driver, not a mere consequence, of cell identity.

The existence of specialized TCA cycle behavior across distinct cell types led us to hypothesize that TCA cycle enzymes might assemble into pathway configurations beyond the one originally described by Sir Hans Krebs (**Chapter 1**). In **Chapter 3**, we combined genetic co-essentiality mapping with isotope tracing studies in cancer cells and stem cells and identified a biochemical alternative to the traditional TCA cycle that transits through the cytoplasm and is anchored by ACL. We found that TCA cycle configuration is cell-state dependent and successful pluripotent state transitions require appropriate TCA cycle engagement. Collectively, this body of work uncovers an alternative TCA cycle pathway and reveals that TCA cycle behavior is both an intrinsic feature of cell identity and critical for the establishment of cell fate.

### 4.2 The non-canonical TCA cycle as a pro-growth strategy for cells

Why would cells preferentially engage the non-canonical TCA cycle over the traditional pathway? Non-canonical TCA cycle utilization confers several potential advantages to proliferating cells. Most notably, in the non-canonical TCA cycle, valuable reduced carbon that would otherwise be lost as $CO_2$ is retained and used to produce cytosolic acetyl-CoA, a critical biosynthetic precursor (**Figure 4.1**). Cytosolic NAD+ is

necessary to sustain glycolysis and is a limiting cofactor required for several catabolic and biosynthetic reactions. With each pyruvate molecule that is taken up into the mitochondria and oxidized in the traditional TCA cycle, an opportunity to regenerate cytosolic NAD+ via the LDH reaction is lost. However, this lost redox opportunity is remedied by the non-canonical TCA cycle, which regenerates NAD+ in the cytosol via the MDH1-mediated reduction of OAA to malate (**Figure 4.1**). Finally, recent work suggests that overproduction of mitochondrial NADH can constrain cell proliferation if it is not balanced with ATP demand and consumption[74]. By circumventing multiple

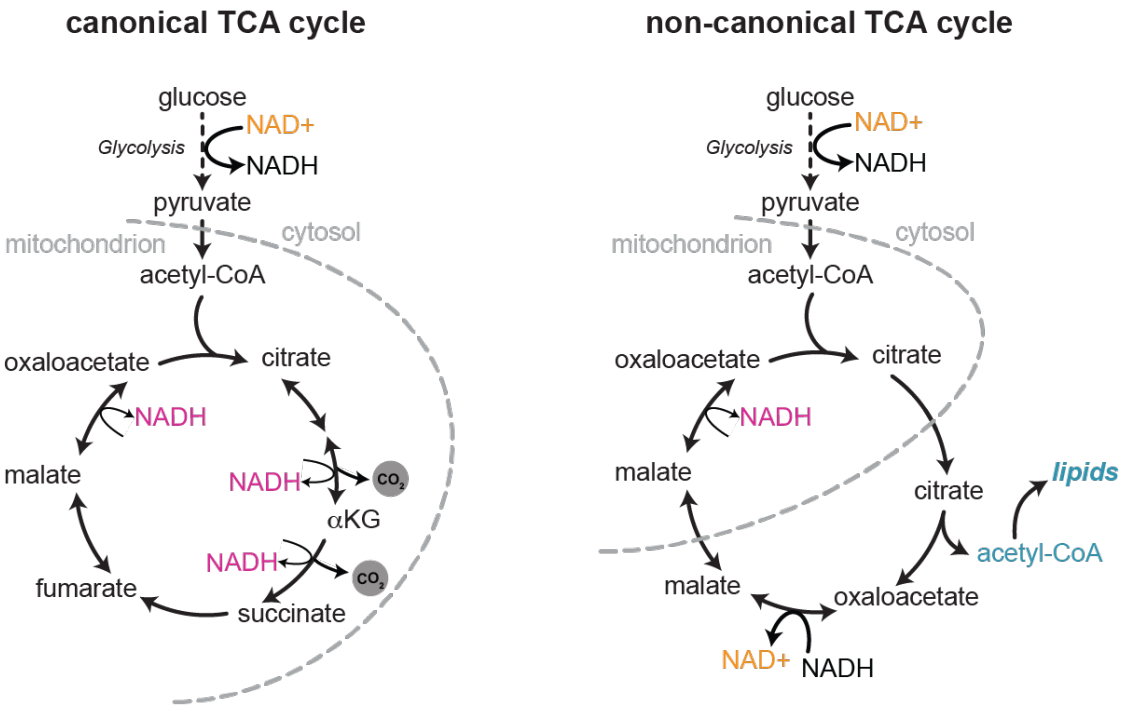


**Figure 4.1 Pro-growth advantages of the non-canonical TCA cycle.**
The canonical TCA cycle combusts carbon substrates, resulting in the loss of two carbon atoms to carbon dioxide ($CO_2$) with each turn of the cycle. In the non-canonical TCA cycle, these carbons are retained and used to generate acetyl-CoA, a biosynthetic precursor used for de novo lipid synthesis. The non-canonical TCA cycle, but not the canonical pathway, balances the consumption of cytosolic NAD+ during glycolysis with NAD+ regeneration via the reduction of oxaloacetate to malate. The non-canonical TCA cycle also bypasses two of the NADH-producing steps of the canonical TCA cycle.

NADH-producing steps of the traditional TCA cycle, engagement of the non-canonical pathway may relieve cells of this pressure while still maintaining oxaloacetate regeneration. This pathway thus represents a metabolic strategy that can be preferentially engaged by cells depending on their unique bioenergetic requirements.

### 4.3 Drivers of TCA cycle choice

While the intra- or extracellular drivers of TCA cycle choice remain to be fully elucidated, in **Chapter 3** we found that the degree to which cells engage the non-canonical TCA cycle can be toggled by modulating the amount of pyruvate captured for oxidation by the PDHC. Blocking import of pyruvate into the mitochondria via MPC inhibition led both ESCs and myoblasts to primarily engage in non-canonical TCA cycle metabolism. Reciprocally, activation of the PDHC via treatment with a PDK inhibitor resulted in more canonical TCA cycle engagement. The implication of these results is that smaller mitochondrial pools of pyruvate and, thus, citrate are preferentially metabolized by the non-canonical TCA cycle. Only when these metabolites accumulate to sufficient levels do carbons begin to flow through the traditional TCA cycle. As described above, some of the carbon molecules that flow through the traditional TCA cycle are lost as $CO_2$. These findings raise the intriguing possibility that cells only combust substrates in the traditional TCA cycle when their nutrient pools are substantial enough to withstand loss of carbon to $CO_2$.

This work also suggests that contrary to the traditional view of the field, export of citrate to the cytosol through SLC25A1 is a major route of citrate metabolism in most

cultured cells, raising the possibility that flux through ACO2 mainly functions as excess or 'overflow' metabolism. In support of this hypothesis, the affinity of ACO2 for citrate is approximately 0.3 mM[251], while the affinity of SLC25A1 for citrate is 40 times higher at approximately 7.5 uM[252,253]. Moreover, ACO2 contains an iron-sulfur cluster, making it exquisitely sensitive to oxygen and susceptible to damage from mitochondrial ROS. These features suggest that ACO2 activity is prone to repression under physiological conditions, which could support preferential engagement of the non-canonical TCA cycle. Future work should aim to shed light on these hypotheses and the different mechanisms and contexts that dictate TCA cycle choice.

### 4.4 The non-canonical TCA cycle underlies metabolic diversity

We identified the non-canonical TCA cycle as a major metabolic network in cultured cells in part due to the $^{13}$C-glucose isotope labeling pattern that it produces. Published isotope tracing data from cultured cell lines frequently demonstrates significant loss of glucose-derived label in TCA cycle metabolites downstream of citrate[222]. Some of these papers attributed this disconnect in labeling to a reduction in glucose or pyruvate oxidation in the TCA cycle, but this explanation is not consistent with the label loss occurring downstream of citrate. In **Chapter 3**, we demonstrated that label loss between citrate and downstream TCA cycle metabolites is in part ACL-dependent in cancer cells and stem cells. These findings support a role for the non-canonical TCA cycle in altering citrate metabolism and suggest that engagement of this pathway contributes to the heterogeneous labeling patterns exhibited by cultured cell lines.

Conceptually, the non-canonical TCA cycle continuously recycles OAA via the mitochondrial reimport of malate, making it net-neutral with regard to the cataplerosis and anaplerosis of OAA-derived carbons[254]. However, ESCs deficient for ACL or SLC25A1 display significantly smaller pools of aspartate, which is synthesized from OAA. Aspartate is utilized in both nucleotide and protein biosynthesis and production of this metabolite has been shown to be limiting for cell proliferation[33,34]. Thus, aspartate deficiency likely contributes to the impaired protein synthesis and reduced proliferation exhibited by ACL- and SLC25A1-deficient cells upon exit from pluripotency. Taken together, these findings suggest that the non-canonical TCA cycle supports the maintenance of intracellular aspartate pools and indicate that the pathway plays a metabolic role beyond strictly recycling carbons.

As discussed in **Chapter 1**, reducing equivalents generated by the TCA cycle donate their electrons to the ETC to support OXPHOS. The TCA cycle also directly interfaces with the ETC via SDH, which is a TCA cycle enzyme with dual functions in complex II. Thus, it stands to reason that reduced engagement of the traditional TCA cycle has the capacity to affect ETC activity and respiration. Indeed, we found that ESCs deficient for ACL exhibit a lower oxygen consumption rate than their wild-type counterparts, which is indicative of reduced respiration. The blunted respiration exhibited by ACL-deficient cells could be driven by multiple mechanisms, including impaired transfer of reducing equivalents back into the mitochondria, bypassing of the NADH-producing steps of the traditional cycle, or reduced flux through SDH. Further studies are needed to elucidate the link between TCA cycle choice and ETC activity, but our results suggest that changes in TCA cycle configuration may allow cells to toggle ETC activity

depending on their specific bioenergetic requirements. For example, while the ETC is efficient at producing energy in the form ATP, recent work has shown that ATP is not limiting for cell proliferation[74]. Thus, it is possible that TCA cycle configuration can be adjusted depending on cellular requirements for ATP versus other outputs of either the traditional or non-canonical TCA cycle.

Collectively, our findings reveal that utilization of the non-canonical TCA cycle affects multiple metabolic features. Given this, we speculate that TCA cycle configuration is a major driver of the significant metabolic diversity exhibited by mammalian cells. An interesting avenue of further investigation will be to determine whether TCA cycle configuration regulates TCA cycle substrate preference, a major source of metabolic variability between cells and a potential vulnerability that could be exploited in anticancer therapies.

## 4.5 Future directions

### *4.5.1 TCA cycle activity during early development*

In **Chapter 3**, we uncovered a requirement for appropriate TCA cycle engagement in permitting pluripotent cell state transitions. Glucose tracing demonstrated that ESCs in the naïve, ground state of pluripotency engage the canonical TCA cycle and exit from this cell state occurs alongside a shift towards non-canonical TCA cycle metabolism. Accordingly, ESCs deficient for the non-canonical TCA cycle enzymes ACL or SLC25A1 display significant metabolic disruption specifically during the

acquisition of differentiation competence, rendering them unable to meet the metabolic demands of this process and blocking them from exiting pluripotency.

These findings establish a metabolic switch required for exit from the naïve pluripotent state *in vitro*, but whether a role for the non-canonical TCA cycle exists during embryonic development *in vivo* remains to be elucidated. Intriguingly, homozygous *Acly* knockout mice are embryonic lethal, dying before 8.5 days post coitum[255]. Mutations in human *Slc25a1* are associated with combined D-2- and L-2-hydroxyglutaric aciduria, an inborn error of metabolism characterized by elevated levels of both L- and D-2HG in the body. This rare disorder presents with neonatal symptoms, developmental delays, and early death[256]. It is tempting to speculate that these developmental defects point to a role for the non-canonical TCA cycle in supporting embryonic development *in vivo*. However, testing of this hypothesis will be challenging as it requires uncoupling the role that these enzymes play in the non-canonical TCA cycle from their other significant metabolic functions. The easier approach would likely be to perform $^{13}$C-glucose isotope tracing *in vivo* or in isolated embryos cultured *in vitro* and use the glucose-derived malate m+2/citrate m+2 ratio that we take advantage of in **Chapter 3** to chart TCA cycle metabolism at different developmental stages. Recent work used $^{13}$C-glucose isotope tracing to track the metabolism of the 2C, morula, and blastocyst stages of extracted preimplantation embryos cultured *in vitro*[257]. This work uncovered a marked disconnect between the two halves of the TCA cycle during early development, which may be suggestive of non-canonical TCA cycle activity[257]. As for early development *in vivo*, a recent study combined isotope tracing with metabolomics to study metabolic programs in the placenta and embryo during midgestation in mice[258].

This work revealed significant variability in TCA cycle tracing patterns between the placenta and embryo at early timepoints and across different organs (i.e. brain, heart, and liver) at later timepoints during midgestation[258]. These fascinating findings reinforce the feasibility of this approach and support the notion that TCA cycle behavior is also dynamic during early development *in vivo*.

While the exit from naïve pluripotency drives a shift from canonical to non-canonical TCA cycle metabolism, we found the opposite to be true in myogenesis, which is accompanied by a shift towards canonical TCA engagement. This observation implies that TCA cycle rewiring is not unidirectional during differentiation. Instead, the directionality of TCA cycle rewiring is likely variable depending on lineage trajectory. Future work should aim to test how TCA cycle behavior changes across divergent lineage trajectories and, accordingly, whether enforcing non-canonical versus canonical TCA cycle metabolism blocks cells at different stages of lineage specification. In line with this, it will be interesting to study the effects of ACL versus ACO2 loss on lineage-specific differentiation and determine whether loss of either enzyme biases cells to undergo differentiation into specific lineages. These studies will add to our understanding of the mechanisms by which metabolism can exert control over developmental biology.

### *4.5.2 In vitro versus in vivo TCA cycle engagement*

A major question that arises from this work is whether the non-canonical TCA cycle is engaged by cells *in vivo* and, if so, in what tissues and under what contexts. We found that multiple cultured cell types, including cancer cells and stem cells, engage in

significant non-canonical TCA cycle activity. In support of this finding, isotope tracing data from a variety of studies in cultured cell lines show significant loss of $^{13}$C-glucose-derived label in TCA cycle metabolites downstream of citrate[222]. However, in contrast to their *in vitro* counterparts, *in vivo* samples from both tumors and normal tissue typically exhibit minimal loss of glucose label between citrate and malate[90,147,148,259]. Variability in TCA cycle behavior between cells growing *in vitro* versus *in vivo* has been appreciated in the field for some time, but the basis for this inconsistency has not yet been established. Our results suggest that differential engagement of the non-canonical TCA cycle may contribute to the discrepancy between *in vitro* and *in vivo* metabolic phenotypes. In support of this hypothesis, a recent study demonstrated that pancreatic cancer cells were more reliant on *Acly* when cultured *in vitro* and were conversely more dependent upon *Aco2* when engrafted onto mice[235]. This is a particularly intriguing finding given that most metabolic gene essentialities were similar between cancer cells cultured *in vitro* versus *in vivo*[235].

Key TCA cycle substrates like glucose and glutamine are supplied at supraphysiological levels in cell culture medium to support the increased glycolysis and glutaminolysis exhibited by rapidly proliferating cells. It is possible that non-canonical TCA cycle activity is driven by this abundant nutrient availability. In support of this idea, the glucose tracing-derived malate m+2/citrate m+2 ratio in NSCLC cell lines is negatively correlated with both glucose and glutamine uptake, indicating that more

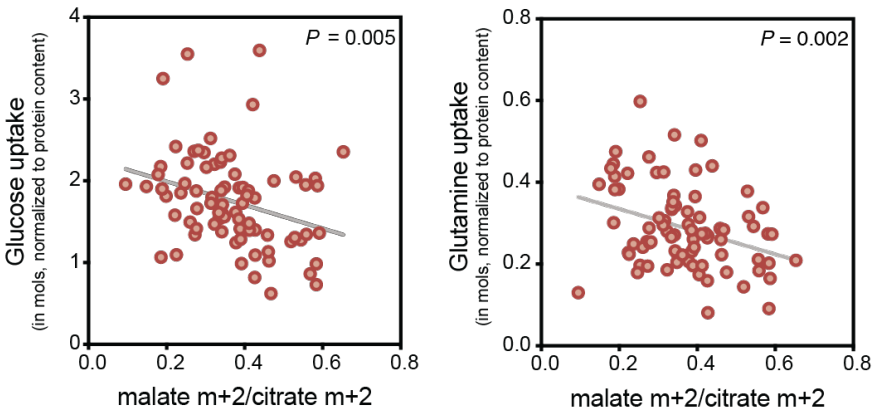


**Figure 4.2 The correlation between nutrient uptake and canonical TCA cycle engagement.** Graph of the correlation between the glucose isotope tracing-derived malate m+2 over citrate m+2 ratio versus glucose uptake (left) and glutamine uptake (right) in dozens of NSCLC cell lines. Data mined from Chen et al., 2019.

traditional TCA cycle activity is associated with reduced uptake of these substrates [222] (**Figure 4.2**). However, one important caveat is that entry of glutamine-derived carbon at the level of αKG (i.e. glutamine anaplerosis) causes glucose label dilution that decreases the malate m+2/citrate m+2 ratio[223]. Thus, the relationship between TCA cycle choice and glutamine uptake needs to be uncoupled from this effect. If culture conditions do, in fact, bias cells towards engagement of the non-canonical TCA cycle, this would have significant implications for how we interpret and develop therapeutics from metabolic studies carried out *in vitro*. Such a finding would require that we modify cell culture conditions to ensure that the metabolism we observe in cells cultured in a dish more closely reflects the metabolic networks that sustain the growth of cells *in vivo*.

Given the myriad advantages that the non-canonical TCA cycle offers to growing cells (see above), it is tempting to speculate that engagement of this pathway is associated with increased proliferative capacity. In contrast to cells growing in culture, which largely exhibit rapid proliferation, many of the cells that make up the tissues of the body

have undergone terminal differentiation and exhibit reduced anabolic cell growth. Thus, it is plausible that differences in growth rate between cells growing *in vitro* versus *in vivo* could dictate TCA cycle choice and contribute to discrepancies in metabolic phenotypes between these contexts. Future work should aim to elucidate the links between proliferation, terminal differentiation, and mode of TCA cycle metabolism. These studies will further our understanding of the metabolic strategies that support cell growth and proliferation in different contexts, which may reveal new therapeutic opportunities to target cancer and other diseases driven by aberrant metabolism.

## REFERENCES


1 Lunt, S. Y. & Vander Heiden, M. G. Aerobic glycolysis: meeting the metabolic requirements of cell proliferation. *Annu Rev Cell Dev Biol* **27**, 441-464, doi:10.1146/annurev-cellbio-092910-154237 (2011).

2 Krebs, H. A. & Johnson, W. A. The role of citric acid in intermediate metabolism in animal tissues. *FEBS Lett* **117 Suppl**, K1-10, doi:10.4159/harvard.9780674366701.c143 (1980).

3 Krebs, H. A. & Johnson, W. A. Metabolism of ketonic acids in animal tissues. *Biochem J* **31**, 645-660, doi:10.1042/bj0310645 (1937).

4 Ryan, D. G. & O'Neill, L. A. J. Krebs Cycle Reborn in Macrophage Immunometabolism. *Annu Rev Immunol* **38**, 289-313, doi:10.1146/annurev-immunol-081619-104850 (2020).

5 Inigo, M., Deja, S. & Burgess, S. C. Ins and Outs of the TCA Cycle: The Central Role of Anaplerosis. *Annu Rev Nutr* **41**, 19-47, doi:10.1146/annurev-nutr-120420-025558 (2021).

6 Pavlova, N. N., Zhu, J. & Thompson, C. B. The hallmarks of cancer metabolism: Still emerging. *Cell Metab* **34**, 355-377, doi:10.1016/j.cmet.2022.01.007 (2022).

7 Kornberg, H. L. Anapleroic sequences and their role in metabolism. *Essays Biochem.* **2**, 1-31 (1966).

8 Kornberg, H. L. Anaplerotic sequences in microbial metabolism. *Angew. Chem. Int. Ed. Engl.* **4**, 558-565 (1965).

9 Smith, E. & Morowitz, H. J. Universality in intermediary metabolism. *Proc Natl Acad Sci U S A* **101**, 13168-13173, doi:10.1073/pnas.0404922101 (2004).

10 Muchowska, K. B. *et al.* Metals promote sequences of the reverse Krebs cycle. *Nat Ecol Evol* **1**, 1716-1721, doi:10.1038/s41559-017-0311-7 (2017).

11 Muchowska, K. B., Varma, S. J. & Moran, J. Synthesis and breakdown of universal metabolic precursors promoted by iron. *Nature* **569**, 104-107, doi:10.1038/s41586-019-1151-1 (2019).

12 Keller, M. A., Kampjut, D., Harrison, S. A. & Ralser, M. Sulfate radicals enable a non-enzymatic Krebs cycle precursor. *Nat Ecol Evol* **1**, 83, doi:10.1038/s41559-017-0083 (2017).

13 Morowitz, H. J., Kostelnik, J. D., Yang, J. & Cody, G. D. The origin of intermediary metabolism. *Proc Natl Acad Sci U S A* **97**, 7704-7708, doi:10.1073/pnas.110153997 (2000).

14 Evans, M. C., Buchanan, B. B. & Arnon, D. I. A new ferredoxin-dependent carbon reduction cycle in a photosynthetic bacterium. *Proc Natl Acad Sci U S A* **55**, 928-934, doi:10.1073/pnas.55.4.928 (1966).

15 Buchanan, B. B. & Arnon, D. I. A reverse KREBS cycle in photosynthesis: consensus at last. *Photosynth Res* **24**, 47-53 (1990).

16 Zhang, X. V. & Martin, S. T. Driving parts of Krebs cycle in reverse through mineral photochemistry. *J Am Chem Soc* **128**, 16032-16033, doi:10.1021/ja066103k (2006).

17 Verschueren, K. H. G. *et al.* Structure of ATP citrate lyase and the origin of citrate synthase in the Krebs cycle. *Nature* **568**, 571-575, doi:10.1038/s41586-019-1095-5 (2019).
18 Nunoura, T. *et al.* A primordial and reversible TCA cycle in a facultatively chemolithoautotrophic thermophile. *Science* **359**, 559-563, doi:10.1126/science.aao3407 (2018).
19 Steffens, L. *et al.* High CO2 levels drive the TCA cycle backwards towards autotrophy. *Nature* **592**, 784-788, doi:10.1038/s41586-021-03456-9 (2021).
20 Mall, A. *et al.* Reversibility of citrate synthase allows autotrophic growth of a thermophilic bacterium. *Science* **359**, 563-567, doi:10.1126/science.aao2410 (2018).
21 Baldwin, J. E. & Krebs, H. The evolution of metabolic cycles. *Nature* **291**, 381-382, doi:10.1038/291381a0 (1981).
22 Intlekofer, A. M. & Finley, L. W. S. Metabolic signatures of cancer cells and stem cells. *Nat Metab* **1**, 177-188, doi:10.1038/s42255-019-0032-0 (2019).
23 Kornberg, H. Krebs and his trinity of cycles. *Nat Rev Mol Cell Biol* **1**, 225-228, doi:10.1038/35043073 (2000).
24 Annau, E., Banga, I., Gözsy, B., Huszák, B., Laki, K., Straub, B., & Szent-Györgryi, A. Über die Bedeutung der Fumarsäure für die tierische Gewebsatmung., 1068 (1935).
25 Stare, F. J. The effect of fumarate on the respiration of liver and kidney tissue. *Biochem J* **30**, 2257-2261, doi:10.1042/bj0302257 (1936).
26 Martius, C. K., F. Physiological breakdown of citric acid. *Prelim. Z Physiol Chem* **246**, 1-11 (1937).
27 Krebs, H. A. & Eggleston, L. V. The oxidation of pyruvate in pigeon breast muscle. *Biochem J* **34**, 442-459, doi:10.1042/bj0340442 (1940).
28 Novelli, G. D. a. L., F. The catalytic function of coenzyme A in citric acid synthesis. *J. Biol. Chem.* **182**, 213-228 (1950).
29 Stern, J. R., Shapiro, B. & Ochoa, S. Synthesis and breakdown of citric acid with crystalline condensing enzyme. *Nature* **166**, 403-404, doi:10.1038/166403b0 (1950).
30 Owen, O. E., Kalhan, S. C. & Hanson, R. W. The key role of anaplerosis and cataplerosis for citric acid cycle function. *J Biol Chem* **277**, 30409-30412, doi:10.1074/jbc.R200006200 (2002).
31 Hatzivassiliou, G. *et al.* ATP citrate lyase inhibition can suppress tumor cell growth. *Cancer Cell* **8**, 311-321, doi:10.1016/j.ccr.2005.09.008 (2005).
32 Zhao, S. *et al.* ATP-Citrate Lyase Controls a Glucose-to-Acetate Metabolic Switch. *Cell Rep* **17**, 1037-1052, doi:10.1016/j.celrep.2016.09.069 (2016).
33 Birsoy, K. *et al.* An Essential Role of the Mitochondrial Electron Transport Chain in Cell Proliferation Is to Enable Aspartate Synthesis. *Cell* **162**, 540-551, doi:10.1016/j.cell.2015.07.016 (2015).
34 Sullivan, L. B. *et al.* Supporting Aspartate Biosynthesis Is an Essential Function of Respiration in Proliferating Cells. *Cell* **162**, 552-563, doi:10.1016/j.cell.2015.07.017 (2015).
35 Moffett, J. R., Puthillathu, N., Vengilote, R., Jaworski, D. M. & Namboodiri, A. M. Acetate Revisited: A Key Biomolecule at the Nexus of Metabolism,

Epigenetics, and Oncogenesis - Part 2: Acetate and ACSS2 in Health and Disease. *Front Physiol* **11**, 580171, doi:10.3389/fphys.2020.580171 (2020).
36 Chandel, N. S. *Navigating Metabolism*. (Cold Spring Harbor Laboratory Press, 2015).
37 Behal, R. H., Buxton, D. B., Robertson, J. G. & Olson, M. S. Regulation of the pyruvate dehydrogenase multienzyme complex. *Annu Rev Nutr* **13**, 497-520, doi:10.1146/annurev.nu.13.070193.002433 (1993).
38 Warburg, O., Posener, K., Negelein E. Ueber den stoffwechsel der tumoren. *Biochem. Z.* **152**, 319-344 (1924).
39 Vander Heiden, M. G., Cantley, L. C. & Thompson, C. B. Understanding the Warburg effect: the metabolic requirements of cell proliferation. *Science* **324**, 1029-1033, doi:10.1126/science.1160809 (2009).
40 Houten, S. M. & Wanders, R. J. A general introduction to the biochemistry of mitochondrial fatty acid beta-oxidation. *J Inherit Metab Dis* **33**, 469-477, doi:10.1007/s10545-010-9061-2 (2010).
41 Chatelain, F. *et al.* Cyclic AMP and fatty acids increase carnitine palmitoyltransferase I gene transcription in cultured fetal rat hepatocytes. *Eur J Biochem* **235**, 789-798, doi:10.1111/j.1432-1033.1996.00789.x (1996).
42 Mascaro, C. *et al.* Control of human muscle-type carnitine palmitoyltransferase I gene transcription by peroxisome proliferator-activated receptor. *J Biol Chem* **273**, 8560-8563, doi:10.1074/jbc.273.15.8560 (1998).
43 Kennedy, K. M. *et al.* Catabolism of exogenous lactate reveals it as a legitimate metabolic substrate in breast cancer. *PLoS One* **8**, e75154, doi:10.1371/journal.pone.0075154 (2013).
44 Faubert, B. *et al.* Lactate Metabolism in Human Lung Tumors. *Cell* **171**, 358-371 e359, doi:10.1016/j.cell.2017.09.019 (2017).
45 Hui, S. *et al.* Glucose feeds the TCA cycle via circulating lactate. *Nature* **551**, 115-118, doi:10.1038/nature24057 (2017).
46 Chen, Y. J. *et al.* Lactate metabolism is associated with mammalian mitochondria. *Nat Chem Biol* **12**, 937-943, doi:10.1038/nchembio.2172 (2016).
47 Holecek, M. Branched-chain amino acids in health and disease: metabolism, alterations in blood plasma, and as supplements. *Nutr Metab (Lond)* **15**, 33, doi:10.1186/s12986-018-0271-1 (2018).
48 Buse, M. G., Biggers, J. F., Friderici, K. H. & Buse, J. F. Oxidation of branched chain amino acids by isolated hearts and diaphragms of the rat. The effect of fatty acids, glucose, and pyruvate respiration. *J Biol Chem* **247**, 8085-8096 (1972).
49 Green, C. R. *et al.* Branched-chain amino acid catabolism fuels adipocyte differentiation and lipogenesis. *Nat Chem Biol* **12**, 15-21, doi:10.1038/nchembio.1961 (2016).
50 Utter, M. F. & Keech, D. B. Pyruvate Carboxylase. I. Nature of the Reaction. *J Biol Chem* **238**, 2603-2608 (1963).
51 McClure, W. R., Lardy, H. A. & Kneifel, H. P. Rat liver pyruvate carboxylase. I. Preparation, properties, and cation specificity. *J Biol Chem* **246**, 3569-3578 (1971).

52 Scrutton, M. C. & White, M. D. Pyruvate carboxylase. Inhibition of the mammalian and avian liver enzymes by alpha-ketoglutarate and L-glutamate. *J Biol Chem* **249**, 5405-5415 (1974).
53 Lussey-Lepoutre, C. *et al.* Loss of succinate dehydrogenase activity results in dependency on pyruvate carboxylation for cellular anabolism. *Nat Commun* **6**, 8784, doi:10.1038/ncomms9784 (2015).
54 Cardaci, S. *et al.* Pyruvate carboxylation enables growth of SDH-deficient cells by supporting aspartate biosynthesis. *Nat Cell Biol* **17**, 1317-1326, doi:10.1038/ncb3233 (2015).
55 Fan, J. *et al.* Glutamine-driven oxidative phosphorylation is a major ATP source in transformed mammalian cells in both normoxia and hypoxia. *Mol Syst Biol* **9**, 712, doi:10.1038/msb.2013.65 (2013).
56 DeBerardinis, R. J. *et al.* Beyond aerobic glycolysis: transformed cells can engage in glutamine metabolism that exceeds the requirement for protein and nucleotide synthesis. *Proc Natl Acad Sci U S A* **104**, 19345-19350, doi:10.1073/pnas.0709747104 (2007).
57 DeBerardinis, R. J., Lum, J. J., Hatzivassiliou, G. & Thompson, C. B. The biology of cancer: metabolic reprogramming fuels cell growth and proliferation. *Cell Metab* **7**, 11-20, doi:10.1016/j.cmet.2007.10.002 (2008).
58 Muir, A. *et al.* Environmental cystine drives glutamine anaplerosis and sensitizes cancer cells to glutaminase inhibition. *Elife* **6**, doi:10.7554/eLife.27713 (2017).
59 Eagle, H. Nutrition needs of mammalian cells in tissue culture. *Science* **122**, 501-514, doi:10.1126/science.122.3168.501 (1955).
60 Eagle, H., Oyama, V. I., Levy, M., Horton, C. L. & Fleischman, R. The growth response of mammalian cells in tissue culture to L-glutamine and L-glutamic acid. *J Biol Chem* **218**, 607-616 (1956).
61 DeBerardinis, R. J. & Cheng, T. Q's next: the diverse functions of glutamine in metabolism, cell biology and cancer. *Oncogene* **29**, 313-324, doi:10.1038/onc.2009.358 (2010).
62 Lane, A. N. & Fan, T. W. Regulation of mammalian nucleotide metabolism and biosynthesis. *Nucleic Acids Res* **43**, 2466-2485, doi:10.1093/nar/gkv047 (2015).
63 Yang, C. *et al.* Glutamine oxidation maintains the TCA cycle and cell survival during impaired mitochondrial pyruvate transport. *Mol Cell* **56**, 414-424, doi:10.1016/j.molcel.2014.09.025 (2014).
64 Son, J. *et al.* Glutamine supports pancreatic cancer growth through a KRAS-regulated metabolic pathway. *Nature* **496**, 101-105, doi:10.1038/nature12040 (2013).
65 Yang, C. *et al.* Glioblastoma cells require glutamate dehydrogenase to survive impairments of glucose metabolism or Akt signaling. *Cancer Res* **69**, 7986-7993, doi:10.1158/0008-5472.CAN-09-2266 (2009).
66 Metallo, C. M. *et al.* Reductive glutamine metabolism by IDH1 mediates lipogenesis under hypoxia. *Nature* **481**, 380-384, doi:10.1038/nature10602 (2011).
67 Mullen, A. R. *et al.* Reductive carboxylation supports growth in tumour cells with defective mitochondria. *Nature* **481**, 385-388, doi:10.1038/nature10642 (2011).

68 Cheng, T. *et al.* Pyruvate carboxylase is required for glutamine-independent growth of tumor cells. *Proc Natl Acad Sci U S A* **108**, 8674-8679, doi:10.1073/pnas.1016627108 (2011).
69 Liu, Y., Hu, L., Ma, T., Yang, J. & Ding, J. Insights into the inhibitory mechanisms of NADH on the alphagamma heterodimer of human NAD-dependent isocitrate dehydrogenase. *Sci Rep* **8**, 3146, doi:10.1038/s41598-018-21584-7 (2018).
70 Martinez-Reyes, I. & Chandel, N. S. Mitochondrial TCA cycle metabolites control physiology and disease. *Nat Commun* **11**, 102, doi:10.1038/s41467-019-13668-3 (2020).
71 Gabriel, J. L., Zervos, P. R. & Plaut, G. W. Activity of purified NAD-specific isocitrate dehydrogenase at modulator and substrate concentrations approximating conditions in mitochondria. *Metabolism* **35**, 661-667, doi:10.1016/0026-0495(86)90175-7 (1986).
72 LaNoue, K. F., Bryla, J. & Williamson, J. R. Feedback interactions in the control of citric acid cycle activity in rat heart mitochondria. *J Biol Chem* **247**, 667-679 (1972).
73 Fink, B. D. *et al.* Oxaloacetic acid mediates ADP-dependent inhibition of mitochondrial complex II-driven respiration. *J Biol Chem* **293**, 19932-19941, doi:10.1074/jbc.RA118.005144 (2018).
74 Luengo, A. *et al.* Increased demand for NAD(+) relative to ATP drives aerobic glycolysis. *Mol Cell* **81**, 691-707 e696, doi:10.1016/j.molcel.2020.12.012 (2021).
75 Korotchkina, L. G. & Patel, M. S. Site specificity of four pyruvate dehydrogenase kinase isoenzymes toward the three phosphorylation sites of human pyruvate dehydrogenase. *J Biol Chem* **276**, 37223-37229, doi:10.1074/jbc.M103069200 (2001).
76 Sugden, M. C. & Holness, M. J. Recent advances in mechanisms regulating glucose oxidation at the level of the pyruvate dehydrogenase complex by PDKs. *Am J Physiol Endocrinol Metab* **284**, E855-862, doi:10.1152/ajpendo.00526.2002 (2003).
77 Kim, J. W., Gao, P., Liu, Y. C., Semenza, G. L. & Dang, C. V. Hypoxia-inducible factor 1 and dysregulated c-Myc cooperatively induce vascular endothelial growth factor and metabolic switches hexokinase 2 and pyruvate dehydrogenase kinase 1. *Mol Cell Biol* **27**, 7381-7393, doi:10.1128/MCB.00440-07 (2007).
78 Patron, M. *et al.* The mitochondrial calcium uniporter (MCU): molecular identity and physiological roles. *J Biol Chem* **288**, 10750-10758, doi:10.1074/jbc.R112.420752 (2013).
79 Gherardi, G., Monticelli, H., Rizzuto, R. & Mammucari, C. The Mitochondrial Ca(2+) Uptake and the Fine-Tuning of Aerobic Metabolism. *Front Physiol* **11**, 554904, doi:10.3389/fphys.2020.554904 (2020).
80 Denton, R. M., Randle, P. J. & Martin, B. R. Stimulation by calcium ions of pyruvate dehydrogenase phosphate phosphatase. *Biochem J* **128**, 161-163, doi:10.1042/bj1280161 (1972).
81 Cantor, J. R. *et al.* Physiologic Medium Rewires Cellular Metabolism and Reveals Uric Acid as an Endogenous Inhibitor of UMP Synthase. *Cell* **169**, 258-272 e217, doi:10.1016/j.cell.2017.03.023 (2017).

82 Li, X. *et al.* Circulating metabolite homeostasis achieved through mass action. *Nat Metab* **4**, 141-152, doi:10.1038/s42255-021-00517-1 (2022).
83 Kim, J. & DeBerardinis, R. J. Mechanisms and Implications of Metabolic Heterogeneity in Cancer. *Cell Metab* **30**, 434-446, doi:10.1016/j.cmet.2019.08.013 (2019).
84 Sullivan, M. R. *et al.* Quantification of microenvironmental metabolites in murine cancers reveals determinants of tumor nutrient availability. *Elife* **8**, doi:10.7554/eLife.44235 (2019).
85 Warburg, O., Wind, F. & Negelein, E. The Metabolism of Tumors in the Body. *J Gen Physiol* **8**, 519-530, doi:10.1085/jgp.8.6.519 (1927).
86 Pavlova, N. N. & Thompson, C. B. The Emerging Hallmarks of Cancer Metabolism. *Cell Metab* **23**, 27-47, doi:10.1016/j.cmet.2015.12.006 (2016).
87 Warburg, O. On the origin of cancer cells. *Science* **123**, 309-314, doi:10.1126/science.123.3191.309 (1956).
88 Frauwirth, K. A. *et al.* The CD28 signaling pathway regulates glucose metabolism. *Immunity* **16**, 769-777, doi:10.1016/s1074-7613(02)00323-0 (2002).
89 Maher, E. A. *et al.* Metabolism of [U-13 C]glucose in human brain tumors in vivo. *NMR Biomed* **25**, 1234-1244, doi:10.1002/nbm.2794 (2012).
90 Marin-Valencia, I. *et al.* Analysis of tumor metabolism reveals mitochondrial glucose oxidation in genetically diverse human glioblastomas in the mouse brain in vivo. *Cell Metab* **15**, 827-837, doi:10.1016/j.cmet.2012.05.001 (2012).
91 Weinberg, F. *et al.* Mitochondrial metabolism and ROS generation are essential for Kras-mediated tumorigenicity. *Proc Natl Acad Sci U S A* **107**, 8788-8793, doi:10.1073/pnas.1003428107 (2010).
92 Kuntz, E. M. *et al.* Targeting mitochondrial oxidative phosphorylation eradicates therapy-resistant chronic myeloid leukemia stem cells. *Nat Med* **23**, 1234-1240, doi:10.1038/nm.4399 (2017).
93 Martinez-Reyes, I. *et al.* Mitochondrial ubiquinol oxidation is necessary for tumour growth. *Nature* **585**, 288-292, doi:10.1038/s41586-020-2475-6 (2020).
94 Barthel, A. *et al.* Regulation of GLUT1 gene transcription by the serine/threonine kinase Akt1. *J Biol Chem* **274**, 20281-20286, doi:10.1074/jbc.274.29.20281 (1999).
95 Gottlob, K. *et al.* Inhibition of early apoptotic events by Akt/PKB is dependent on the first committed step of glycolysis and mitochondrial hexokinase. *Genes Dev* **15**, 1406-1418, doi:10.1101/gad.889901 (2001).
96 Lawrence, M. S. *et al.* Discovery and saturation analysis of cancer genes across 21 tumour types. *Nature* **505**, 495-501, doi:10.1038/nature12912 (2014).
97 Gao, P. *et al.* c-Myc suppression of miR-23a/b enhances mitochondrial glutaminase expression and glutamine metabolism. *Nature* **458**, 762-765, doi:10.1038/nature07823 (2009).
98 Wise, D. R. *et al.* Myc regulates a transcriptional program that stimulates mitochondrial glutaminolysis and leads to glutamine addiction. *Proc Natl Acad Sci U S A* **105**, 18782-18787, doi:10.1073/pnas.0810199105 (2008).
99 Yuneva, M., Zamboni, N., Oefner, P., Sachidanandam, R. & Lazebnik, Y. Deficiency in glutamine but not glucose induces MYC-dependent apoptosis in human cells. *J Cell Biol* **178**, 93-105, doi:10.1083/jcb.200703099 (2007).

100 Yuneva, M. O. *et al.* The metabolic profile of tumors depends on both the responsible genetic lesion and tissue type. *Cell Metab* **15**, 157-170, doi:10.1016/j.cmet.2011.12.015 (2012).
101 Ahuja, P. *et al.* Myc controls transcriptional regulation of cardiac metabolism and mitochondrial biogenesis in response to pathological stress in mice. *J Clin Invest* **120**, 1494-1505, doi:10.1172/JCI38331 (2010).
102 Osthus, R. C. *et al.* Deregulation of glucose transporter 1 and glycolytic gene expression by c-Myc. *J Biol Chem* **275**, 21797-21800, doi:10.1074/jbc.C000023200 (2000).
103 Shim, H. *et al.* c-Myc transactivation of LDH-A: implications for tumor metabolism and growth. *Proc Natl Acad Sci U S A* **94**, 6658-6663, doi:10.1073/pnas.94.13.6658 (1997).
104 Stine, Z. E., Walton, Z. E., Altman, B. J., Hsieh, A. L. & Dang, C. V. MYC, Metabolism, and Cancer. *Cancer Discov* **5**, 1024-1039, doi:10.1158/2159-8290.CD-15-0507 (2015).
105 Palm, W. Metabolic functions of macropinocytosis. *Philos Trans R Soc Lond B Biol Sci* **374**, 20180285, doi:10.1098/rstb.2018.0285 (2019).
106 Bar-Sagi, D. & Feramisco, J. R. Induction of membrane ruffling and fluid-phase pinocytosis in quiescent fibroblasts by ras proteins. *Science* **233**, 1061-1068, doi:10.1126/science.3090687 (1986).
107 Commisso, C. *et al.* Macropinocytosis of protein is an amino acid supply route in Ras-transformed cells. *Nature* **497**, 633-637, doi:10.1038/nature12138 (2013).
108 Brown, M. S. & Goldstein, J. L. Receptor-mediated endocytosis: insights from the lipoprotein receptor system. *Proc Natl Acad Sci U S A* **76**, 3330-3337, doi:10.1073/pnas.76.7.3330 (1979).
109 Lum, J. J. *et al.* Growth factor regulation of autophagy and cell survival in the absence of apoptosis. *Cell* **120**, 237-248, doi:10.1016/j.cell.2004.11.046 (2005).
110 Yakes, F. M. & Van Houten, B. Mitochondrial DNA damage is more extensive and persists longer than nuclear DNA damage in human cells following oxidative stress. *Proc Natl Acad Sci U S A* **94**, 514-519, doi:10.1073/pnas.94.2.514 (1997).
111 DeBerardinis, R. J. & Chandel, N. S. Fundamentals of cancer metabolism. *Sci Adv* **2**, e1600200, doi:10.1126/sciadv.1600200 (2016).
112 Lee, S. R. *et al.* Reversible inactivation of the tumor suppressor PTEN by H2O2. *J Biol Chem* **277**, 20336-20342, doi:10.1074/jbc.M111899200 (2002).
113 Lee, S. R., Kwon, K. S., Kim, S. R. & Rhee, S. G. Reversible inactivation of protein-tyrosine phosphatase 1B in A431 cells stimulated with epidermal growth factor. *J Biol Chem* **273**, 15366-15372, doi:10.1074/jbc.273.25.15366 (1998).
114 Finkel, T. Signal transduction by reactive oxygen species. *J Cell Biol* **194**, 7-15, doi:10.1083/jcb.201102095 (2011).
115 Cheung, E. C. & Vousden, K. H. The role of ROS in tumour development and progression. *Nat Rev Cancer*, doi:10.1038/s41568-021-00435-0 (2022).
116 van der Reest, J., Lilla, S., Zheng, L., Zanivan, S. & Gottlieb, E. Proteome-wide analysis of cysteine oxidation reveals metabolic sensitivity to redox stress. *Nat Commun* **9**, 1581, doi:10.1038/s41467-018-04003-3 (2018).
117 Szatrowski, T. P. & Nathan, C. F. Production of large amounts of hydrogen peroxide by human tumor cells. *Cancer Res* **51**, 794-798 (1991).

118 Nieborowska-Skorska, M. *et al.* Rac2-MRC-cIII-generated ROS cause genomic instability in chronic myeloid leukemia stem cells and primitive progenitors. *Blood* **119**, 4253-4263, doi:10.1182/blood-2011-10-385658 (2012).
119 Tran, T. Q. *et al.* alpha-Ketoglutarate attenuates Wnt signaling and drives differentiation in colorectal cancer. *Nat Cancer* **1**, 345-358, doi:10.1038/s43018-020-0035-5 (2020).
120 Raffel, S. *et al.* BCAT1 restricts alphaKG levels in AML stem cells leading to IDHmut-like DNA hypermethylation. *Nature* **551**, 384-388, doi:10.1038/nature24294 (2017).
121 Carey, B. W., Finley, L. W., Cross, J. R., Allis, C. D. & Thompson, C. B. Intracellular alpha-ketoglutarate maintains the pluripotency of embryonic stem cells. *Nature* **518**, 413-416, doi:10.1038/nature13981 (2015).
122 Hwang, I. Y. *et al.* Psat1-Dependent Fluctuations in alpha-Ketoglutarate Affect the Timing of ESC Differentiation. *Cell Metab* **24**, 494-501, doi:10.1016/j.cmet.2016.06.014 (2016).
123 Lu, C. *et al.* IDH mutation impairs histone demethylation and results in a block to cell differentiation. *Nature* **483**, 474-478, doi:10.1038/nature10860 (2012).
124 Figueroa, M. E. *et al.* Leukemic IDH1 and IDH2 mutations result in a hypermethylation phenotype, disrupt TET2 function, and impair hematopoietic differentiation. *Cancer Cell* **18**, 553-567, doi:10.1016/j.ccr.2010.11.015 (2010).
125 Saha, S. K. *et al.* Mutant IDH inhibits HNF-4alpha to block hepatocyte differentiation and promote biliary cancer. *Nature* **513**, 110-114, doi:10.1038/nature13441 (2014).
126 Ward, P. S. *et al.* The common feature of leukemia-associated IDH1 and IDH2 mutations is a neomorphic enzyme activity converting alpha-ketoglutarate to 2-hydroxyglutarate. *Cancer Cell* **17**, 225-234, doi:10.1016/j.ccr.2010.01.020 (2010).
127 Dang, L. *et al.* Cancer-associated IDH1 mutations produce 2-hydroxyglutarate. *Nature* **462**, 739-744, doi:10.1038/nature08617 (2009).
128 Yan, H. *et al.* IDH1 and IDH2 mutations in gliomas. *N Engl J Med* **360**, 765-773, doi:10.1056/NEJMoa0808710 (2009).
129 Mardis, E. R. *et al.* Recurring mutations found by sequencing an acute myeloid leukemia genome. *N Engl J Med* **361**, 1058-1066, doi:10.1056/NEJMoa0903840 (2009).
130 Intlekofer, A. M. *et al.* Hypoxia Induces Production of L-2-Hydroxyglutarate. *Cell Metab* **22**, 304-311, doi:10.1016/j.cmet.2015.06.023 (2015).
131 Oldham, W. M., Clish, C. B., Yang, Y. & Loscalzo, J. Hypoxia-Mediated Increases in L-2-hydroxyglutarate Coordinate the Metabolic Response to Reductive Stress. *Cell Metab* **22**, 291-303, doi:10.1016/j.cmet.2015.06.021 (2015).
132 Intlekofer, A. M. *et al.* L-2-Hydroxyglutarate production arises from noncanonical enzyme function at acidic pH. *Nat Chem Biol* **13**, 494-500, doi:10.1038/nchembio.2307 (2017).
133 Nadtochiy, S. M. *et al.* Acidic pH Is a Metabolic Switch for 2-Hydroxyglutarate Generation and Signaling. *J Biol Chem* **291**, 20188-20197, doi:10.1074/jbc.M116.738799 (2016).

134 Xiao, M. *et al.* Inhibition of alpha-KG-dependent histone and DNA demethylases by fumarate and succinate that are accumulated in mutations of FH and SDH tumor suppressors. *Genes Dev* **26**, 1326-1338, doi:10.1101/gad.191056.112 (2012).
135 Cervera, A. M., Bayley, J. P., Devilee, P. & McCreath, K. J. Inhibition of succinate dehydrogenase dysregulates histone modification in mammalian cells. *Mol Cancer* **8**, 89, doi:10.1186/1476-4598-8-89 (2009).
136 Tomlinson, I. P. *et al.* Germline mutations in FH predispose to dominantly inherited uterine fibroids, skin leiomyomata and papillary renal cell cancer. *Nat Genet* **30**, 406-410, doi:10.1038/ng849 (2002).
137 Baysal, B. E. *et al.* Mutations in SDHD, a mitochondrial complex II gene, in hereditary paraganglioma. *Science* **287**, 848-851, doi:10.1126/science.287.5454.848 (2000).
138 Hao, H. X. *et al.* SDH5, a gene required for flavination of succinate dehydrogenase, is mutated in paraganglioma. *Science* **325**, 1139-1142, doi:10.1126/science.1175689 (2009).
139 Selak, M. A. *et al.* Succinate links TCA cycle dysfunction to oncogenesis by inhibiting HIF-alpha prolyl hydroxylase. *Cancer Cell* **7**, 77-85, doi:10.1016/j.ccr.2004.11.022 (2005).
140 Isaacs, J. S. *et al.* HIF overexpression correlates with biallelic loss of fumarate hydratase in renal cancer: novel role of fumarate in regulation of HIF stability. *Cancer Cell* **8**, 143-153, doi:10.1016/j.ccr.2005.06.017 (2005).
141 Sullivan, L. B. *et al.* The proto-oncometabolite fumarate binds glutathione to amplify ROS-dependent signaling. *Mol Cell* **51**, 236-248, doi:10.1016/j.molcel.2013.05.003 (2013).
142 Cai, L., Sutter, B. M., Li, B. & Tu, B. P. Acetyl-CoA induces cell growth and proliferation by promoting the acetylation of histones at growth genes. *Mol Cell* **42**, 426-437, doi:10.1016/j.molcel.2011.05.004 (2011).
143 Wellen, K. E. *et al.* ATP-citrate lyase links cellular metabolism to histone acetylation. *Science* **324**, 1076-1080, doi:10.1126/science.1164097 (2009).
144 Lee, J. V. *et al.* Akt-dependent metabolic reprogramming regulates tumor cell histone acetylation. *Cell Metab* **20**, 306-319, doi:10.1016/j.cmet.2014.06.004 (2014).
145 Muir, A., Danai, L. V. & Vander Heiden, M. G. Microenvironmental regulation of cancer cell metabolism: implications for experimental design and translational studies. *Dis Model Mech* **11**, doi:10.1242/dmm.035758 (2018).
146 Jang, C., Chen, L. & Rabinowitz, J. D. Metabolomics and Isotope Tracing. *Cell* **173**, 822-837, doi:10.1016/j.cell.2018.03.055 (2018).
147 Davidson, S. M. *et al.* Environment Impacts the Metabolic Dependencies of Ras-Driven Non-Small Cell Lung Cancer. *Cell Metab* **23**, 517-528, doi:10.1016/j.cmet.2016.01.007 (2016).
148 Courtney, K. D. *et al.* Isotope Tracing of Human Clear Cell Renal Cell Carcinomas Demonstrates Suppressed Glucose Oxidation In Vivo. *Cell Metab* **28**, 793-800 e792, doi:10.1016/j.cmet.2018.07.020 (2018).
149 Mashimo, T. *et al.* Acetate is a bioenergetic substrate for human glioblastoma and brain metastases. *Cell* **159**, 1603-1614, doi:10.1016/j.cell.2014.11.025 (2014).

150 Comerford, S. A. *et al.* Acetate dependence of tumors. *Cell* **159**, 1591-1602, doi:10.1016/j.cell.2014.11.020 (2014).
151 Zheng, X. *et al.* Metabolic reprogramming during neuronal differentiation from aerobic glycolysis to neuronal oxidative phosphorylation. *Elife* **5**, doi:10.7554/eLife.13374 (2016).
152 Shapira, S. N. & Christofk, H. R. Metabolic Regulation of Tissue Stem Cells. *Trends Cell Biol* **30**, 566-576, doi:10.1016/j.tcb.2020.04.004 (2020).
153 Rodriguez-Colman, M. J. *et al.* Interplay between metabolic identities in the intestinal crypt supports stem cell function. *Nature* **543**, 424-427, doi:10.1038/nature21673 (2017).
154 Schell, J. C. *et al.* Control of intestinal stem cell function and proliferation by mitochondrial pyruvate metabolism. *Nat Cell Biol* **19**, 1027-1036, doi:10.1038/ncb3593 (2017).
155 Wei, P., Dove, K. K., Bensard, C., Schell, J. C. & Rutter, J. The Force Is Strong with This One: Metabolism (Over)powers Stem Cell Fate. *Trends Cell Biol* **28**, 551-559, doi:10.1016/j.tcb.2018.02.007 (2018).
156 Flores, A. *et al.* Lactate dehydrogenase activity drives hair follicle stem cell activation. *Nat Cell Biol* **19**, 1017-1026, doi:10.1038/ncb3575 (2017).
157 Leary, S. C., Battersby, B. J., Hansford, R. G. & Moyes, C. D. Interactions between bioenergetics and mitochondrial biogenesis. *Biochim Biophys Acta* **1365**, 522-530, doi:10.1016/s0005-2728(98)00105-4 (1998).
158 Weinberger, L., Ayyash, M., Novershtern, N. & Hanna, J. H. Dynamic stem cell states: naive to primed pluripotency in rodents and humans. *Nat Rev Mol Cell Biol* **17**, 155-169, doi:10.1038/nrm.2015.28 (2016).
159 Torres-Padilla, M. E. & Chambers, I. Transcription factor heterogeneity in pluripotent stem cells: a stochastic advantage. *Development* **141**, 2173-2181, doi:10.1242/dev.102624 (2014).
160 Marks, H. *et al.* The transcriptional and epigenomic foundations of ground state pluripotency. *Cell* **149**, 590-604, doi:10.1016/j.cell.2012.03.026 (2012).
161 Ying, Q. L. *et al.* The ground state of embryonic stem cell self-renewal. *Nature* **453**, 519-523, doi:10.1038/nature06968 (2008).
162 Leitch, H. G. *et al.* Naive pluripotency is associated with global DNA hypomethylation. *Nat Struct Mol Biol* **20**, 311-316, doi:10.1038/nsmb.2510 (2013).
163 Takashima, Y. *et al.* Resetting transcription factor control circuitry toward ground-state pluripotency in human. *Cell* **158**, 1254-1269, doi:10.1016/j.cell.2014.08.029 (2014).
164 Palm, W. & Thompson, C. B. Nutrient acquisition strategies of mammalian cells. *Nature* **546**, 234-242, doi:10.1038/nature22379 (2017).
165 Vander Heiden, M. G. & DeBerardinis, R. J. Understanding the Intersections between Metabolism and Cancer Biology. *Cell* **168**, 657-669, doi:10.1016/j.cell.2016.12.039 (2017).
166 Schvartzman, J. M., Thompson, C. B. & Finley, L. W. S. Metabolic regulation of chromatin modifications and gene expression. *J Cell Biol* **217**, 2247-2259, doi:10.1083/jcb.201803061 (2018).

167 Saxton, R. A. & Sabatini, D. M. mTOR Signaling in Growth, Metabolism, and Disease. *Cell* **168**, 960-976, doi:10.1016/j.cell.2017.02.004 (2017).
168 Su, X., Wellen, K. E. & Rabinowitz, J. D. Metabolic control of methylation and acetylation. *Curr Opin Chem Biol* **30**, 52-60, doi:10.1016/j.cbpa.2015.10.030 (2016).
169 Lu, C. & Thompson, C. B. Metabolic regulation of epigenetics. *Cell Metab* **16**, 9-17, doi:10.1016/j.cmet.2012.06.001 (2012).
170 Gu, W. *et al.* Glycolytic Metabolism Plays a Functional Role in Regulating Human Pluripotent Stem Cell State. *Cell Stem Cell* **19**, 476-490, doi:10.1016/j.stem.2016.08.008 (2016).
171 Tohyama, S. *et al.* Glutamine Oxidation Is Indispensable for Survival of Human Pluripotent Stem Cells. *Cell Metab* **23**, 663-674, doi:10.1016/j.cmet.2016.03.001 (2016).
172 Zhang, H. *et al.* Distinct Metabolic States Can Support Self-Renewal and Lipogenesis in Human Pluripotent Stem Cells under Different Culture Conditions. *Cell Rep* **16**, 1536-1547, doi:10.1016/j.celrep.2016.06.102 (2016).
173 Moussaieff, A. *et al.* Glycolysis-mediated changes in acetyl-CoA and histone acetylation control the early differentiation of embryonic stem cells. *Cell Metab* **21**, 392-402, doi:10.1016/j.cmet.2015.02.002 (2015).
174 TeSlaa, T. *et al.* alpha-Ketoglutarate Accelerates the Initial Differentiation of Primed Human Pluripotent Stem Cells. *Cell Metab* **24**, 485-493, doi:10.1016/j.cmet.2016.07.002 (2016).
175 Chambers, I. *et al.* Nanog safeguards pluripotency and mediates germline development. *Nature* **450**, 1230-1234, doi:10.1038/nature06403 (2007).
176 Filipczyk, A. *et al.* Biallelic expression of nanog protein in mouse embryonic stem cells. *Cell Stem Cell* **13**, 12-13, doi:10.1016/j.stem.2013.04.025 (2013).
177 Chisolm, D. A. *et al.* CCCTC-Binding Factor Translates Interleukin 2- and alpha-Ketoglutarate-Sensitive Metabolic Changes in T Cells into Context-Dependent Gene Programs. *Immunity* **47**, 251-267 e257, doi:10.1016/j.immuni.2017.07.015 (2017).
178 Liu, P. S. *et al.* alpha-ketoglutarate orchestrates macrophage activation through metabolic and epigenetic reprogramming. *Nat Immunol* **18**, 985-994, doi:10.1038/ni.3796 (2017).
179 Yang, Q. *et al.* AMPK/alpha-Ketoglutarate Axis Dynamically Mediates DNA Demethylation in the Prdm16 Promoter and Brown Adipogenesis. *Cell Metab* **24**, 542-554, doi:10.1016/j.cmet.2016.08.010 (2016).
180 Burdon, T., Stracey, C., Chambers, I., Nichols, J. & Smith, A. Suppression of SHP-2 and ERK signalling promotes self-renewal of mouse embryonic stem cells. *Dev Biol* **210**, 30-43, doi:10.1006/dbio.1999.9265 (1999).
181 van Oosten, A. L., Costa, Y., Smith, A. & Silva, J. C. JAK/STAT3 signalling is sufficient and dominant over antagonistic cues for the establishment of naive pluripotency. *Nat Commun* **3**, 817, doi:10.1038/ncomms1822 (2012).
182 Martello, G., Bertone, P. & Smith, A. Identification of the missing pluripotency mediator downstream of leukaemia inhibitory factor. *EMBO J* **32**, 2561-2574, doi:10.1038/emboj.2013.177 (2013).

183 Chambers, I. *et al.* Functional expression cloning of Nanog, a pluripotency sustaining factor in embryonic stem cells. *Cell* **113**, 643-655 (2003).
184 Mitsui, K. *et al.* The homeoprotein Nanog is required for maintenance of pluripotency in mouse epiblast and ES cells. *Cell* **113**, 631-642 (2003).
185 Zhang, P., Andrianakos, R., Yang, Y., Liu, C. & Lu, W. Kruppel-like factor 4 (Klf4) prevents embryonic stem (ES) cell differentiation by regulating Nanog gene expression. *J Biol Chem* **285**, 9180-9189, doi:10.1074/jbc.M109.077958 (2010).
186 Festuccia, N. *et al.* Esrrb is a direct Nanog target gene that can substitute for Nanog function in pluripotent cells. *Cell Stem Cell* **11**, 477-490, doi:10.1016/j.stem.2012.08.002 (2012).
187 Shi, W. *et al.* Regulation of the pluripotency marker Rex-1 by Nanog and Sox2. *J Biol Chem* **281**, 23319-23325, doi:10.1074/jbc.M601811200 (2006).
188 Faddah, D. A. *et al.* Single-cell analysis reveals that expression of nanog is biallelic and equally variable as that of other pluripotency factors in mouse ESCs. *Cell Stem Cell* **13**, 23-29, doi:10.1016/j.stem.2013.04.019 (2013).
189 Boroviak, T., Loos, R., Bertone, P., Smith, A. & Nichols, J. The ability of inner-cell-mass cells to self-renew as embryonic stem cells is acquired following epiblast specification. *Nat Cell Biol* **16**, 516-528, doi:10.1038/ncb2965 (2014).
190 Karwacki-Neisius, V. *et al.* Reduced Oct4 expression directs a robust pluripotent state with distinct signaling activity and increased enhancer occupancy by Oct4 and Nanog. *Cell Stem Cell* **12**, 531-545, doi:10.1016/j.stem.2013.04.023 (2013).
191 Silva, J. *et al.* Nanog is the gateway to the pluripotent ground state. *Cell* **138**, 722-737, doi:10.1016/j.cell.2009.07.039 (2009).
192 Nichols, J. *et al.* Formation of pluripotent stem cells in the mammalian embryo depends on the POU transcription factor Oct4. *Cell* **95**, 379-391 (1998).
193 Hochedlinger, K. & Jaenisch, R. Induced Pluripotency and Epigenetic Reprogramming. *Cold Spring Harb Perspect Biol* **7**, doi:10.1101/cshperspect.a019448 (2015).
194 Silva, J. *et al.* Promotion of reprogramming to ground state pluripotency by signal inhibition. *PLoS Biol* **6**, e253, doi:10.1371/journal.pbio.0060253 (2008).
195 Stadtfeld, M., Maherali, N., Borkent, M. & Hochedlinger, K. A reprogrammable mouse strain from gene-targeted embryonic stem cells. *Nat Methods* **7**, 53-55, doi:10.1038/nmeth.1409 (2010).
196 Dunn, S. J., Martello, G., Yordanov, B., Emmott, S. & Smith, A. G. Defining an essential transcription factor program for naive pluripotency. *Science* **344**, 1156-1160, doi:10.1126/science.1248882 (2014).
197 Buganim, Y. *et al.* The developmental potential of iPSCs is greatly influenced by reprogramming factor selection. *Cell Stem Cell* **15**, 295-309, doi:10.1016/j.stem.2014.07.003 (2014).
198 Choi, J. *et al.* Prolonged Mek1/2 suppression impairs the developmental potential of embryonic stem cells. *Nature* **548**, 219-223, doi:10.1038/nature23274 (2017).
199 Yagi, M. *et al.* Derivation of ground-state female ES cells maintaining gamete-derived DNA methylation. *Nature* **548**, 224-227, doi:10.1038/nature23286 (2017).

200 Huang, K., Maruyama, T. & Fan, G. The naive state of human pluripotent stem cells: a synthesis of stem cell and preimplantation embryo transcriptome analyses. *Cell Stem Cell* **15**, 410-415, doi:10.1016/j.stem.2014.09.014 (2014).
201 Wang, J. *et al.* Isolation and cultivation of naive-like human pluripotent stem cells based on HERVH expression. *Nat Protoc* **11**, 327-346, doi:10.1038/nprot.2016.016 (2016).
202 Warrier, S. *et al.* Direct comparison of distinct naive pluripotent states in human embryonic stem cells. *Nat Commun* **8**, 15055, doi:10.1038/ncomms15055 (2017).
203 Carbognin, E., Betto, R. M., Soriano, M. E., Smith, A. G. & Martello, G. Stat3 promotes mitochondrial transcription and oxidative respiration during maintenance and induction of naive pluripotency. *EMBO J* **35**, 618-634, doi:10.15252/embj.201592629 (2016).
204 Ficz, G. *et al.* FGF signaling inhibition in ESCs drives rapid genome-wide demethylation to the epigenetic ground state of pluripotency. *Cell Stem Cell* **13**, 351-359, doi:10.1016/j.stem.2013.06.004 (2013).
205 Habibi, E. *et al.* Whole-genome bisulfite sequencing of two distinct interconvertible DNA methylomes of mouse embryonic stem cells. *Cell Stem Cell* **13**, 360-369, doi:10.1016/j.stem.2013.06.002 (2013).
206 Galonska, C., Ziller, M. J., Karnik, R. & Meissner, A. Ground State Conditions Induce Rapid Reorganization of Core Pluripotency Factor Binding before Global Epigenetic Reprogramming. *Cell Stem Cell* **17**, 462-470, doi:10.1016/j.stem.2015.07.005 (2015).
207 Bauer, D. E. *et al.* Cytokine stimulation of aerobic glycolysis in hematopoietic cells exceeds proliferative demand. *FASEB J* **18**, 1303-1305, doi:10.1096/fj.03-1001fje (2004).
208 Utsunomiya-Tate, N., Endou, H. & Kanai, Y. Cloning and functional characterization of a system ASC-like Na+-dependent neutral amino acid transporter. *J Biol Chem* **271**, 14883-14890 (1996).
209 Kammen, H. O. & Hurlbert, R. B. Amination of uridine nucleotides to cytidine nucleotides by soluble mammalian enzymes; role of glutamine and guanosine nucleotides. *Biochim Biophys Acta* **30**, 195-196 (1958).
210 Marsboom, G. *et al.* Glutamine Metabolism Regulates the Pluripotency Transcription Factor OCT4. *Cell Rep* **16**, 323-332, doi:10.1016/j.celrep.2016.05.089 (2016).
211 Alexander, P. B., Wang, J. & McKnight, S. L. Targeted killing of a mammalian cell based upon its specialized metabolic state. *Proc Natl Acad Sci U S A* **108**, 15828-15833, doi:10.1073/pnas.1111312108 (2011).
212 Finley, L. W. S. *et al.* Pluripotency transcription factors and Tet1/2 maintain Brd4-independent stem cell identity. *Nat Cell Biol* **20**, 565-574, doi:10.1038/s41556-018-0086-3 (2018).
213 Shi, Z. D. *et al.* Genome Editing in hPSCs Reveals GATA6 Haploinsufficiency and a Genetic Interaction with GATA4 in Human Pancreatic Development. *Cell Stem Cell* **20**, 675-688 e676, doi:10.1016/j.stem.2017.01.001 (2017).
214 Millard, P., Letisse, F., Sokol, S. & Portais, J. C. IsoCor: correcting MS data in isotope labeling experiments. *Bioinformatics* **28**, 1294-1296, doi:10.1093/bioinformatics/bts127 (2012).

215 Lengner, C. J. *et al.* Oct4 expression is not required for mouse somatic stem cell self-renewal. *Cell Stem Cell* **1**, 403-415, doi:10.1016/j.stem.2007.07.020 (2007).
216 Faubert, B., Solmonson, A. & DeBerardinis, R. J. Metabolic reprogramming and cancer progression. *Science* **368**, doi:10.1126/science.aaw5473 (2020).
217 Wainberg, M. *et al.* A genome-wide almanac of co-essential modules assigns function to uncharacterized genes. *bioRxiv*, 827071, doi:10.1101/827071 (2019).
218 Wang, T. *et al.* Gene Essentiality Profiling Reveals Gene Networks and Synthetic Lethal Interactions with Oncogenic Ras. *Cell* **168**, 890-903 e815, doi:10.1016/j.cell.2017.01.013 (2017).
219 Wainberg, M. *et al.* A genome-wide atlas of co-essential modules assigns function to uncharacterized genes. *Nat Genet* **53**, 638-649, doi:10.1038/s41588-021-00840-z (2021).
220 Bayraktar, E. C. *et al.* Metabolic coessentiality mapping identifies C12orf49 as a regulator of SREBP processing and cholesterol metabolism. *Nat Metab* **2**, 487-498, doi:10.1038/s42255-020-0206-9 (2020).
221 Tsherniak, A. *et al.* Defining a Cancer Dependency Map. *Cell* **170**, 564-576 e516, doi:10.1016/j.cell.2017.06.010 (2017).
222 Chen, P. H. *et al.* Metabolic Diversity in Human Non-Small Cell Lung Cancer Cells. *Mol Cell* **76**, 838-851 e835, doi:10.1016/j.molcel.2019.08.028 (2019).
223 Alves, T. C. *et al.* Integrated, Step-Wise, Mass-Isotopomeric Flux Analysis of the TCA Cycle. *Cell Metab* **22**, 936-947, doi:10.1016/j.cmet.2015.08.021 (2015).
224 Sullivan, L. B. *et al.* Aspartate is an endogenous metabolic limitation for tumour growth. *Nat Cell Biol* **20**, 782-788, doi:10.1038/s41556-018-0125-0 (2018).
225 Lewis, C. A. *et al.* Tracing compartmentalized NADPH metabolism in the cytosol and mitochondria of mammalian cells. *Mol Cell* **55**, 253-263, doi:10.1016/j.molcel.2014.05.008 (2014).
226 Williamson, D. H., Lund, P. & Krebs, H. A. The redox state of free nicotinamide-adenine dinucleotide in the cytoplasm and mitochondria of rat liver. *Biochem J* **103**, 514-527, doi:10.1042/bj1030514 (1967).
227 Shintaku, J. *et al.* MyoD Regulates Skeletal Muscle Oxidative Metabolism Cooperatively with Alternative NF-kappaB. *Cell Rep* **17**, 514-526, doi:10.1016/j.celrep.2016.09.010 (2016).
228 Stacpoole, P. W. The pharmacology of dichloroacetate. *Metabolism* **38**, 1124-1144, doi:10.1016/0026-0495(89)90051-6 (1989).
229 Kalkan, T. *et al.* Tracking the embryonic stem cell transition from ground state pluripotency. *Development* **144**, 1221-1234, doi:10.1242/dev.142711 (2017).
230 Vardhana, S. A. *et al.* Glutamine independence is a selectable feature of pluripotent stem cells. *Nat Metab* **1**, 676-687, doi:10.1038/s42255-019-0082-3 (2019).
231 Wray, J. *et al.* Inhibition of glycogen synthase kinase-3 alleviates Tcf3 repression of the pluripotency network and increases embryonic stem cell resistance to differentiation. *Nat Cell Biol* **13**, 838-845, doi:10.1038/ncb2267 (2011).
232 Borst, P. The malate-aspartate shuttle (Borst cycle): How it started and developed into a major metabolic pathway. *IUBMB Life* **72**, 2241-2259, doi:10.1002/iub.2367 (2020).

233 Assmann, N. *et al.* Srebp-controlled glucose metabolism is essential for NK cell functional responses. *Nat Immunol* **18**, 1197-1206, doi:10.1038/ni.3838 (2017).
234 Luengo, A. *et al.* Increased demand for NAD(+) relative to ATP drives aerobic glycolysis. *Mol Cell*, doi:10.1016/j.molcel.2020.12.012 (2020).
235 Zhu, X. G. *et al.* Functional Genomics In Vivo Reveal Metabolic Dependencies of Pancreatic Cancer Cells. *Cell Metab* **33**, 211-221 e216, doi:10.1016/j.cmet.2020.10.017 (2021).
236 Dempster, J. M. Extracting Biological Insights from the Project Achilles Genome-Scale CRISPR Screens in Cancer Cell Lines. (2019).
237 Meyers, R. M. *et al.* Computational correction of copy number effect improves specificity of CRISPR-Cas9 essentiality screens in cancer cells. *Nat Genet* **49**, 1779-1784, doi:10.1038/ng.3984 (2017).
238 Ashburner, M. *et al.* Gene ontology: tool for the unification of biology. The Gene Ontology Consortium. *Nat Genet* **25**, 25-29, doi:10.1038/75556 (2000).
239 The Gene Ontology, C. The Gene Ontology Resource: 20 years and still GOing strong. *Nucleic Acids Res* **47**, D330-D338, doi:10.1093/nar/gky1055 (2019).
240 Virtanen, P. *et al.* SciPy 1.0: fundamental algorithms for scientific computing in Python. *Nat Methods* **17**, 261-272, doi:10.1038/s41592-019-0686-2 (2020).
241 Ghandi, M. *et al.* Next-generation characterization of the Cancer Cell Line Encyclopedia. *Nature* **569**, 503-508, doi:10.1038/s41586-019-1186-3 (2019).
242 Subramanian, A. *et al.* Gene set enrichment analysis: a knowledge-based approach for interpreting genome-wide expression profiles. *Proc Natl Acad Sci U S A* **102**, 15545-15550, doi:10.1073/pnas.0506580102 (2005).
243 Dow, L. E. *et al.* Inducible in vivo genome editing with CRISPR-Cas9. *Nat Biotechnol* **33**, 390-394, doi:10.1038/nbt.3155 (2015).
244 Ran, F. A. *et al.* Genome engineering using the CRISPR-Cas9 system. *Nat Protoc* **8**, 2281-2308, doi:10.1038/nprot.2013.143 (2013).
245 Fellmann, C. *et al.* An optimized microRNA backbone for effective single-copy RNAi. *Cell Rep* **5**, 1704-1713, doi:10.1016/j.celrep.2013.11.020 (2013).
246 Millard, P. *et al.* IsoCor: isotope correction for high-resolution MS labeling experiments. *Bioinformatics* **35**, 4484-4487, doi:10.1093/bioinformatics/btz209 (2019).
247 Chen, S., Zhou, Y., Chen, Y. & Gu, J. fastp: an ultra-fast all-in-one FASTQ preprocessor. *Bioinformatics* **34**, i884-i890, doi:10.1093/bioinformatics/bty560 (2018).
248 Dobin, A. *et al.* STAR: ultrafast universal RNA-seq aligner. *Bioinformatics* **29**, 15-21, doi:10.1093/bioinformatics/bts635 (2013).
249 Liao, Y., Smyth, G. K. & Shi, W. featureCounts: an efficient general purpose program for assigning sequence reads to genomic features. *Bioinformatics* **30**, 923-930, doi:10.1093/bioinformatics/btt656 (2014).
250 Love, M. I., Huber, W. & Anders, S. Moderated estimation of fold change and dispersion for RNA-seq data with DESeq2. *Genome Biol* **15**, 550, doi:10.1186/s13059-014-0550-8 (2014).
251 Villafranca, J. J. & Mildvan, A. S. The mechanism of aconitase action. II. Magnetic resonance studies of the complexes of enzyme, manganese(II), iron(II), and substrates. *J Biol Chem* **246**, 5791-5798 (1971).

252 Kaplan, R. S., Morris, H. P. & Coleman, P. S. Kinetic characteristics of citrate influx and efflux with mitochondria from Morris hepatomas 3924A and 16. *Cancer Res* **42**, 4399-4407 (1982).
253 Majd, H., King, M. S., Smith, A. C. & Kunji, E. R. S. Pathogenic mutations of the human mitochondrial citrate carrier SLC25A1 lead to impaired citrate export required for lipid, dolichol, ubiquinone and sterol synthesis. *Biochim Biophys Acta Bioenerg* **1859**, 1-7, doi:10.1016/j.bbabio.2017.10.002 (2018).
254 Deja, S., Crawford, P. A. & Burgess, S. C. Krebs takes a turn at cell differentiation. *Cell Metab* **34**, 658-660, doi:10.1016/j.cmet.2022.04.005 (2022).
255 Beigneux, A. P. *et al.* ATP-citrate lyase deficiency in the mouse. *J Biol Chem* **279**, 9557-9564, doi:10.1074/jbc.M310512200 (2004).
256 Prasun, P. *et al.* Expanding the Clinical Spectrum of Mitochondrial Citrate Carrier (SLC25A1) Deficiency: Facial Dysmorphism in Siblings with Epileptic Encephalopathy and Combined D,L-2-Hydroxyglutaric Aciduria. *JIMD Rep* **19**, 111-115, doi:10.1007/8904_2014_378 (2015).
257 Sharpley, M. S., Chi, F., Hoeve, J. T. & Banerjee, U. Metabolic plasticity drives development during mammalian embryogenesis. *Dev Cell* **56**, 2329-2347 e2326, doi:10.1016/j.devcel.2021.07.020 (2021).
258 Solmonson, A. *et al.* Compartmentalized metabolism supports midgestation mammalian development. *Nature* **604**, 349-353, doi:10.1038/s41586-022-04557-9 (2022).
259 Johnston, K. *et al.* Isotope tracing reveals glycolysis and oxidative metabolism in childhood tumors of multiple histologies. *Med (N Y)* **2**, 395-410, doi:10.1016/j.medj.2021.01.002 (2021).